

# FINAL REPORT

## Non-traditional Physics-based Inverse Approaches for Determining a Buried Object's Location

SERDP Project MM-1592

SEPTEMBER 2008

Dr. Fridon Shubitidze  
Thayer School of Engineering, Dartmouth College



Strategic Environmental Research and  
Development Program

Report Documentation Page				Form Approved OMB No. 0704-0188	
Public reporting burden for the collection of information is estimated to average 1 hour per response, including the time for reviewing instructions, searching existing data sources, gathering and maintaining the data needed, and completing and reviewing the collection of information. Send comments regarding this burden estimate or any other aspect of this collection of information, including suggestions for reducing this burden, to Washington Headquarters Services, Directorate for Information Operations and Reports, 1215 Jefferson Davis Highway, Suite 1204, Arlington VA 22202-4302. Respondents should be aware that notwithstanding any other provision of law, no person shall be subject to a penalty for failing to comply with a collection of information if it does not display a currently valid OMB control number.					
1. REPORT DATE <b>01 SEP 2008</b>		2. REPORT TYPE <b>N/A</b>		3. DATES COVERED <b>-</b>	
4. TITLE AND SUBTITLE <b>Non-traditional Physics-based Inverse Approaches for Determining a Buried Objects Location</b>				5a. CONTRACT NUMBER	
				5b. GRANT NUMBER	
				5c. PROGRAM ELEMENT NUMBER	
6. AUTHOR(S)				5d. PROJECT NUMBER	
				5e. TASK NUMBER	
				5f. WORK UNIT NUMBER	
7. PERFORMING ORGANIZATION NAME(S) AND ADDRESS(ES) <b>Thayer School of Engineering, Dartmouth College</b>				8. PERFORMING ORGANIZATION REPORT NUMBER	
9. SPONSORING/MONITORING AGENCY NAME(S) AND ADDRESS(ES)				10. SPONSOR/MONITOR'S ACRONYM(S)	
				11. SPONSOR/MONITOR'S REPORT NUMBER(S)	
12. DISTRIBUTION/AVAILABILITY STATEMENT <b>Approved for public release, distribution unlimited</b>					
13. SUPPLEMENTARY NOTES <b>The original document contains color images.</b>					
14. ABSTRACT					
15. SUBJECT TERMS					
16. SECURITY CLASSIFICATION OF:			17. LIMITATION OF ABSTRACT <b>UU</b>	18. NUMBER OF PAGES <b>98</b>	19a. NAME OF RESPONSIBLE PERSON
a. REPORT <b>unclassified</b>	b. ABSTRACT <b>unclassified</b>	c. THIS PAGE <b>unclassified</b>			

This report was prepared under contract to the Department of Defense Strategic Environmental Research and Development Program (SERDP). The publication of this report does not indicate endorsement by the Department of Defense, nor should the contents be construed as reflecting the official policy or position of the Department of Defense. Reference herein to any specific commercial product, process, or service by trade name, trademark, manufacturer, or otherwise, does not necessarily constitute or imply its endorsement, recommendation, or favoring by the Department of Defense.

# Executive Summary

The research described in this report was conducted in fulfillment of Project MM-1592, “Non-traditional physics-based inverse approaches for determining a buried object’s location,” submitted to the Strategic Environmental Research and Development Program’s (SERDP) Exploratory Development Program (SEED) in response to Statement of Need MMSEED-07-02, “Advanced Technologies for Detection, Discrimination, and Remediation of Munitions and Explosives of Concern (MEC): UXO Technology.”

The main focus of this research was to explore and develop new electromagnetic inverse-scattering approaches for estimating the locations and orientations of buried objects that would not involve the solution of an ill-posed nonlinear minimization problem and that would be sufficiently robust and efficient to be used in real field UXO discrimination. We concentrated on the fundamental aspects and potential practical applicability to the UXO problem of three novel physics-based approaches: (1) pole-series expansions, (2) energy gradients, and (3) use of the physical properties of left-handed media (LHM). All three methods assume that targets’ responses can be approximately reproduced by means of a set of magnetic dipoles—the scattered field singularities—distributed in particular points inside the objects. The algorithms are implemented using a numerical technique called the Normalized Surface Magnetic Source (NSMS) model. We studied the accuracy with which the methods can estimate an object’s location, orientation, and equivalent magnetic polarizability, their robustness with respect to noise, their computational speed, and their requirements with regard to data quality and quantity. We ultimately wanted to determine which of these three techniques would be practical and reliable for use in real UXO production runs.

As part of this investigation we studied several existing data sets collected by established instruments such as the Geophex GEM-3 and the Geonics EM-63 and by next-generation sensors like the NRL discrimination array, the MPV-TD and the GEM-3D+. The GEM-3, GEM-3D+, and TD MPV data were collected at the ERDC-CRREL test site in Hanover, NH, by CRREL personnel; the EM-63 data were collected at the ERDC test stand in Vicksburg, MS, by operators from Sky Research and the University of British Columbia; and the NRL discrimination array data were collected by NRL researchers. The new proposed algorithms were applied to these data sets in order to estimate locations, orientations, and equivalent magnetic polarizability tensors of buried objects; in addition we conducted discrimination studies using the NSMS model so as to demonstrate the applicability of these techniques.

# Acknowledgments

The Principal Investigator, Prof. Fridon Shubitidze of the Thayer School of Engineering at Dartmouth College, conceived, implemented, and tested most of the approaches presented in this report. He developed the NSMS model and the HAP method and integrated them into a location/discrimination algorithm that can be adapted to any sensor and UXO collection.

Prof. David Karkashadze of Tbilisi State University in Tbilisi, Georgia, was Visiting Professor at the Thayer School in the summer of 2007. In that capacity, and as an expert in the MAS, he obtained most of the LHM results of Chapter 4.

Dr. Juan Pablo Fernández joined the project as a student at the Thayer School and, upon graduating, continued there as a postdoctoral researcher. He prepared the MPV-TD data of Chapter 2 for use by the HAP method and verified those results using other techniques. He edited many successive drafts of this report and of the papers on which it is based.

Dr-s. Benjamin Barrowes and Kevin O'Neill of CRREL took the MPV-TD data analyzed in Chapter 2. They shared their expertise in electromagnetism during group meetings.

The rest of the data from Chapter 2 were taken CRREL (GEM-3 and GEM-3D+), Sky Research (EM-63), and NRL (EMI TD) personnel.

# Table of Contents

	Page
List of figures .....	v
List of tables .....	viii
 <b>Chapter</b>	
1 Introduction .....	1
2 The HAP approach for estimating the location, orientation, and magnetic polarizability of a buried object.....	4
2.1 Introduction .....	4
2.2 Estimating a buried object's location, orientation and magnetic polarization from EMI data .....	4
2.3 A reduced HAP formulation for estimating a buried object's location and orientation.....	6
2.4 Predicting the vector and scalar potentials from EMI data .....	7
2.4.1 Determining vector and scalar potentials from multistatic data.....	9
2.4.2 Determining $\tilde{\mathbf{A}}_1^{\text{sc}}$ and $\tilde{\psi}_1^{\text{sc}}$ from monostatic data using NSMS .....	11
2.5 The Normalized Surface Magnetic Source model.....	13
2.6 A numerical procedure for estimating orientation.....	15
2.7 Matrix diagonalization .....	16
2.8 Results .....	17
2.8.1 Estimating the location of a buried object using synthetic EMI data .....	17
2.8.2 Predicting a dipole's orientation from monostatic synthetic data .....	18
2.8.3 Noise effect: predicting a dipole's orientation from monostatic noisy synthetic data .....	19
2.8.4 Studies for a highly conducting and permeable sphere .....	23
2.8.5 Studies for non-spherical and heterogeneous objects.....	23
2.8.6 Noise-effect analysis for heterogeneous objects .....	26
2.8.7 Estimating object location using measured monostatic and multistatic EMI data .....	26
2.8.7.a Frequency-domain EMI data.....	26
2.8.7.b Time-domain EMI-63 data.....	31
2.8.7.c MPV-TD data blind-test analysis.....	32
2.8.7.d EMI Array .....	37
2.9 Conclusion.....	42
3 Pole-series and pseudospectral approaches for estimating a buried object's depth .....	43
3.1 Introduction .....	43
3.2 The pole-series-expansion approach in EMI.....	43
3.3 Pseudospectral FD scheme in EMI .....	46
3.4 Noise analysis in the PSE and PSFD approaches.....	48
3.5 Results .....	48
3.5.1 PSE applied to a dipole .....	48

3.5.2	Extending the EMI field upwards .....	51
3.5.3	Combining NSMS and PSE .....	51
3.5.4	PSE-NSMS applied to measured EM-63 data.....	53
3.5.5	PSFD for refocusing the scattered magnetic field.....	62
3.6	Conclusion.....	63
4	Scatterer localization using a left-handed-medium slab.....	64
4.1	Introduction .....	64
4.2	Governing equations in the EM wave regime .....	64
4.3	Boundary conditions at a free-space/LHM interface.....	67
4.4	Refocusing of the scattered EM field using LHM.....	68
4.5	The method of auxiliary sources for LHM in the EM-wave regime .....	68
4.6	Numerical results.....	72
4.6.1	Point-source and Gaussian-beam illumination results .....	72
4.6.2	LHM applied to multiple sources and objects.....	74
4.6.3	An attempt to extend the LHM approach to the EMI regime.....	79
4.7	Conclusion.....	81
5	Discussion and conclusions.....	82
5.1	Objectives.....	82
5.2	HAP method.....	83
5.3	Outlook.....	83
	References .....	85

# List of Figures

Figure		Page
2.1	Geometry of the problem. The target is assumed to be a magnetic dipole located at $\mathbf{r}_d$ .....	5
2.2	Multistatic EMI data survey scenario showing the intermediate NSMS surface. The potentials $\mathbf{A}$ and $\psi$ are obtained from sources on this surface which reproduce the dipolar target.....	8
2.3	Geometry of the NSMS model.....	12
2.4	Inverted coordinates (a) $x_o$ , (b) $y_o$ and (c) $z_o$ for a dipole. Inverted locations for these synthetic tests are essentially exact and demonstrate the viability of this method.....	17
2.5	Three source dipoles at different depths: (a) Problem geometry. Inverted coordinates of inverted aggregate dipole (b) $x_o$ , and (c) $z_o$ .....	18
2.6	Scattered magnetic field and scalar magnetic potential for a dipole source. Left: no noise added; right: noise added .....	20
2.7	Problem geometry for a sphere under the measurement plane.....	21
2.8	Estimated $z_c$ for the sphere in Figure 2.7 .....	21
2.9	Estimated $\sqrt{x_c^2 + y_c^2}$ for the sphere in Figure 2.7 .....	21
2.10	Estimated $z_c$ for the sphere in Figure 2.7 vs. observation point.....	21
2.11	Geometry of the problem for a homogeneous object .....	22
2.12	Estimated $z_c$ for the bullet of Figure 2.11 .....	22
2.13	Estimated $\sqrt{x_c^2 + y_c^2}$ for the bullet of Figure 2.11 .....	22
2.14	Estimated $z_c$ for the bullet in Figure 2.11 vs. observation point.....	22
2.15	Problem geometry for a heterogeneous object .....	24
2.16	Estimated $z_c$ for the heterogeneous object of Figure 2.15.....	24
2.17	Estimated $\sqrt{x_c^2 + y_c^2}$ for the heterogeneous object of Figure 2.15.....	24
2.18	Estimated $z_c$ for the bullet of Figure 2.15 vs. observation point.....	24
2.19	Scattered magnetic field from a 90-mm UXO modeled via the SEA using synthetic data (a) without and (b) with noise. (c) Inverted location from noise-free and noisy data.....	25
2.20	The GEM-3D+ sensor head showing the transverse receiver coils.....	27
2.21	Comparisons between actual and modeled data.....	27
2.22	Comparisons between actual and predicted data for a sphere subject to GEM-3D+ excitation: (a) $x$ -component, (b) $y$ -component .....	28
2.23	Estimated $\sqrt{x_c^2 + y_c^2}$ (left) and $z_c$ (right) for the steel sphere. The true $z_c = 26$ cm .....	29
2.24.	Comparison between GEM-3D+ blind tests inversions and library NSMS .....	30–31
2.25	Estimated $z_c$ for the 81-mm UXO. The true $z_c = 60$ cm.....	31
2.26	Actual and schematic diagram of the MPV-TD sensor.....	32
2.27	Predicted and actual TD MPV data for a 60-mm UXO .....	33
2.28	NSMS model comparison to library for Target #1.....	34
2.29	NSMS model comparison to library for Target #4 (left) and Target #5 (right) .....	35
2.30	NSMS model comparison to library for Target #2 (left) and Target #3 (right) .....	36
2.31	EMI TD array sensor in operation.....	37
2.32	Schematic diagram of the EMI TD array sensor .....	38



2.33	Measured EM field distribution on $5 \times 5$ array receivers for time channel #1 for different (from 1 to 25) transmission; each subplot corresponds to a fixed transmitter.....	39
2.34	Measured EM field distribution on $5 \times 5$ array receivers for time channel #40 for different (from 1 to 25) transmission; each subplot corresponds to a fixed transmitter.....	40
2.35	Inverted position for Camp Sibert 4.2-inch UXO vs. transmission number at different time channels .....	41
3.1	Schematic diagram of the PSE algorithm.....	45
3.2	Yee FD scheme for the PSFD approach.....	46
3.3	Comparison between predicted and actual fields for a magnetic dipole .....	49
3.4	(a) Experimental setup for $H_z$ field upper continuation and (b) clutter items used in the experiment. Plots: Inphase (top) and quadrature (bottom) $H_z$ field distribution on the measurement plane as predicted by NSMS (left) and measured by the GEM-3 (right).....	50
3.5	$H_z$ bistatic magnetic field on a grid .....	52
3.6	Distribution of predicted $H_z$ magnetic field intensity over the $x$ - $z$ plane for a 2.75-inch rocket oriented horizontally and interrogated by the GEM-3 sensor. The different panels correspond to increasing noise levels: (a) 0, (b) 0.5%, (c) 1%, (d) 2%, (e) 3%, (f) 5%, (g) 10%, (h) 15% .....	54–57
3.7	Distribution of predicted $H_z$ magnetic field intensity over the $x$ - $z$ plane for a 2.75-inch rocket at $45^\circ$ inclination and interrogated by the GEM-3 sensor. The different panels correspond to increasing noise levels: (a) 0, (b) 0.5%, (c) 1%, (d) 2%, (e) 3%, (f) 5%, (g) 10%, (h) 15% .....	58–61
3.8	Predicted and actual scattered magnetic field of a sphere at different heights above the sphere center. The y-scale is logarithmic .....	62
4.1	Configuration of Poynting vectors ( $\mathbf{S}$ ) and wave vectors ( $\mathbf{k}$ ) in a LHM half-space.....	65
4.2	Interface between free space and a LHM showing a negative angle of refraction.....	66
4.3	Schematic diagram of a 2D EM problem .....	67
4.4	MAS geometry for a uniform half-space model.....	69
4.5	Electric field distribution around a point source (left) and MAS-predicted electric field distribution in a virtual LHM half-space with $n = -1$ (right) .....	72
4.6	Electric field distribution from a Gaussian beam (left) and MAS-predicted electric field distribution in a virtual LHM half-space with $n = -1$ (right).....	73
4.7	Four Gaussian beam sources placed in a virtual LHM space with $n = -1$ . Left: electric field-intensity distribution. Right: phase distribution .....	74
4.8	Actual (in free space, at left) and reconstructed (in a LHM with $n = -1$ , at right) electric field-intensity (top row) and phase (bottom row) distributions for three point sources.....	75
4.9	Actual (in free space, at left) and reconstructed (in a LHM with $n = -1$ , at right) electric field intensity (top row) and phase (bottom row) distributions for a cylindrical scatterer .....	76
4.10	Electric field intensity distribution for three objects: actual (in free space, at left) and reconstructed (in a LHM with $n = -1$ , at right).....	77
4.11	Magnetic field intensity ( $H_x$ ) distribution for two objects: actual (in free space, at left) and reconstructed (in a LHM with $n = -1$ , at right).....	77
4.12	Magnetic field ( $H_y$ ) intensity distribution for two objects: actual (in free space, at left) and reconstructed (in a LHM with $n = -1$ , at right) .....	78

4.13	Reconstructed electric field-intensity (left) and phase (right) distributions for three point sources in a LHM with $n = -1$ when the wavelength is 1000 times greater than the distances between the objects .....	79
4.14	Problem geometry (left) and reconstructed magnetic-field intensity distribution (right) for a dipole .....	80

# List of Tables

Table		Page
2.1	Estimated and actual orientation of a dipole using a synthetic data set.....	19
2.2	Estimated and actual orientation for the dipole using noisy data.....	19
2.3	Estimated and actual positions and orientations for the GEM-3D+ blind-test data runs .....	29
2.4	Ground truth for the MPV-TD blind-test data runs .....	34
2.5	Inverted results for position and orientation for MPV-TD blind-test data. Numbers with an asterisk are arbitrary due to BOR considerations.....	34

## List of acronyms

2D	Two-Dimensional
3D	Three-Dimensional
BOR	Body of Revolution
BUD	Berkeley UXO Discriminator
CRREL	Cold Regions Research and Engineering Laboratory
EM	Electromagnetic
EM-63	An EMI sensor developed by Geonics, Inc.
EMI	Electromagnetic Induction Regime
EMI-BOR	An MAS-based computer program developed at Dartmouth College that solves electromagnetic scattering problems in the EMI regime
ERDC	Engineer Research and Development Center
FD	Frequency Domain; Finite Differences
FFT	Fast Fourier Transform
GEM-3	An EMI sensor developed by Geophex, Inc.
GEM-3D+	A vector version of the GEM-3
GSEA	Generalized Standardized Excitation Approach
HAP	A method to estimate the location and orientation of a target employing the magnetic field $\mathbf{H}$ , the vector potential $\mathbf{A}$ , and the magnetic scalar potential $\psi$ (Psi)
LH	Left-Handed
LHM	Left-Handed Medium; Left-Handed Material
LS	Least-Squares Method
MAS	Method of Auxiliary Sources
MAS-TSA	Method of Auxiliary Sources, complemented with the Thin Skin Approximation for high frequencies
MEC	Munitions and Explosives of Concern
MPV-TD	The Man-Portable Vector Time-Domain Sensor, developed by CRREL and G&G Sciences, Inc.
MQS	Magnetoquasistatic Approximation
NRL	Naval Research Laboratory
NRL EMI	An EMI array-type sensor developed by NRL
NSMC	Normalized Surface Magnetic Charge Model
NSMS	Normalized Surface Magnetic Source Model
PSE	Pole-Series Expansion Method
PSFD	Pseudospectral Finite-Difference Method
PSTD	Pseudospectral Time-Domain Method (same as PSFD)
RH	Right-Handed
SEA	Standardized Excitation Approach
SEED	SERDP Exploratory Development Program
SERDP	Strategic Environmental Research and Development Program
SFS	Scattered Field Singularity
TD	Time Domain
TD EMI	Another name for the NRL EMI array sensor
USACE	U.S. Army Corps of Engineers
UXO	Unexploded Ordnance

# Chapter 1

## Introduction

The research described in this report was conducted in fulfillment of Project MM-1592, “Non-traditional physics-based inverse approaches for determining buried objects’ location,” submitted to the Strategic Environmental Research and Development Program’s (SERDP) Exploratory Development Program (SEED) in response to Statement of Need MMSEED-07-02, “Advanced Technologies for Detection, Discrimination, and Remediation of Munitions and Explosives of Concern (MEC): UXO Technology.”

Several data-processing techniques for geophysical survey data have been developed for discriminating between unexploded ordnance (UXO) and non-UXO items. Typically the first step of these methods is the recovery of a set of parameters that specify a physics-based model representing the object under interrogation. For example, in electromagnetic induction (EMI) sensing, the recovered parameters consist of the object’s location and spatial orientation in addition to “intrinsic” parameters such as the polarizability tensor (along with some parameterization of its time-decay curve) in dipole models (Pasion and Oldenburg, 2001) or the amplitudes of responding magnetic sources in the NSMS and SEA models (Shubitidze *et al.*, 2005; Sun *et al.*, 2005; Shubitidze *et al.*, 2007). EMI responses depend nonlinearly on the subsurface object’s location and orientation, and inverting for these parameters quickly and accurately is a crucial part of all the inversion techniques currently in use by the UXO community.

Most EMI sensors are composed of separate transmitting and receiving coils. When the operator activates the sensor, a current runs through the transmitter coils, which results in the establishment of a (“primary” or “principal”) magnetic field in the surrounding space. By Faraday’s law, this time-varying magnetic field induces eddy currents in highly conducting bodies; ferromagnetic bodies also have their magnetization affected by the impinging field. These currents and magnetization in turn generate a (“secondary” or “scattered”) magnetic field that also varies with time and induces measurable currents in the receiving coils. At the end, the electromagnetic data are inverted using different forward models. The procedure for estimating the location, orientation, and electromagnetic parameters of a buried object (strung together in a “model vector”  $\mathbf{v}$ ) is carried out by defining an objective function that quantifies the goodness-of-fit between the measured data and the predictions of the forward model. Routinely, a least-squares (LS) approach is taken to recover  $\mathbf{v}$ : formally, if  $\mathbf{d}^{\text{obs}}$  is the vector of the measured scattered field and  $\mathbf{F}(\mathbf{v})$  is the solution to the forward problem, the least-squares criterion assumes the form

$$\text{minimize } \phi(\mathbf{v}) = \left\| \mathbf{d}^{\text{obs}} - \mathbf{F}(\mathbf{v}) \right\|^2. \quad (1)$$

A simple way to determine the model vector  $\mathbf{v}$  is to use the Gauss-Newton method, which starts with an initial guess  $\mathbf{v}_0$  and updates it iteratively through

$$\mathbf{v}_{k+1} = \mathbf{v}_k + \mathbf{J}(\mathbf{v}_k)^{-1} (\mathbf{d}^{\text{obs}} - \mathbf{F}(\mathbf{v}_k)), \quad (2)$$

where  $k$  denotes the iteration number and  $\mathbf{s}_k$  is a perturbation direction; we solve for the  $\mathbf{s}_k$  that minimizes  $\phi$ . This approach is computationally intensive because it requires massive repetition of the forward-problem solution. In particular, the determination of the nonlinear elements of  $\mathbf{v}$ —the location and orientation of the object—is nontrivial and time-consuming.

The main motivation of this project was to develop new non-traditional physics-based inverse scattering approaches that would enable us to infer the location of a buried object from measured data without having to solve a nonlinear ill-posed EMI inverse problem. Specifically, we proposed to investigate three physics-based methods involving (1) energy gradients, (2) pole-series expansions, and (3) the physical properties of left-handed media (LHM). All three approaches assume that targets exhibit a dipolar response. Secondary magnetic fields in the EMI regime are due to eddy currents or magnetic dipoles distributed nonuniformly inside the scatterers. There are some particular points, the “scattered field singularities” (SFS), where most of these sources are concentrated. Recent studies show that under certain conditions the entire scatterer can be replaced with several responding elementary sources placed at the SFS (Kyurhkan *et al.*, 1996; Zaridze *et al.*, 2002; Bliznyuk *et al.*, 2005). The mathematical and physical properties of SFS and their application to electromagnetic scattering problems are very well documented and studied, and constitute the discipline known in the literature as “Catastrophe Theory” (Arnold, 1986). Our objective in this project was to utilize the three approaches mentioned above to find fast and effective ways to determine the locations of these singularities.

In the energy-gradient approach we found that it is possible to determine the location and orientation of a buried object if we have access to (1) the magnetic field vector  $\mathbf{H}$ , (2) the vector potential  $\mathbf{A}$ , and (3) the scalar magnetic potential  $\psi$  at a single point in space. Since of these quantities only  $\mathbf{H}$ , or one of its components, is available, as part of this project we developed a numerical procedure based on the 2D normalized surface magnetic source (NSMS) model that reconstructs  $\mathbf{A}$  and  $\psi$  from  $\mathbf{H}$ .

The NSMS model can be considered as a generalized surface dipole model and indeed reduces to the usual dipole model in a special limiting case. The full 3D NSMS approach models an object’s response to a primary field by distributing a set of equivalent elementary magnetic sources over an auxiliary surface surrounding the target (Shubitidze *et al.*, 2007); the field radiated by these elementary sources satisfies analytically the governing EMI equations outside the scatterer. The surface integral of the source amplitudes can be used as a discriminator; moreover, the method can be used to generate a synthetic scattered magnetic field  $\mathbf{H}$  and its corresponding potentials  $\mathbf{A}$  and  $\psi$ . The NSMS has proved to be successful in single- and multiple-target discrimination studies, but, lacking a method to rapidly and independently determine the location and orientation of the target (and hence of the surrounding surface), it has to be used within a time-consuming and computationally expensive optimization procedure. The 2D NSMS method, on the other hand, replaces the surface around the scatterer with a flat plane of dipoles at a (known) location intermediate between the instrument and the target. Given high-spatial-coverage geophysical data taken over a buried object it is possible to calculate the amplitudes of the responding magnetic sources on the intermediate plane by solving a linear system of equations. The amplitudes can then be used to estimate  $\mathbf{H}$ ,  $\mathbf{A}$ , and  $\psi$  at any point on or above the measurement surface, and these in turn can be combined analytically to solve for the relative location  $\mathbf{R}$  and the polarizability  $\overline{\mathbf{M}}$  of the hypothetical dipole.

Chapter 2 outlines our research into this method, to which we will refer from now on as the HAP approach. As we shall see, the HAP method provides fast and accurate estimates of the

location, orientation, and induced magnetic polarizability of a visually obscured object. We tested the procedure using both synthetic and measured data, both in the time domain (with the EM-63, MPV-TD, and NRL array sensors) and in the frequency domain (using the GEM-3D+), and successfully combined it with the 3D NSMS method in MPV-TD and GEM-3D+ blind tests. Its performance and its tolerance to noise make this approach our definitive candidate for real-field applications. We also introduce an equivalent but reduced version of the HAP that employs only  $\mathbf{H}$  and  $\psi$ .

The pole-series-expansion approach involves determining a spatial distribution of scattered field singularities which can be related to a target's properties (*i.e.*, its shape and size). It uses scattered-field information at a given set of points, again estimated via a 2D NSMS approximation, to quickly locate the origin of this scattered field at any spatial resolution. A similar technique developed for this project is the pseudospectral finite-difference (PSFD) method, which is based on spatial finite-difference approximations. Chapter 3 outlines our research into these modeling techniques. We find that the methods are fast but very sensitive to noise, which detracts from their potential usefulness in the field.

The last approach we developed uses left-handed media (LHM), and in particular their EM field-refocusing property, as a tool for estimating the location of a buried object. In the low-frequency EMI regime one first reconstructs a Gaussian beam by combining a monostatic EMI spatial distribution with an empirically assigned wave-phase part; after that one solves a full EM scattering problem in order to map the field distribution back to its origin. Chapter 4 outlines our research into LHM in order to assess their potential usefulness in the context of the UXO problem. Our studies show that in the low-frequency regime the LHM refocusing approach is impractical because the necessary wavelengths are much larger than the size and depth of any potentially interesting target; however, the research reported here could be useful for the EM-wave community.

Finally, Chapter 5 summarizes this report and suggests future research directions.

## Chapter 2

# The HAP approach for estimating the location, orientation, and magnetic polarizability of a buried object

### 2.1. Introduction

In this chapter we present a new, physics-based expression for determining the location, orientation, and magnetic polarizability of a buried object. The approach assumes that the target exhibits a dipolar response; it requires three global values—the magnetic field vector  $\mathbf{H}$ , the vector potential  $\mathbf{A}$ , and the scalar magnetic potential  $\psi$ —to be evaluated at a single location in space. Of these values only the scattered magnetic field  $\mathbf{H}$  is measurable. Therefore, in order to estimate the scattered magnetic scalar and vector potentials from data, we employ a numerical technique called the normalized surface magnetic source (NSMS) method. In the original NSMS model, the scattered magnetic field outside an object is reproduced mathematically by equivalent magnetic charges distributed on a 3D closed surface. Here we use a 2D implementation of the NSMS that uses elementary magnetic dipoles (instead of magnetic charges) distributed on a planar surface placed under the measurement grid. These sources are used to estimate the scattered magnetic field's vector potential  $\mathbf{A}$  and scalar magnetic potential  $\psi$  without *a priori* knowledge of the object's location and orientation. The amplitudes of the NSMS are determined by matching the measured magnetic field with the NSMS modeled field. Once the NSMS amplitudes are determined,  $\mathbf{H}$ ,  $\mathbf{A}$ , and  $\psi$  are simulated on or above the measurement grid. After reviewing the theoretical basis and the practical implementation of the new technique, we demonstrate its applicability to UXO discrimination by using synthetic and measured data. We then present several numerical and experimental tests with actual UXO interrogated by the EM-63, MPV-TD, NRL EMI array and GEM-3D+ sensors.

### 2.2. Estimating a buried object's location, orientation and magnetic polarization from EMI data

In the low-frequency EMI regime considered here, the primary magnetic field penetrates a metallic object to some (frequency-dependent) degree and induces eddy currents/magnetic dipoles within it. These induced currents and dipoles then produce a secondary or scattered field outside the object that is measured by a receiver. Using the magnetic dipole approximation we can write the magnetic field  $\mathbf{H}$  and the scalar and vector potentials  $\psi$  and  $\mathbf{A}$  as

$$\mathbf{H} = \frac{e^{jkR}}{4\pi R^3} \left[ \left( \frac{3\mathbf{R}(\mathbf{R} \cdot \mathbf{m})}{R^2} - \mathbf{m} \right) (1 - jkR) - k^2 (\mathbf{R} \times (\mathbf{R} \times \mathbf{m})) \right], \quad (2.1)$$



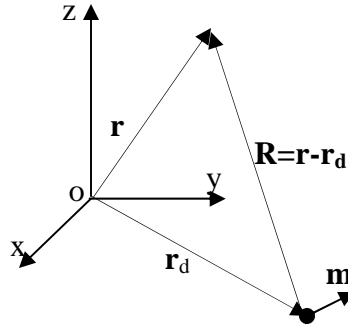


**Figure 2.1.** Geometry of the problem. The target is assumed to be a magnetic dipole located at  $\mathbf{r}_d$ .

$$\psi = \frac{(\mathbf{R} \cdot \mathbf{m})}{4\pi R^3} (1 - jkR) e^{jkR}, \quad (2.2)$$

$$\mathbf{A} = \mu_o \frac{(\mathbf{m} \times \mathbf{R})}{4\pi R^3} (1 - jkR) e^{jkR}, \quad (2.3)$$

where  $k$  is the wave number in the surrounding medium,  $\mathbf{R} = \mathbf{r} - \mathbf{r}_d$ , and the vectors  $\mathbf{r}$  and  $\mathbf{r}_d$  are the observation point and the location of the source, which we assume to be a dipole (Stratton, 1941, Chapter 8) (see Figure 2.1). From (2.1) note that, in the electromagnetic wave regime, the magnetic field due to a magnetic dipole has terms that decay as  $R^{-1}$ ,  $R^{-2}$ , and  $R^{-3}$ . The range  $kR \gg 1$  is referred to as the far zone, and fields in this range are referred to as being in the far field. Similarly, fields in the near zone (with  $kR \ll 1$ ) are referred to as being in the near field, while the zone  $kR \approx 1$  is called the intermediate zone. Typically, UXO detection and discrimination are conducted in the near and intermediate zones during both land-based and underwater UXO cleanup. Additionally, in the EMI regime, displacement currents are considered irrelevant, which means that the contribution of the  $k^2$  term in (2.1) can be set to be zero. Under these assumptions we can take the dot product of (2.1) and  $\mathbf{R}$  and use (2.2) to show that

$$\mathbf{H} \cdot \mathbf{R} = \frac{1}{R^3} \left( \frac{3\mathbf{R}(\mathbf{R} \cdot \mathbf{m})}{R^2} - \mathbf{m} \right) \cdot \mathbf{R} \quad G(R, k) = 2 \frac{(\mathbf{R} \cdot \mathbf{m})}{R^3} G(R, k) = 2\psi, \quad (2.4)$$

where  $G(R, k) = (1 - jkR) e^{jkR} / 4\pi$ .

Similarly, we can take the *cross* product of (2.1) and  $\mathbf{R}$  and use (2.3) to obtain

$$\mathbf{H} \times \mathbf{R} = G(R, k) \frac{1}{R^3} \left( \frac{3\mathbf{R}(\mathbf{R} \cdot \mathbf{m})}{R^2} - \mathbf{m} \right) \times \mathbf{R} = -G(R, k) \frac{[\mathbf{m} \times \mathbf{R}]}{R^3} = \frac{-\mathbf{A}}{\mu_o}. \quad (2.5)$$

Now, taking the cross product of  $\mathbf{H}$  and (2.5) gives

$$\left[ \mathbf{H} \times \frac{-\mathbf{A}}{\mu_o} \right] = \mathbf{H} \times [\mathbf{H} \times \mathbf{R}] = \mathbf{H}(\mathbf{H} \cdot \mathbf{R}) - \mathbf{R} |\mathbf{H}|^2 = 2\mathbf{H} \psi - \mathbf{R} |\mathbf{H}|^2, \quad (2.6)$$

and from this we can solve for  $\mathbf{R}$ :

$$\mathbf{R} = \frac{2\mathbf{H} \cdot \boldsymbol{\psi} + [\mathbf{H} \times \mathbf{A} / \mu_o]}{|\mathbf{H}|^2}. \quad (2.7)$$

Thus if we assume that the source is a single dipole we can express its location vector  $\mathbf{R}$  in terms of only three global values. Moreover, this expression is independent of the frequency, which means that (2.7) is valid for both free space and conducting media such as water as long as the MQS assumption holds; *i.e.*, as long as we can neglect displacement currents. Note that  $\mathbf{R}$  is determined as a ratio between the three global values. This makes the expression in (2.7) partially tolerant to noise due to scaling arguments, since  $\mathbf{A}$  and  $\boldsymbol{\psi}$  depend on the  $\mathbf{H}$  field (*cf.* (2.4) and (2.5)). The magnetic dipole moment can be found by taking the cross product of  $\mathbf{R}$  and (2.3) and using (2.2):

$$\mathbf{m} = \frac{R}{G(\mathbf{R}, k)} (\mathbf{R} \boldsymbol{\psi} - [\mathbf{A} / \mu_o \times \mathbf{R}]), \quad (2.8)$$

where  $\mathbf{R}$  is determined from (2.7) (see Figure 2.1). Note that, for an isolated dipolar source, only a single instance of  $\mathbf{H}$ ,  $\mathbf{A}$ , and  $\boldsymbol{\psi}$  is needed to determine  $\mathbf{R}$  and  $\mathbf{m}$  uniquely.

### 2.3. A reduced HAP formulation for estimating a buried object's location and orientation

The analytic expressions (2.7) and (2.8) derived in the previous section require the magnetic field vector  $\mathbf{H}$ , the vector potential  $\mathbf{A}$ , and the scalar magnetic potential  $\boldsymbol{\psi}$  at a single location in space; the method uses seven global values to estimate the object's location, which, as we can see from (2.7), consists of only three unknown parameters. We now present a reduced HAP formulation that uses only the magnetic field and the scalar potential, thus decreasing the number of required global values and reducing computational requirements. Recalling that  $\mathbf{R} = \mathbf{r} - \mathbf{r}_d$ , where  $\mathbf{r}$  and  $\mathbf{r}_d$  are respectively the observation point and the dipole location in the global coordinate system (see Figure 2.1), we can write (2.4) as

$$\mathbf{H} \cdot (\mathbf{r} - \mathbf{r}_d) = 2\boldsymbol{\psi} \quad (2.9)$$

or

$$\mathbf{H} \cdot \mathbf{r}_d = -2\boldsymbol{\psi} + \mathbf{H} \cdot \mathbf{r}. \quad (2.10)$$

Since  $\mathbf{r}$ ,  $\mathbf{H}$  and  $\boldsymbol{\psi}$  are known at every observation point, the last equation can be rewritten in matrix form as follows:

$$\begin{bmatrix} H_{x,1} & H_{y,1} & H_{z,1} \\ H_{x,1} & H_{y,1} & H_{z,1} \\ \vdots & \vdots & \vdots \\ H_{x,N} & H_{y,N} & H_{z,N} \end{bmatrix} \begin{bmatrix} x_d \\ y_d \\ z_d \end{bmatrix} = \begin{bmatrix} -2\boldsymbol{\psi}_1 + \mathbf{H}_1 \cdot \mathbf{r}_1 \\ -2\boldsymbol{\psi}_2 + \mathbf{H}_2 \cdot \mathbf{r}_2 \\ \vdots \\ -2\boldsymbol{\psi}_N + \mathbf{H}_N \cdot \mathbf{r}_N \end{bmatrix}. \quad (2.11)$$

Under the low-frequency EMI assumption  $k^2 \rightarrow 0$ , equation (2.1) can be rewritten as

$$\mathbf{H} = \frac{\nabla \boldsymbol{\psi} \times \nabla \boldsymbol{\psi}}{|\nabla \boldsymbol{\psi}|^2}, \quad (2.12)$$

which lets us find the induced magnetic dipole moment via

$$\mathbf{m} = \frac{R}{G(\mathbf{R})} \left( \mathbf{R} \psi - [\mathbf{H} R^2] \right) \quad (2.13)$$

once we have determined  $\mathbf{R}$  from (2.11). Thus the location  $\mathbf{r}_d$  and the dipole moment  $\mathbf{m}$  of a single isolated dipolar source can be uniquely determined from  $\mathbf{H}$  and  $\psi$ .

## 2.4. Predicting the vector and scalar potentials from EMI data

As we have stated before, of the three global values ( $\mathbf{H}$ ,  $\mathbf{A}$ ,  $\psi$ ) needed to find location, orientation, and magnetic polarizability we have access only to the  $\mathbf{H}$  field (either one or all three components). Therefore we need to find a way to obtain the potentials  $\mathbf{A}$  and  $\psi$  from the measured magnetic field  $\mathbf{H}$  to be able to use our method.

Recently, new EMI sensors have been developed that can operate in both monostatic and multistatic data-collection regimes. Monostatic sensors, such as the Geophex GEM-3 frequency-domain instrument (Won *et al.*, 1997) and the Geonics EM-61 and EM-63 time-domain instruments (McNeill and Bosnar, 1996), have collocated transmitter and receiver coils. Multistatic sensors like the Man-Portable Vector (MPV) time-domain instrument from CRREL (Barrowes *et al.*, 2006), the Berkeley UXO Discriminator (BUD) system (Gasperikova, 2006), and the TD EMI array (Nelson and McDonald, 2001) have multiple transmitters and/or receiver coils. This section describes in detail the numerical procedure we use to estimate the vector potential  $\mathbf{A}$  and the scalar magnetic potential  $\psi$  using multistatic or monostatic EMI data. It is important to notice that each kind of data requires a different numerical scheme: in the case of multistatic data only one set of equivalent responding magnetic sources is needed to predict an object's EMI response at every measurement point (Dampney, 1969); on the other hand, in the monostatic case each data point requires a different set of responding magnetic sources, and this leads to an underdetermined ill-posed least-squares problem. The NSMS model was recently introduced to address these difficulties. The method uses one set of normalized magnetic sources to predict monostatic EMI data.

In this section we present two numerical procedures to estimate the vector potential  $\mathbf{A}$  and the scalar magnetic potential  $\psi$  starting from monostatic and multistatic data. For multistatic data we use the Method of Auxiliary Sources (Shubitidze *et al.*, 2002) and for monostatic data we employ the 2D NSMS model.

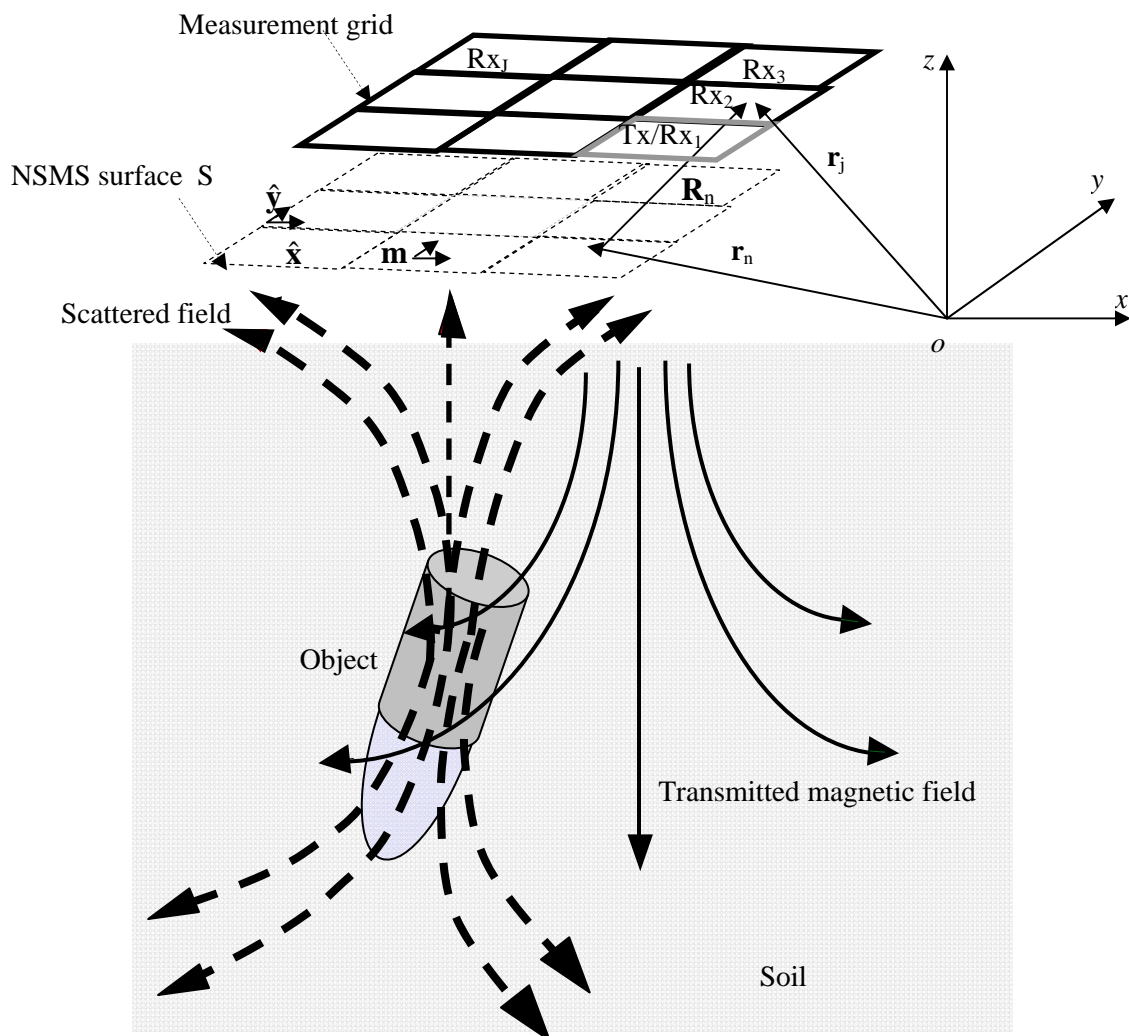


**Figure 2.2.** Multistatic EMI data survey scenario showing the intermediate NSMS surface. The potentials  $\mathbf{A}$  and  $\psi$  are obtained from sources on this surface which reproduce the dipolar target.

### 2.4.1. Determining vector and scalar potentials from multistatic data

Let an EMI sensor with one or more transmitters excite a highly conducting and permeable metallic object (see Figure 2.2). The object responds by producing a secondary magnetic field which is recorded by one or more receivers at different locations. Under this scenario, the primary magnetic field induces only one set of eddy currents or dipoles inside the object. Our goal is to estimate the scattered magnetic vector  $\mathbf{A}$  and scalar  $\psi$  potentials from the measured multistatic magnetic field data and then use these estimated potentials, together with the scattered magnetic field  $\mathbf{H}$ , to determine the buried object's location, orientation and magnetic polarizability using (2.7) and (2.8), or (2.11) and (2.13).

First, choose a fictitious planar surface  $S$  underneath the set of measurement positions but above the target itself, and assume that the scattered magnetic field  $\mathbf{H}_1^{\text{sc}}$  due to the target and its corresponding vector and scalar potentials  $\mathbf{A}_1^{\text{sc}}$  and  $\psi_1^{\text{sc}}$  are approximated by finding a set of surface magnetic dipoles placed on this surface (see Figure 2.2) which produce a magnetic field that most closely matches the secondary magnetic field produced by the target itself at the measurement locations. Let these approximated values be  $\tilde{\mathbf{H}}_1^{\text{sc}}$ ,  $\tilde{\mathbf{A}}_1^{\text{sc}}$ , and  $\tilde{\psi}_1^{\text{sc}}$ , where the tilde denotes that the values are approximated using the intermediate fictitious surface:

$$\tilde{\mathbf{H}}_1^{\text{sc}}(\mathbf{r}) = \int_S \frac{1}{R^3} \left( \frac{3\mathbf{R}(\mathbf{R} \cdot \mathbf{m})}{R^2} - \mathbf{m} \right) \cdot \mathbf{m} G(\mathbf{R}) ds' \quad (2.14)$$

$$\tilde{\psi}_1^{\text{sc}} = - \int_S \frac{(\mathbf{R} \cdot \mathbf{m})}{R^3} G(\mathbf{R}) ds' \quad (2.15)$$

$$\tilde{\mathbf{A}}_1^{\text{sc}} = \int_S \frac{(\mathbf{m} \times \mathbf{R})}{R^3} G(\mathbf{R}) ds' . \quad (2.16)$$

The auxiliary (or fictitious) surface  $S$  is divided into  $S_n$ ,  $n = 1, 2, \dots, N$ , subsurfaces, and on it we define a local Cartesian coordinate system using  $\hat{\mathbf{x}}$ ,  $\hat{\mathbf{y}}$ , and  $\hat{\mathbf{z}}$  (see Figure 2.2). According to Huygens's principle, the scattered magnetic field and the vector and scalar potentials can be reproduced by using a set of surface magnetic dipoles with only two independent components along  $\hat{\mathbf{x}}$  and  $\hat{\mathbf{y}}$ . Thus the unknown surface dipole moment for layer  $S$ ,  $\mathbf{m}(s')$ , can be written as

$$\mathbf{m}(s') = P^x(s') \hat{\mathbf{x}} + P^y(s') \hat{\mathbf{y}}; \quad (2.17)$$

here  $P^x(s')$  and  $P^y(s')$  are unknown. To determine  $P^\xi(s')$  ( $\xi = \{x, y\}$ ) for the entire surface  $s'$  we expand  $P^\xi(s')$  as

$$P^\xi(s') = \sum_{n=1}^N P_n^\xi F_n^\xi(s'), \quad (2.18)$$

where  $P_n^\xi$ ,  $n = 1, 2, 3, \dots, N$ , are expansion coefficients. For computational simplicity, in all subsequent analysis we will assume the expansion functions,  $F_n^\xi(s')$ , are a set of pulse functions given by

$$F_n^\xi(s') = \begin{cases} 1, & s' \in S_n \\ 0, & \text{otherwise.} \end{cases} \quad (2.19)$$

This expansion of  $F_n^\xi(s')$  results in a piecewise constant approximation to  $P^x(s')$  and  $P^y(s')$  on the fictitious surface  $S$ .

Substituting (2.18) into expression (2.14) for the magnetic field we obtain

$$\tilde{\mathbf{H}}_1^{sc}(\mathbf{r}) = \sum_{\xi=\rho,z} \sum_{n=1}^N \int_{S_n} P_n^\xi F_n^\xi(s') \left( 3\mathbf{R}_n(\mathbf{R}_n \cdot \mathbf{P}_n^\xi \hat{\xi}_n) - R_n^2 \hat{\xi}_n \right) \frac{G(R_n)}{R_n^5} ds', \quad (2.20)$$

where  $R_n = |\mathbf{r} - \mathbf{r}_n|$  is the distance between the observation point and the subsurface  $S_n$ . The potentials  $\tilde{\mathbf{A}}_1^{sc}$  and  $\tilde{\psi}_1^{sc}$  can be expressed in the same form as (2.20) after substituting (2.18) into (2.16) and (2.15) respectively. Using (2.19) in (2.20) enables us to write

$$\tilde{\mathbf{H}}_1^{sc}(\mathbf{r}) = \sum_{\xi=\rho,z} \sum_{n=1}^N P_n^\xi \int_{S_n} \left( 3\mathbf{R}_n(\mathbf{R}_n \cdot \hat{\xi}_n) - R_n^2 \hat{\xi}_n \right) \frac{G(R_n)}{R_n^5} ds'. \quad (2.21)$$

For convenience, we let

$$f(\mathbf{r}, \xi_n) = \int_{S_n} \left( 3\mathbf{R}_n(\mathbf{R}_n \cdot \hat{\xi}_n) - R_n^2 \hat{\xi}_n \right) \frac{G(R_n)}{R_n^5} ds'. \quad (2.22)$$

Then substituting (2.22) in (2.21) yields a numerical expression for the magnetic field at  $\mathbf{r}$  due to a magnetic dipole layer  $\mathbf{m}(s')$ :

$$\begin{aligned} \tilde{\mathbf{H}}_1^{sc}(\mathbf{r}) = & P_1^x f(\mathbf{r}, x_1) + P_2^x f(\mathbf{r}, x_2) + \dots + P_N^x f(\mathbf{r}, x_N) + \\ & P_1^y f(\mathbf{r}, y_1) + P_2^y f(\mathbf{r}, y_2) + \dots + P_N^y f(\mathbf{r}, y_N). \end{aligned} \quad (2.23)$$

The physical interpretation of this equation is as follows. A fictitious surface located in between a target and the measurement location(s) consisting of a surface magnetic dipole layer has been used to reproduce the magnetic field from an actual target. The fictitious surface has been divided up to  $N$  subsurfaces, with the  $P_n^\xi$  being an unknown constant over each subsurface. The amplitudes of the  $P_n^\xi$  surface magnetic sources can be determined by matching the sum of the magnetic fields produced from all  $N$  subsurfaces to the measured field  $\mathbf{H}^{\text{data}}(\mathbf{r})$  at  $\mathbf{r}$ . Usually, data are recorded at multiple points  $\mathbf{r}_j$ ,  $j = 1, 2, \dots, J$ . After matching the magnetic field produced by the fictitious surface layer to the magnetic field data at  $J$  points, the problem reduces to a linear system of equations which in compact matrix form can be written as

$$[\mathbf{Z}_{jn}] [\mathbf{P}_n^\xi] = [\mathbf{H}^{\text{data}}(\mathbf{r}_j)] \quad (2.24)$$

where  $[\mathbf{Z}_{jn}] = f(\mathbf{r}_j, \xi_n)$  is given by (2.22) and  $[\mathbf{H}^{\text{data}}(\mathbf{r}_j)]$  is the measured magnetic field at  $\mathbf{r}_j$ .

Using standard matrix algebra solution techniques for non-square systems of equations, the solution to (2.24) can be written symbolically as

$$\begin{bmatrix} P_n^\varepsilon \end{bmatrix} = \frac{\begin{bmatrix} \mathbf{Z}_{jn} \end{bmatrix}^T \begin{bmatrix} \mathbf{H}^{\text{data}}(\mathbf{r}_j) \end{bmatrix}}{\begin{bmatrix} \mathbf{Z}_{jn} \end{bmatrix}^T \begin{bmatrix} \mathbf{Z}_{jn} \end{bmatrix}}. \quad (2.25)$$

In order to find a unique solution,  $J$  must be larger than  $N$ . The number of subsurfaces  $N$  may be as few as 9 resulting from a  $3 \times 3$  grid.

Once  $[P_n^\varepsilon]$  is determined, all three global values: estimates of the  $\mathbf{H}$  magnetic field vector, and the  $\mathbf{A}$  and  $\psi$  potentials,  $\tilde{\mathbf{H}}_1^{\text{sc}}$ ,  $\tilde{\mathbf{A}}_1^{\text{sc}}$ , and  $\tilde{\psi}_1^{\text{sc}}$ , can be computed readily at any point in space using (2.14)–(2.16). After finding these estimates found from monostatic data, one can find the location  $\mathbf{R}$  and dipole moment,  $\mathbf{m}$  (and thereby the orientation, see below), using (2.7) and (2.8) respectively. Note that each subsurface source produces a separate  $\tilde{\mathbf{H}}_1^{\text{sc}}$ ,  $\tilde{\mathbf{A}}_1^{\text{sc}}$ , and  $\tilde{\psi}_1^{\text{sc}}$  (and thereby  $\mathbf{R}$  and  $\mathbf{m}$ ), and in practice these are averaged over  $N$  to produce a final estimated  $\mathbf{R}$  and  $\mathbf{m}$ . This concludes our treatment of multistatic data. In the next subsection we estimate the location and orientation of a subsurface target starting from monostatic measurements.

#### 2.4.2. Determining $\tilde{\mathbf{A}}_1^{\text{sc}}$ and $\tilde{\psi}_1^{\text{sc}}$ from monostatic data using NSMS

Many currently available EMI sensors, such as the Geonics EM-61 and EM-63 in the time domain and the Geophex GEM-3 in the frequency domain, are monostatic and have collocated transmitters and receivers. Usually during UXO surveying, the monostatic sensor is placed at multiple locations in order to obtain more information about a buried object: the impinging primary magnetic field around the scatterer changes with location, and so do the induced eddy currents inside the object. Thus there is not a unique set of eddy currents that will correctly reproduce a given object's monostatic data at multiple locations simultaneously. To relate monostatic data at multiple locations with some set of unique parameters, recently a new numerical technique called the normalized surface magnetic charge model (NSMC) was developed for a finite-sized object (Shamatava et al., 2004, Shubitidze et al., 2007). Here, the NSMC is generalized to the NSMS model (by utilizing dipole sources instead of charge sources) for predicting the scattered magnetic field vector and the scalar potentials using only measured EMI magnetic field data.

The NSMS approach assumes that the scattered magnetic field is produced by a set of magnetic dipoles placed on a fictitious surface  $S$ , just as in the multistatic case described above. The fictitious surface is again divided into small subsurfaces and at each subsurface (and for each monostatic measurement) the impinging (primary) magnetic field is determined. The amplitudes of the responding NSMS magnetic dipoles at each subsurface are scaled by the primary magnetic field:

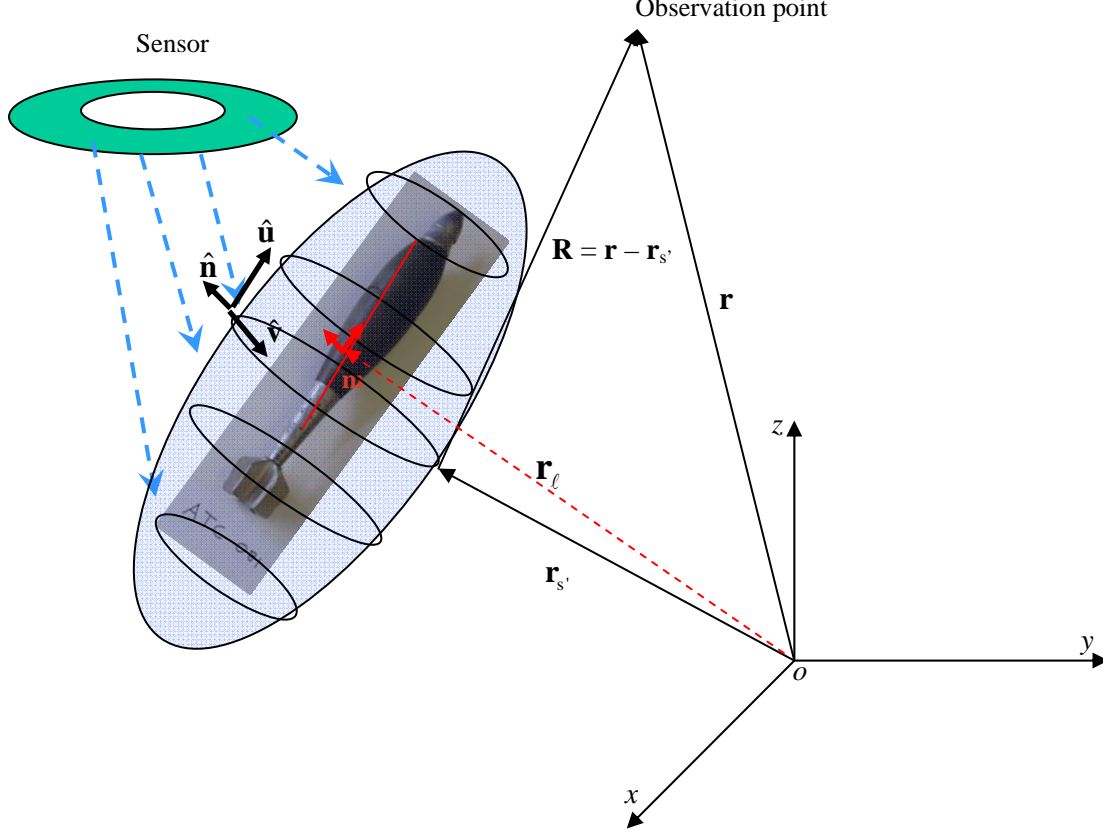


**Figure 2.3.** Geometry of the NSMS model.

$$\mathbf{m}(s') = P^x(s') H_x^{pr} \hat{\mathbf{x}} + P^y(s') H_y^{pr} \hat{\mathbf{y}}. \quad (2.26)$$

This is the main difference between the multistatic section above and the present monostatic NSMS formulation. The scattered magnetic field in the monostatic case is then determined to be

$$\tilde{\mathbf{H}}_1^{sc}(\mathbf{r}) = \sum_{\xi=\rho,z} \sum_{n=1}^N P_n^\xi \int_{S_n} H_{\xi_n}^{pr} \left( 3\mathbf{R}_n (\mathbf{R}_n \cdot \hat{\xi}_n) - R_n^2 \hat{\xi}_n \right) \frac{G(R_n)}{R_n^5} ds'. \quad (2.27)$$

After following the same procedure as in the previous section, the amplitudes of the NSMC are determined by matching  $\tilde{\mathbf{H}}_1^{sc}$  from (2.27) to the measured field,  $\mathbf{H}^{\text{data}}(\mathbf{r}_j)$ , at a selected set of measurement points  $\mathbf{r}_j$ ,  $j = 1, 2, \dots, J$ . Once the amplitudes  $[P_n^\xi]$  of this source set are found, the scattered EMI field and its corresponding potentials can be determined at any point. For more details on NSMS refer to the next section. Note that in order to avoid ill-conditioning, the number of data points  $J$  must not be smaller than the number of patches  $N$ .



## 2.5. The Normalized Surface Magnetic Source model

The NSMS model can be considered as an extended version of the multi-dipole model. According to the NSMS model, an object's response to a sensor's primary field is modeled mathematically by a set of equivalent magnetic dipoles distributed over a surface surrounding the object. The amplitudes of the equivalent responding magnetic dipoles, which are oriented normally to the surrounding surface, are normalized by the component of the primary magnetic field normal to the surface. The amplitude  $\Omega$  of the dipole sources is a property of the object, and its integral  $Q$  over the surface constitutes a global magnetic "capacitance" of sorts that relates the induced double layer charge density to the normal component of the primary magnetic field,  $H_n^{pr}$ . Thus the scattered magnetic field of the NSMS is identical to that produced by a layer of magnetic dipoles distributed over the surface. It can be considered that such a surface distribution is generated by spreading positive charge density over the *positive* side (with respect to the surface normal) of a smooth surface and an identical distribution of opposite sign on its negative side. The result is a double layer of magnetic charge separated by an infinitesimal distance. According to the Huygens equivalence principle, an object's EMI response can be reproduced with a set of equivalent single or double layer magnetic charges. The double layer charge density introduces the proper discontinuities in the tangential components of magnetic flux density vector  $\mathbf{B}$ , but does not affect the transition of the normal component of  $\mathbf{B}$ . The single layer charge density, on the other hand, in no way affects the transition of the tangential components but accounts for the proper discontinuity in the normal component of the vector  $\mathbf{B}$ . Since the normal component of the magnetic flux density vector is always continuous on the boundary between two media (there are no free magnetic charges in nature), the secondary magnetic field outside the object can be accounted for by a layer of magnetic dipoles with density  $\Omega$  distributed on an auxiliary/surrounding surface.

In order to illustrate the similarity between the multi dipole and NSMS approaches, let us briefly describe the multi-dipole model approximation (Shubitidze *et al.*, 2008). In the multi dipole approximation the EMI response of the whole object is represented by a set of magnetic dipoles distributed on a line along the object's elongation axis (red line on Figure 2.3). Mathematically, the secondary magnetic field due to a set of dipoles of moment  $\mathbf{m}(\ell')$  along the line  $L$  can be written as

$$\mathbf{H}^{sc} = \int_L \frac{1}{4\pi\mu_0 R^3} \mathbf{m}(\ell') \cdot (3\hat{\mathbf{R}}\hat{\mathbf{R}} - \bar{\mathbf{I}}) d\ell', \quad (2.28)$$

where  $\hat{\mathbf{R}}$  is the unit vector along  $\mathbf{R} = \mathbf{r} - \mathbf{r}_\ell$ ,  $\mathbf{r}_\ell$  is the position of the dipole on line  $L$ ,  $\mathbf{r}$  is the observation point (see Figure 2.1),  $\bar{\mathbf{I}}$  is the identity dyad, and  $\mathbf{m}(\ell')$  is the induced magnetic dipole along  $L$ . The induced magnetic dipole is related to the primary field via  $\mathbf{m}(\ell') = \bar{\bar{\mathbf{M}}}(\ell') \cdot \mathbf{H}^{pr}(\ell')$ , where the polarizability tensor  $\bar{\bar{\mathbf{M}}}(\ell')$  is assumed to be varying along the line and to have the form

$$\bar{\bar{\mathbf{M}}}(\ell') = \begin{bmatrix} m_{xx}(\ell') & 0 & 0 \\ 0 & m_{yy}(\ell') & 0 \\ 0 & 0 & m_{zz}(\ell') \end{bmatrix}, \quad (2.29)$$

where  $m_{xx}(\ell')$ ,  $m_{yy}(\ell')$ , and  $m_{zz}(\ell')$  are the moments along the principal axes of  $\bar{\bar{\mathbf{M}}}(\ell')$  at point  $\ell'$  on  $L$ . The multi dipole model is a fast algorithm, and it takes into account an object's geometric and electromagnetic (heterogeneity) variations along  $L$ . However, actual objects have finite size, and the primary magnetic field can vary not only along the axis of symmetry but along the circumference axis as well. To take into account geometric variations along the circumference axis let us extend the multi dipole model by distributing the dipoles on a closed surface. Thus, the total scattered magnetic field produced by the surface magnetic dipoles (*i.e.*, the NSMS system) can be written as

$$\mathbf{H}^{sc} = \int_s \frac{1}{4\pi\mu_0 R^3} \mathbf{m}(\mathbf{r}_{s'}) \cdot (3\hat{\mathbf{R}}\hat{\mathbf{R}} - \bar{\bar{\mathbf{I}}}) ds', \quad (2.30)$$

where the induced magnetic dipole  $\mathbf{m}(\mathbf{r}_{s'})$  on the surface at point  $\mathbf{r}_{s'}$  is related to the primary field via  $\mathbf{m}(\mathbf{r}_{s'}) = \bar{\bar{\mathbf{M}}}(\mathbf{r}_{s'}) \cdot \mathbf{H}^{pr}(\mathbf{r}_{s'})$ . In the NSMS approach the polarizability tensor  $\bar{\bar{\mathbf{M}}}(\mathbf{r}_{s'})$  in a local curvilinear coordinate system  $(\hat{\mathbf{u}}(\mathbf{r}_{s'}), \hat{\mathbf{v}}(\mathbf{r}_{s'}), \hat{\mathbf{n}}(\mathbf{r}_{s'}))$  is assumed to have only one nonzero principal axis along the normal direction  $\hat{\mathbf{n}}(\mathbf{r}_{s'})$ , and since

$$\mathbf{H}^{pr}(\mathbf{r}_{s'}) = H_u^{pr}(\mathbf{r}_{s'})\hat{\mathbf{u}}(\mathbf{r}_{s'}) + H_v^{pr}(\mathbf{r}_{s'})\hat{\mathbf{v}}(\mathbf{r}_{s'}) + H_n^{pr}(\mathbf{r}_{s'})\hat{\mathbf{n}}(\mathbf{r}_{s'})$$

we have

$$\mathbf{m}(\mathbf{r}_{s'}) = \Omega(\mathbf{r}_{s'}) H_n^{pr}(\mathbf{r}_{s'}) \hat{\mathbf{n}}(\mathbf{r}_{s'}), \quad (2.31)$$

where  $\Omega(\mathbf{r}_{s'})$  is the amplitude of the magnetic dipole at point  $\mathbf{r}_{s'}$  on the spheroidal surface. Overall, in the NSMS approach the scattered magnetic field is approximated as a sum of magnetic fields radiated by elementary magnetic sources (magnetic charges or dipoles) distributed on an auxiliary closed surface. The amplitudes of these responding magnetic charges at each point on the surface are normalized by the normal component of the impinging primary magnetic field,  $H_n^{pr}$ . At the end the scattered field is expressed by the proportionality constant  $\Omega(s')$ :

$$\mathbf{H}^{sc}(t, \mathbf{r}) = \int_s \frac{1}{4\pi\mu_0 R^3} \Omega(t, \mathbf{r}_{s'}) H_n^{pr}(\mathbf{r}_{s'}) (\hat{\mathbf{n}}(\mathbf{r}_{s'}) \cdot (3\hat{\mathbf{R}}\hat{\mathbf{R}} - \bar{\bar{\mathbf{I}}})) ds'. \quad (2.32)$$

The quantity  $\Omega(t, s')$  is essentially a normalized charge density, corresponding to a primary field  $H_n^{pr} = 1$  A/m. For discrimination purposes we propose using a single variable equal to the total normalized magnetic charge. This is a global measure of  $\Omega$  for the entire object and is thus less subject to numerical fluctuation than the individual  $\Omega(t, s')$  values:

$$Q(t) = \int_s \Omega(t, s') ds' \quad (2.33)$$

Our studies have showed that the total NSMS  $Q$  is invariant for a given object, in the sense that different computational constructs (*e.g.*, surrounding surfaces) and different primary fields produce the same value. Once the amplitudes of the NSMS are determined the scattered EM fields can be calculated extremely fast and accurately for any known object and any type of EMI sensor. Thus the NSMS model can be considered a complete, unified fast forward dipole model of EMI

scattering for use in discrimination processing that relies on comparing received fields to those produced by a library of known objects. In such “pattern matching” discrimination processing, an optimization or search algorithm is used to determine what configuration of known UXO types and sensor best reproduces the received signal, for catalogued  $\Omega(t, s')$  distributions associated with those UXO.

## 2.6. A numerical procedure for estimating orientation

The Method of Auxiliary Sources (MAS) (Shubitidze *et al.* 2002), approximates an object’s response to a given excitation as the summation of magnetic fields produced by elementary magnetic dipoles or charges placed inside the object. Using the superposition principle, this set of dipoles can be further approximated as one independent aggregate dipole which can then be compared to the simple dipole model commonly in use. According to the simple dipole model (Pasion and Oldenburg, 2001), the secondary magnetic field due to the dipole  $\mathbf{m}$  is

$$\mathbf{H} = \frac{1}{4\pi\mu_0 R^3} \mathbf{m} \cdot (3\hat{\mathbf{R}}\hat{\mathbf{R}} - \bar{\bar{\mathbf{I}}}), \quad (2.34)$$

where  $\hat{\mathbf{R}}$  is the unit vector along  $\mathbf{R} = \mathbf{r} - \mathbf{r}_d$ ,  $\mathbf{r}_d$  is the dipole’s position,  $\mathbf{r}$  is the observation point, and  $\bar{\bar{\mathbf{I}}}$  is the identity dyad (see Figure 2.1). The dipole moment  $\mathbf{m}$  induced by the primary magnetic field  $\mathbf{H}^{pr}$  is given by

$$\mathbf{m} = \bar{\bar{\mathbf{M}}} \cdot \mathbf{H}^{pr}(\mathbf{r}, \mathbf{r}_d), \quad (2.35)$$

where  $\bar{\bar{\mathbf{M}}}$  is the target’s magnetic polarizability tensor. This tensor depends on the scatterer’s shape, size, and material properties. In a coordinate system not aligned with the scatterer’s principal axes for different primary magnetic fields  $\mathbf{H}^{pr}(\mathbf{r}_j, \mathbf{r}_d)$ ,  $j = 1, 2, \dots, J$ , equation (2.35) can be written in matrix form as

$$[\mathbf{m}] = \bar{\bar{\mathbf{M}}} \cdot [\mathbf{H}^{pr}], \quad (2.36)$$

where

$$[\mathbf{m}] = \begin{bmatrix} m_x^1 & \dots & m_x^J \\ m_y^1 & \dots & m_y^J \\ m_z^1 & \dots & m_z^J \end{bmatrix} \quad \text{and} \quad [\mathbf{H}^{pr}] = \begin{bmatrix} H_x^{pr}(\mathbf{r}_1, \mathbf{r}) & \dots & H_x^{pr}(\mathbf{r}_J, \mathbf{r}) \\ H_y^{pr}(\mathbf{r}_1, \mathbf{r}) & \dots & H_y^{pr}(\mathbf{r}_J, \mathbf{r}) \\ H_z^{pr}(\mathbf{r}_1, \mathbf{r}) & \dots & H_z^{pr}(\mathbf{r}_J, \mathbf{r}) \end{bmatrix}. \quad (2.37)$$

Equation (2.36) can be solved for the magnetic polarizability  $\bar{\bar{\mathbf{M}}}$ :

$$\frac{[\mathbf{m}] [\mathbf{H}^{pr}]^T}{[\mathbf{H}^{pr}] [\mathbf{H}^{pr}]^T} = \bar{\bar{\mathbf{M}}}. \quad (2.38)$$

Once  $\bar{\bar{\mathbf{M}}}$  is determined, the principal target and the global coordinate systems can be related via the Euler rotation tensor,  $\bar{\bar{\mathbf{A}}}(\psi, \theta, \phi)$ , which is an orthogonal matrix:  $\bar{\bar{\mathbf{A}}}^{-1} = \bar{\bar{\mathbf{A}}}^T$ . Using the eigendecomposition theorem one can write  $\bar{\bar{\mathbf{M}}}$  as

$$\bar{\bar{\mathbf{M}}} = \bar{\bar{\mathbf{A}}} \bar{\bar{\beta}} \bar{\bar{\mathbf{A}}}^T, \quad (2.39)$$

where

$$\bar{\bar{\beta}} = \begin{bmatrix} \beta_{xx} & 0 & 0 \\ 0 & \beta_{yy} & 0 \\ 0 & 0 & \beta_{zz} \end{bmatrix}. \quad (2.40)$$

For a body of revolution (BOR) (which includes most UXO)  $\beta_{xx} = \beta_{yy}$ , and because of BOR symmetry the third Euler angle  $\psi$  is zero, and thus

$$\bar{\bar{\mathbf{A}}} = \begin{bmatrix} \cos \theta \cos \phi & \cos \theta \sin \phi & -\sin \theta \\ -\sin \phi & \cos \phi & 0 \\ \sin \theta \cos \phi & \sin \theta \sin \phi & \cos \theta \end{bmatrix}, \quad (2.41)$$

where  $\theta$  and  $\phi$  are the angles between the local and global axes. Equation (2.39) can be rewritten as

$$\bar{\bar{\mathbf{A}}}^T \bar{\bar{\mathbf{M}}} \bar{\bar{\mathbf{A}}} = \bar{\bar{\beta}}. \quad (2.42)$$

Since  $\bar{\bar{\mathbf{M}}}$  is determined from (2.38) and the  $\bar{\bar{\mathbf{A}}}$  are given explicitly, from (2.42) we can determine  $\theta$  and  $\phi$  values that give minimum/zero values of the off-diagonal elements of  $\bar{\bar{\beta}}$ .

## 2.7. Matrix diagonalization

To determine the matrices  $\bar{\bar{\mathbf{A}}}$  and  $\bar{\bar{\beta}}$  we employ a simultaneous matrix diagonalization technique that uses the Jacobi angles to build a unitary orthogonal matrix  $\bar{\bar{\mathbf{A}}}$ . Namely, consider a set  $|\bar{\bar{\mathbf{M}}} = \{\bar{\bar{\mathbf{M}}}_t | t=1, N_t\}$  of  $N_t$   $3 \times 3$  matrices. When the matrices in  $|\bar{\bar{\mathbf{M}}}$  are normal commuting matrices, their off-diagonal terms can be set to zero by a unitary transform, thus simultaneously diagonalizing the set  $|\bar{\bar{\mathbf{M}}}$ .

$$\min (\text{of } |\bar{\bar{\mathbf{M}}}) = \sum_{1 \leq it \neq jt \leq 3} \left| \bar{\bar{\mathbf{M}}}_{it,jt} \right|^2. \quad (2.43)$$

$\bar{\bar{\mathbf{M}}}_{it,jt}$  denotes the  $(it, jt)$ -th entry of matrix  $|\bar{\bar{\mathbf{M}}}$ . The simultaneous diagonalization is obtained by minimizing the composite objective function  $\sum_{t=1, N_t} |\bar{\bar{\mathbf{A}}} \bar{\bar{\mathbf{M}}}_t \bar{\bar{\mathbf{A}}}^T|^2$  by a unitary matrix  $\bar{\bar{\mathbf{A}}}$ .

## 2.8. Results

### 2.8.1. Estimating the location of a buried object using synthetic EMI data

In this section we present results of numerical experiments to demonstrate the applicability of the physics-based method for determining a buried object's location without solving a time-consuming minimization problem. First, the proposed algorithm is tested for the case of a single dipole source, with dipole moment  $\mathbf{m}$ , placed in free space ( $k = 0$ ) at different depths below an arbitrary measurement plane with no primary field. In these tests, the measurement plane was divided into grid points ( $40 \times 40$ ), and at each point on the grid the magnetic field, scalar and vector potentials were calculated from the single dipole source on the fictitious surface using equations (2.1)–(2.3) for the magnetic dipole  $\mathbf{m} = (1, 1, 2)$ . Then, using these values of  $\mathbf{H}$ ,  $\mathbf{A}$ , and  $\psi$ , the dipole's location was determined using (2.7) at each grid point. The synthetic test is done for four cases:  $h = 1, 10, 30$ , and  $40$  cm below the measurement surface. The inverted location of the magnetic dipole is depicted in Figure 2.4.

The results show that the proposed algorithm inverts the dipole's location from each point very accurately, *i.e.* for determining the dipole's location, only  $\mathbf{H}$ ,  $\mathbf{A}$ , and  $\psi$  at a single point (each grid point separately) are needed. In addition, results indicate that the approach is applicable in the near ( $h = 1$  cm) as well as far field ( $h = 41$  cm).

In order to test the effects that the presence of multiple dipoles would have on the algorithm (which assumes only one dipole source), similar tests were done for three separate source dipoles, each with  $\mathbf{m} = (1, 1, 2)$ , placed at  $[x, y, z] = [-5, 0, 14]$  cm,  $[x, y, z] = [-5, 0, 19]$  cm

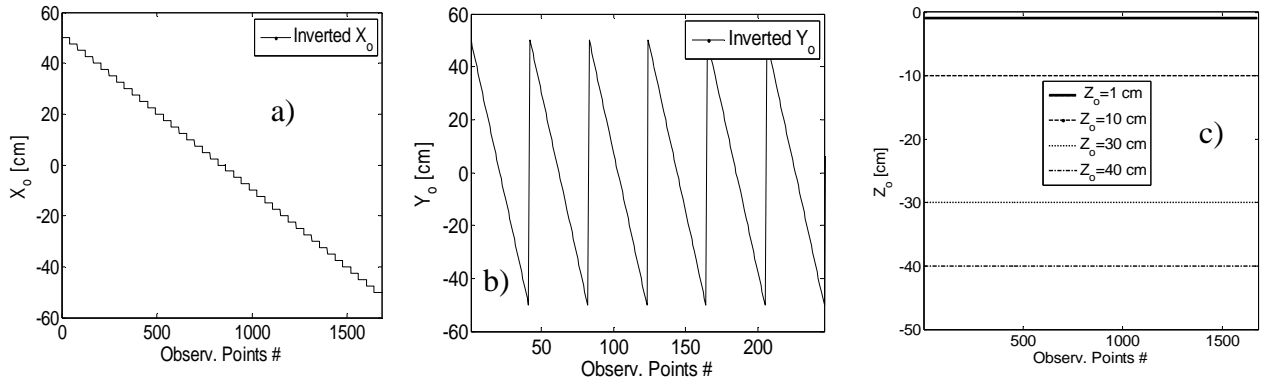


**Figure 2.4.** Inverted coordinates (a)  $x_o$ , (b)  $y_o$  and (c)  $z_o$  for a dipole. Inverted locations for these synthetic tests are essentially exact and demonstrate the viability of this method.

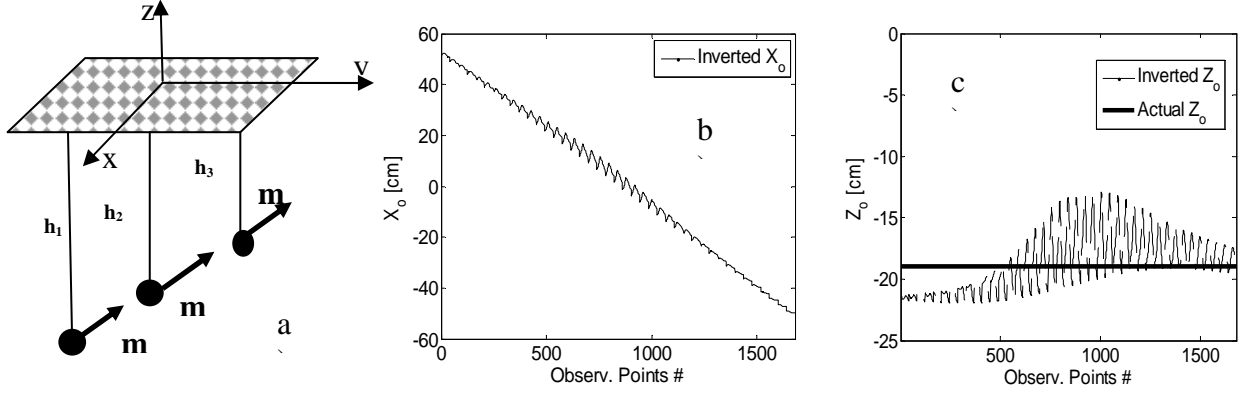


**Figure 2.5.** Three source dipoles at different depths: (a) Problem geometry. Inverted coordinates of inverted aggregate dipole (b)  $x_0$ , and (c)  $z_0$ .

### 2.8.2 Predicting a dipole's orientation from monostatic synthetic data

Here we test the new approach for estimating a dipole's orientation from monostatic field data. The dipole with magnetic polarizability  $\bar{\bar{\beta}}$  tensor  $\text{diag}(\bar{\bar{\beta}}) = (1, 2, 3)$  is placed 30 cm below the measurement surface. The dipole is illuminated with the virtual EM-63 sensor, and monostatic sensor data are collected over a  $60 \text{ cm} \times 60 \text{ cm}$  measurement surface divided into  $25 \times 25$  grid points. The monostatic means that the transmitter and receiver are always co-located i.e. when it is located at some particular point on measurement surface the sensor records only the scattered field at that point produced by the primary field transmitted from that point. Each data point is from a different scattered field, as each result from a different excitation of the dipole. At each point on the grid the magnetic field, scalar and vector potentials were calculated from the magnetic dipole with polarizability  $\bar{\bar{\beta}}$  tensor  $\text{diag}(\bar{\bar{\beta}}) = (1, 2, 3)$  on the measurement surface using (2.1)–(2.3) and the simple dipole model approximation (2.35). First, using these values of  $\mathbf{H}$ ,  $\mathbf{A}$ , and  $\psi$ , the dipole's location was estimated using (2.7), and then using the predicted values of location, the dipole's magnetic polarizability tensor  $\bar{\bar{\mathbf{M}}}$  was determined from (2.8) and (2.38). Finally, the dipole's orientation  $(\psi, \theta, \phi)$  that gives minimum/zero values of the  $\bar{\bar{\beta}}$  matrix's off-diagonal elements and diagonal elements of  $\bar{\bar{\beta}}$  were estimated. The numerical tests are done for five cases and summarized in Table 2.1. For these numerical studies, a comparison between estimated and true values for the orientation shows an excellent match. Note that the estimated values of  $\bar{\bar{\beta}}$  diagonal elements exactly matched with the actual  $\text{diag}(\bar{\bar{\beta}}) = (1, 2, 3)$  values as well.

### 2.8.3 Noise effect: predicting a dipole's orientation from monostatic noisy synthetic data

In this section we studied the robustness of the reduced HAP approach with respect to noise for a dipole source. We consider the same dipole with magnetic polarizability  $\bar{\bar{\beta}}$  tensor  $\text{diag}(\bar{\bar{\beta}}) = (1, 2, 3)$  oriented with Euler angles  $(\theta = 45^\circ, \phi = 30^\circ, \psi = 60^\circ)$  and placed 35 cm below the measurement surface. The dipole is illuminated with the virtual EM-63 sensor, and monostatic

sensor data are collected over a  $40 \text{ cm} \times 40 \text{ cm}$  measurement surface divided into  $21 \times 21$  grid points. The distribution of the scattered magnetic field and the scalar potential without (left) and with (right) noise are depicted on Figure 2.6. As before at each point on the grid the magnetic field and scalar potential were calculated from the magnetic dipole, on the measurement surface using (2.1)–(2.3) via the basic simple dipole model approximation (see distribution on the left column of Figure 2.6). Then at each point on the measurement surface a random Gaussian random noise were to both field and scalar potentials. The noise generated this way is better suited to simulating sensor noise than to modeling positional uncertainty. The noisy data distribution are plotted on Figure 2.6 left. Using these values of  $\mathbf{H}$  and  $\psi$  (Figure 2.6, left), the dipole's location was estimated by using (2.11) and then, using the predicted values of location, the dipole's magnetic polarizability tensor  $\bar{\bar{\mathbf{M}}}$  was determined from (2.13) and (2.38). Finally, using the joint orthogonal diagonalization technique (2.43) the  $\bar{\bar{\mathbf{M}}}$  matrix's diagonal elements and orientations ( $\theta, \phi, \psi$ ) were estimated. The numerical test is summarized in Table 2.2. For these numerical studies, the comparison between estimated and true values for the orientation show very close matches.

**Table 2.1.** Estimated and actual orientation of a dipole using a synthetic data set.

Case	Estimated			Actual		
	$\theta (^{\circ})$	$\phi (^{\circ})$	$\Psi (^{\circ})$	$\theta (^{\circ})$	$\phi (^{\circ})$	$\Psi (^{\circ})$
<b>1</b>	45	3	1.8	<b>45</b>	<b>3</b>	<b>1.8</b>
<b>2</b>	45	30	18	<b>45</b>	<b>30</b>	<b>18</b>
<b>3</b>	60	45	90	<b>60</b>	<b>45</b>	<b>90</b>
<b>4</b>	30	20	60	<b>30</b>	<b>20</b>	<b>60</b>
<b>5</b>	36	45	45	<b>36</b>	<b>45</b>	<b>45</b>

**Table 2.2.** Estimated and actual orientation for the dipole using noisy data.

Estimated									Actual								
$X_o(\text{cm})$	$Y_o(\text{cm})$	$Z_o(\text{cm})$	$\theta(^{\circ})$	$\phi(^{\circ})$	$\psi (^{\circ})$	$\beta_1$	$\beta_2$	$\beta_3$	$X_o(\text{cm})$	$Y_o(\text{cm})$	$Z_o(\text{cm})$	$\theta(^{\circ})$	$\phi(^{\circ})$	$\psi (^{\circ})$	$\beta_1$	$\beta_2$	$\beta_3$
2.2	1.5	-35.36	44	34	64	1.03	1.98	2.96	<b>0</b>	<b>0</b>	<b>-36</b>	<b>45</b>	<b>35</b>	<b>60</b>	<b>1</b>	<b>2</b>	<b>3</b>

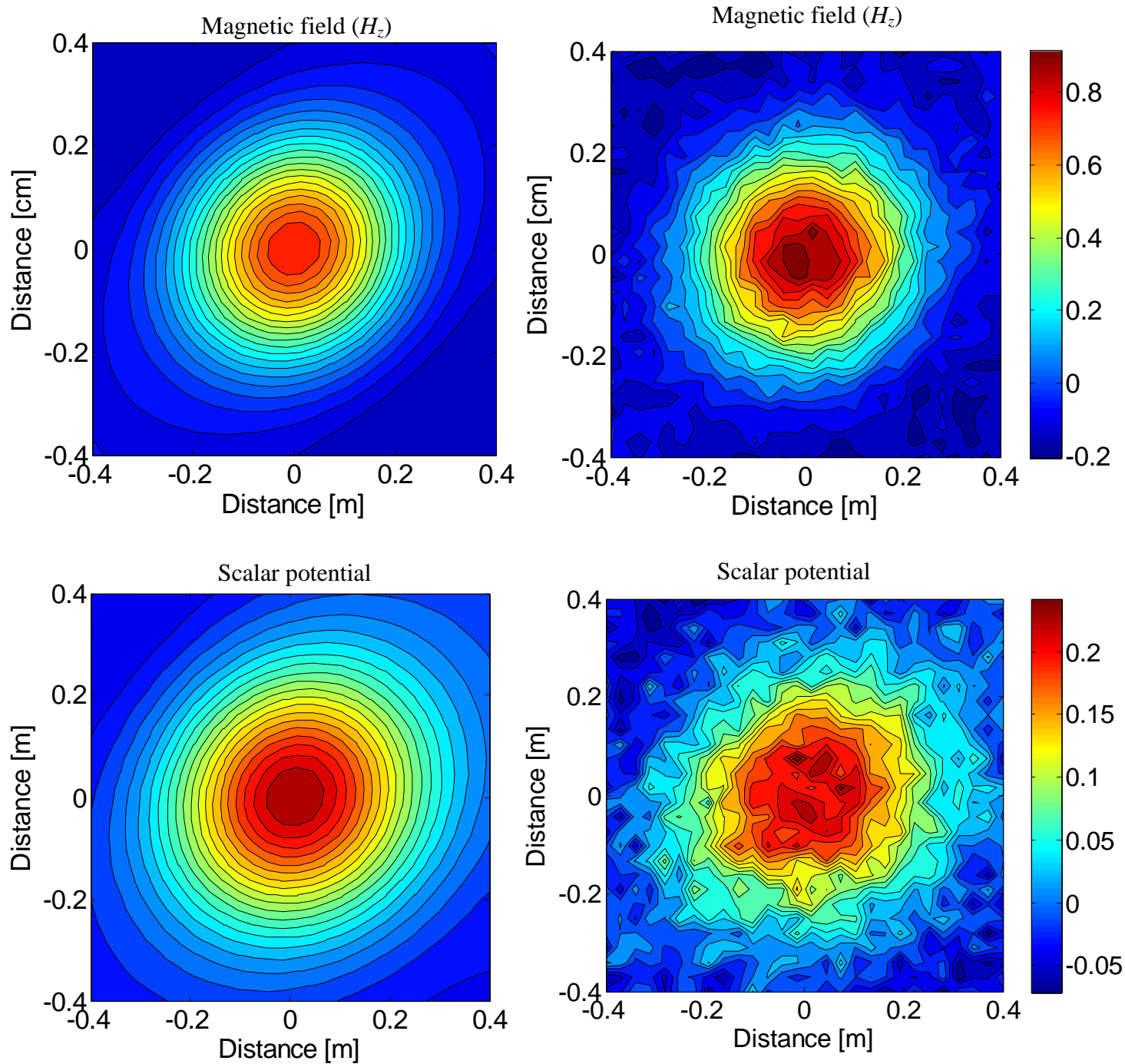


**Figure 2.6.** Scattered magnetic field and scalar magnetic potential for a dipole source. Left: no noise added; right: noise added.



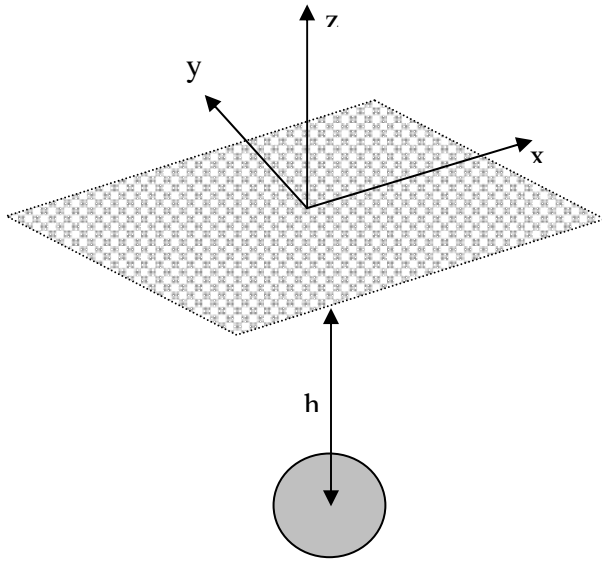


**Figure 2.7.** Problem geometry for a sphere under the measurement plane.

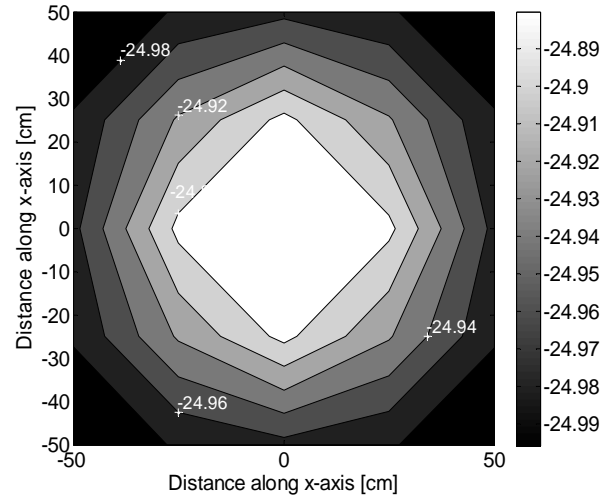


**Figure 2.8.** Estimated  $z_c$  for the sphere in Figure 2.7.

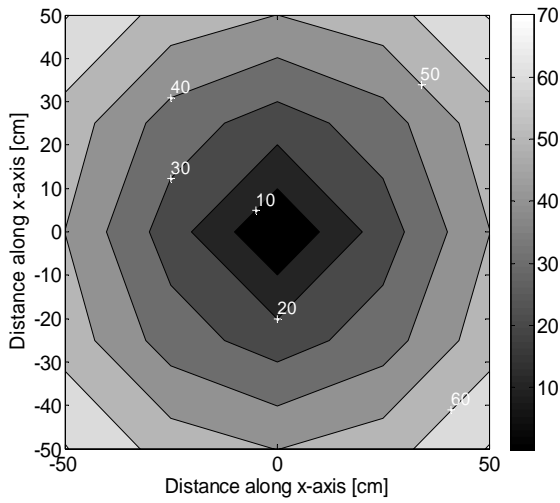


**Figure 2.9.** Estimated  $\sqrt{x_c^2 + y_c^2}$  for the sphere in Figure 2.7.

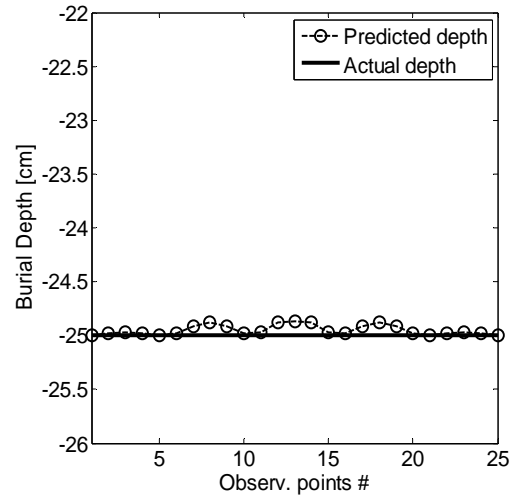


**Figure 2.10.** Estimated  $z_c$  for the sphere in Figure 2.7 vs. observation point.

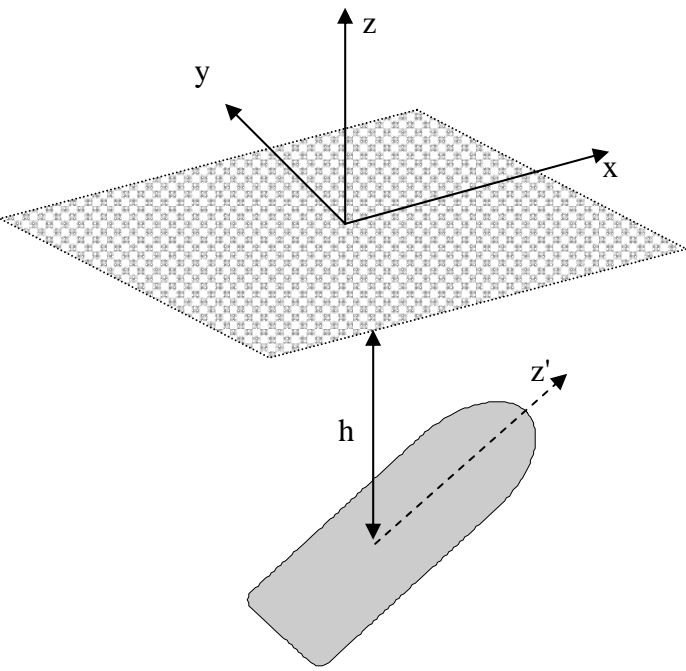


**Figure 2.11.** Geometry of the problem for a homogeneous object.

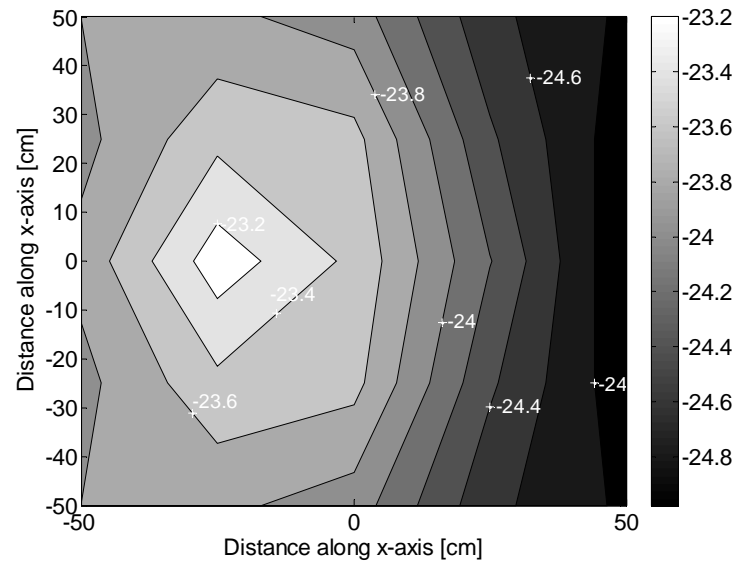


**Figure 2.12.** Estimated  $z_c$  for the bullet of Figure 2.11.

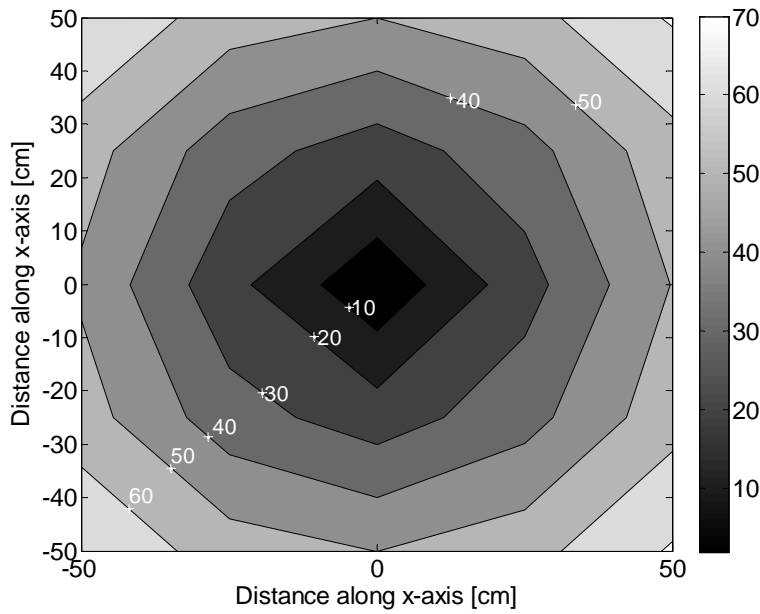


**Figure 2.13.** Estimated  $\sqrt{x_c^2 + y_c^2}$  for the bullet of Figure 2.11.

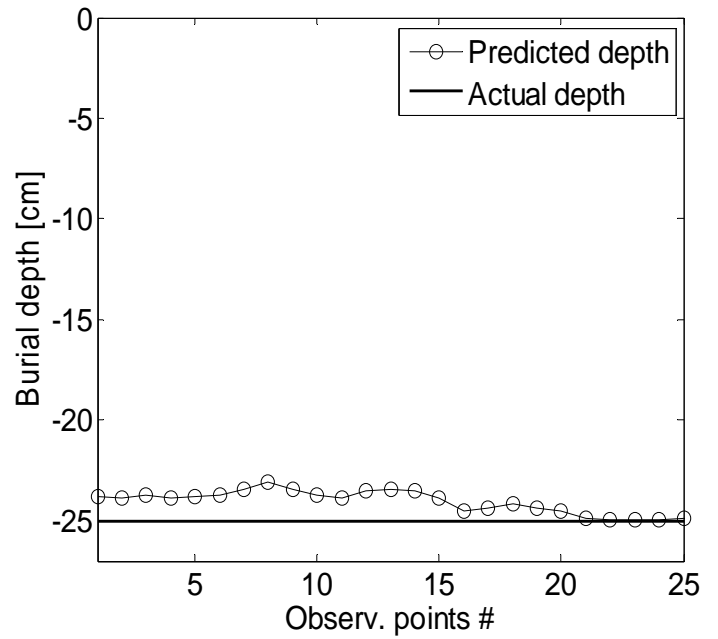


**Figure 2.14.** Estimated  $z_c$  for the bullet in Figure 2.11 vs. observation point.

#### 2.8.4. Studies for a highly conducting and permeable sphere

Next, the algorithm was applied to the synthetic EMI response from a highly conducting and permeable metallic sphere, with radius  $a = 5$  cm, permeability  $\mu_r = 100$ , and conductivity  $\sigma = 4 \times 10^6$  S/m. The sphere is placed at  $[x_c, y_c, z_c] = [0, 0, -25]$  cm (Figure 2.7) and illuminated with a time-varying magnetic field generated by a virtual Geophex GEM-3 sensor (Won *et al.*, 1996). The sensor's primary magnetic field is modeled as the field radiated by two concentric coils. The current amplitudes in the coils are chosen in such a way that at the center of the concentric coils, where the receiving coil resides, the primary magnetic field is zero. The measurement plane is again divided into grid points, and the GEM-3 sensor is swept over the grid points in 25-cm increments resulting in a  $5 \times 5$  grid of measurement locations. At each measurement position a separate EMI problem is solved using the MAS EMI-BOR code and the scattered magnetic field and scalar and vector potentials ( $\mathbf{H}_1^{\text{sc}}$ ,  $\mathbf{A}_1^{\text{sc}}$ , and  $\psi_1^{\text{sc}}$ ) are calculated at the sensor's center, *i.e.* a synthetic mono-static data set is created. Using this  $\mathbf{H}_1^{\text{sc}}$ ,  $\mathbf{A}_1^{\text{sc}}$ , and  $\psi_1^{\text{sc}}$ , the sphere's center  $[x_c, y_c, z_c]$  is determined using (2.7) at each grid point. Figures 2.8 and 2.9 show the predicted  $z_c$  and  $\sqrt{x_c^2 + y_c^2}$  over the  $x$ - $y$  measured plane using the analytic inversion algorithm presented in this paper. The results show that the algorithm predicts the sphere's center location with reasonable accuracy at each measurement point. Figure 2.10 shows a comparison between the predicted and actual  $z_c$  for each observation point. The results demonstrate that knowing  $\mathbf{H}_1^{\text{sc}}$ ,  $\mathbf{A}_1^{\text{sc}}$ , and  $\psi_1^{\text{sc}}$  at any given point is enough to estimate the buried sphere's location.

#### 2.8.5. Studies for non-spherical and heterogeneous objects

The sphere is the simplest 3D geometrical figure, and its EMI response can be represented very well with a magnetic dipole. However, in order to demonstrate the applicability of this new-physics based algorithm, in this section we present additional numerical studies for homogeneous (Figures 2.11–2.14) and heterogeneous (Figures 2.15–2.18) objects. The homogeneous object's geometrical and electromagnetic parameters are: nose radius  $a = 2.5$  cm, overall length 18 cm, relative permeability  $\mu_r = 100$ , and conductivity  $\sigma = 4 \times 10^6$  S/m. The heterogeneous object's parameters are: overall length 28 cm, nose radius 2.5 cm, relative permeability  $\mu_r = 100$ , and conductivity  $\sigma = 4 \times 10^6$  S/m for the bottom cylindrical part, while the nose has  $\mu_r = 30$  and  $\sigma = 5 \times 10^7$  S/m.

The objects are placed at  $[x_c, y_c, z_c] = [0, 0, -25]$  cm (see Figures 2.11 and 2.15) and oriented at  $45^\circ$  with respect to the vertical. As in the case of the sphere, they are illuminated with a time-varying magnetic field generated by a synthetic double-loop model of the Geophex GEM-3 sensor. The simulated sensor is placed at different points on the measurement grid at 25-cm increments. The full EMI problem is solved for each sensor position, and  $\mathbf{H}_1^{\text{sc}}$ ,  $\mathbf{A}_1^{\text{sc}}$ , and  $\psi_1^{\text{sc}}$  are calculated. The objects' center location is estimated using (2.7) and is depicted in Figures 2.12, 2.13, 2.16, and 2.17. These results again demonstrate that the algorithm can predict a buried object's center position with reasonable accuracy for both homogeneous and heterogeneous objects. Note that these results are presented only for a single frequency; similar trends have been observed for all other frequencies. Figures 2.13 and 2.17 show the buried object's center in the  $x$ - $y$  plane, while Figures 2.14 and 2.18 depict the estimated  $z_c$  from each of the observation points.

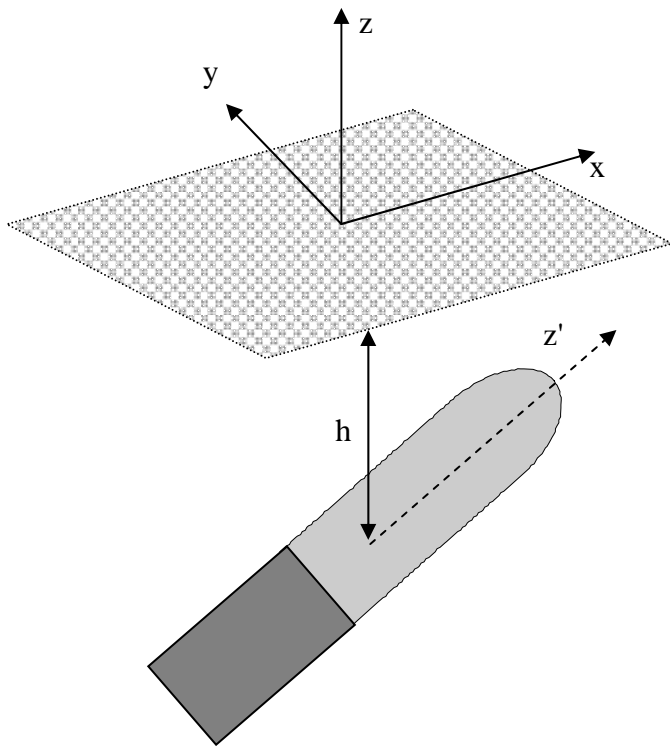


**Figure 2.15.** Problem geometry for a heterogeneous object.

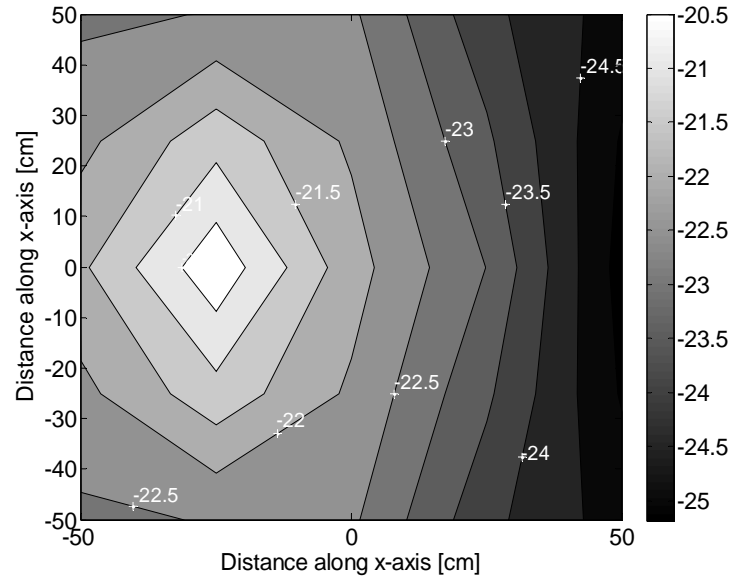


**Figure 2.16.** Estimated  $z_c$  for the heterogeneous object of Figure 2.15.

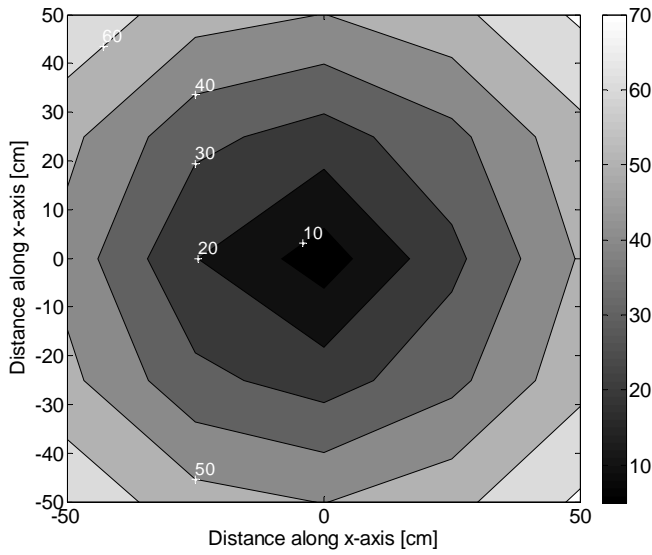


**Figure 2.17.** Estimated  $\sqrt{x_c^2 + y_c^2}$  for the heterogeneous object of Figure 2.15.

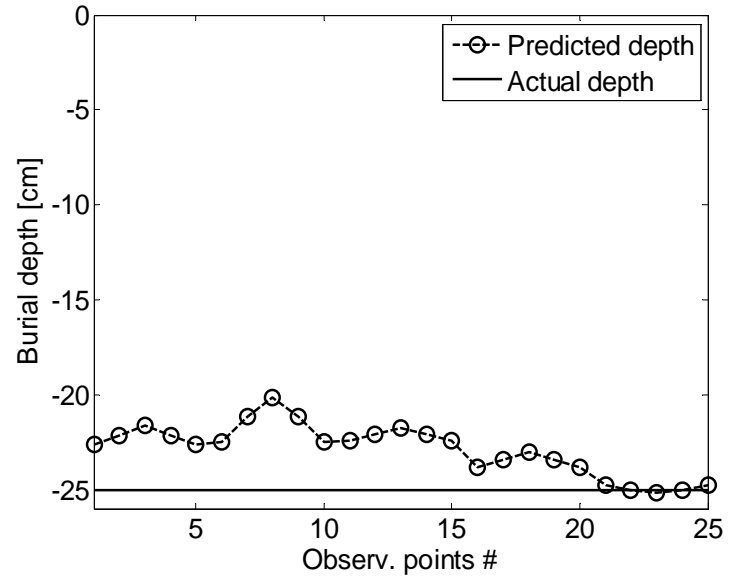


**Figure 2.18.** Estimated  $z_c$  for the bullet of Figure 2.15 vs. observation point.

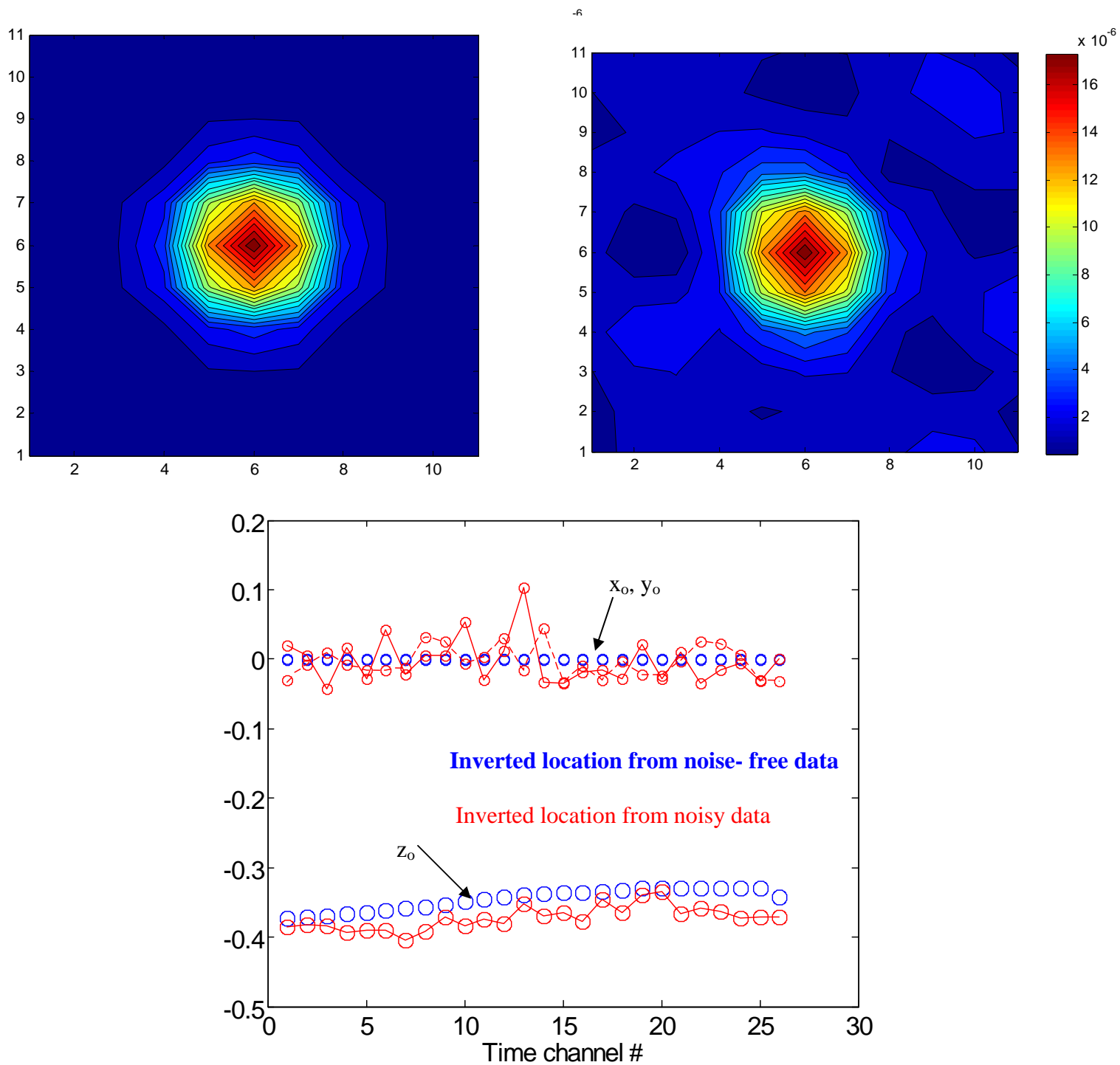


**Figure 2.19.** Scattered magnetic field from an 81-mm UXO modeled via the SEA using synthetic data a) without and b) with noise. c) Inverted location from noise-free and noisy data.

### 2.8.6. Noise-effect analysis for heterogeneous objects

To further illustrate the applicability of the HAP method in real field conditions, we investigate the performance of the technique for a case in which signals are contaminated with additive sensor noise. We generate synthetic scattered-field data using the (spheroidal) standardized excitation approach (SEA). The analysis is done for an 81-mm UXO for which the amplitudes of a reduced set of responding sources were determined and stored in a library. Using these sources we generated the object's EMI response on a  $11 \times 11$  measurement grid to the primary field of the (monostatic) EM-63 sensor. These responses are depicted on Figure 2.19, upper left; the target was placed at a depth of 35 cm and oriented horizontally. To replicate the conditions of a EM-63 survey we calculated only one component ( $H_z$ ) of the scattered magnetic field. The 2D NSMS layer was placed under the measurement grid and the amplitudes of the NSMS were determined, after which the magnetic field and scalar magnetic potential were determined for 26 time channels. The target position was estimated using the HAP technique. The inverted results are depicted on Figure 2.19. The results show that the HAP method reconstructs the position very well. We then added random Gaussian noise to the field reading at every position; the results appear in Figure 2.19 upper right. The object's position was inverted from the noisy data by applying the same numerical procedure. The inverted results are depicted on Figure 2.19 with red circles. We see that even with noisy data the method does a very good job of predicting the object's position, in particular its depth.

### 2.8.7. Estimating object location using measured monostatic and multistatic EMI data

#### 2.8.7.a. Frequency-domain EMI data

In this section we apply our approach to monostatic GEM-3 data. We first compare the predicted EMI magnetic field computed via the NSMS fictitious source layer to measured data. In these tests, the NSMS model is used to predict the scattered magnetic field components  $H_x$  and  $H_y$  using only monostatic measured magnetic field data. The tests are done for a steel sphere of radius  $a = 3.75$  cm.

The data were collected at two elevations:  $h_1 = 21$  cm and  $h_2 = 26$  cm using the new Geophex GEM-3D+ sensor (O'Neill *et al.*, 2004). Here  $h_1$  and  $h_2$  are measured from the sphere's center to the measurement surface. The GEM-3D+ sensor consists of two transmitter loops and three orthogonal receivers (Figure 2.20). The currents in the transmitter loops circulate in opposite directions and are scaled so that their respective primary fields cancel at their common center, where the receiving coils are located. In the numerical model, the transmitter loops are idealized as infinitely thin loop sources of radii  $a_1$  and  $a_2$ , with currents  $I_2 = -I_1 a_2/a_1$ . At each elevation, the EMI field is measured on an 81-point grid at 5-cm increments.

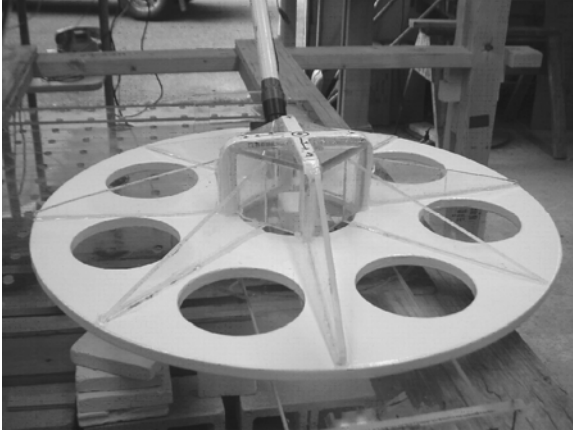


**Figure 2.20.** The GEM-3D+ sensor head showing the transverse receiver coils.

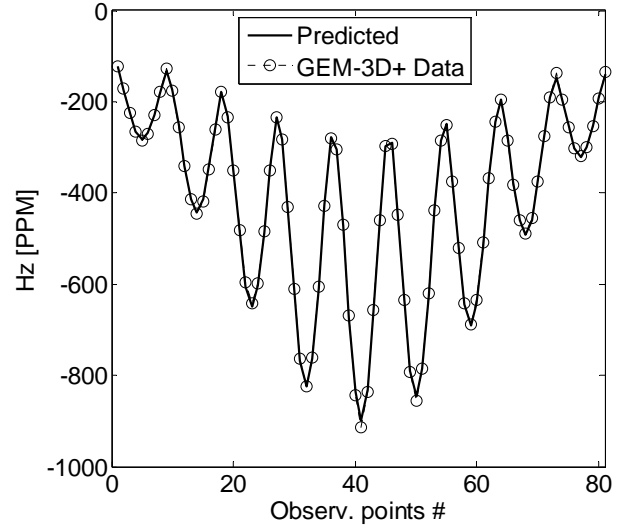


**Figure 2.21.** Comparisons between actual and modeled  $H_z$  data.

The scattered magnetic field is modeled as a superposition of the magnetic field produced by a set of normalized magnetic dipoles placed on a fictitious surface just below the actual measurement grid. The fictitious surface is divided into small patches (*cf.* Figure 2.2). At each patch the primary magnetic field is determined. The amplitudes of the responding magnetic dipoles on each subsurface are scaled by the primary magnetic field using (2.26). The amplitudes of the responding surface layer NSMS are then determined by matching the  $z$ -component of the modeled magnetic field to its measured counterpart at the grid points with a sensor elevation  $h_1$ . Once the amplitudes are found, the secondary field quantities  $\tilde{\mathbf{H}}_1^{\text{sc}}$ ,  $\tilde{\mathbf{A}}_1^{\text{sc}}$ , and  $\tilde{\psi}_1^{\text{sc}}$  can be found anywhere above the fictitious surface. Note that the auxiliary NSMS layer is placed between the object and the measurement plane. In this arrangement, the NSMS surface sources represents the magnetic fields radiated by all metallic objects distributed beneath the fictitious surface.

The NSMS sources were distributed on a  $5 \times 5$  grid at an elevation  $h = 10.5$  cm. The spacing between sources in this case was 10 cm. The NSMS modeled magnetic field is matched to the measured data at the elevation  $h_1 = 21$  cm. The results appear in Figure 2.21. The surface-distributed NSMS sources do a good job of predicting the EM signal at  $h_1$ . After determining the amplitudes of the NSMS we can compute the  $x$ - and  $y$ -components of the scattered monostatic magnetic field at  $9 \times 9$  grid points at the elevation  $h_2 = 26$  cm, where the GEM-3D+ data were collected. The results appear in Figure 2.22. The NSMS dipoles can be seen to predict  $H_x$  and  $H_y$  of the scattered magnetic field at elevation  $h_2$  using only the  $H_z$  of the scattered magnetic field data at  $h_1$ .

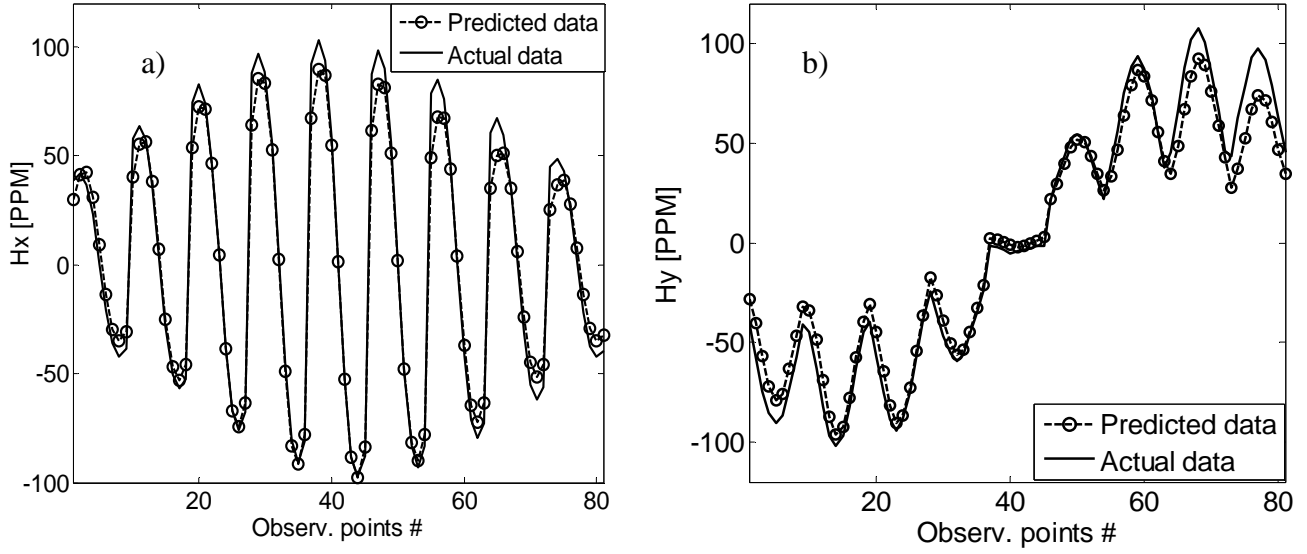
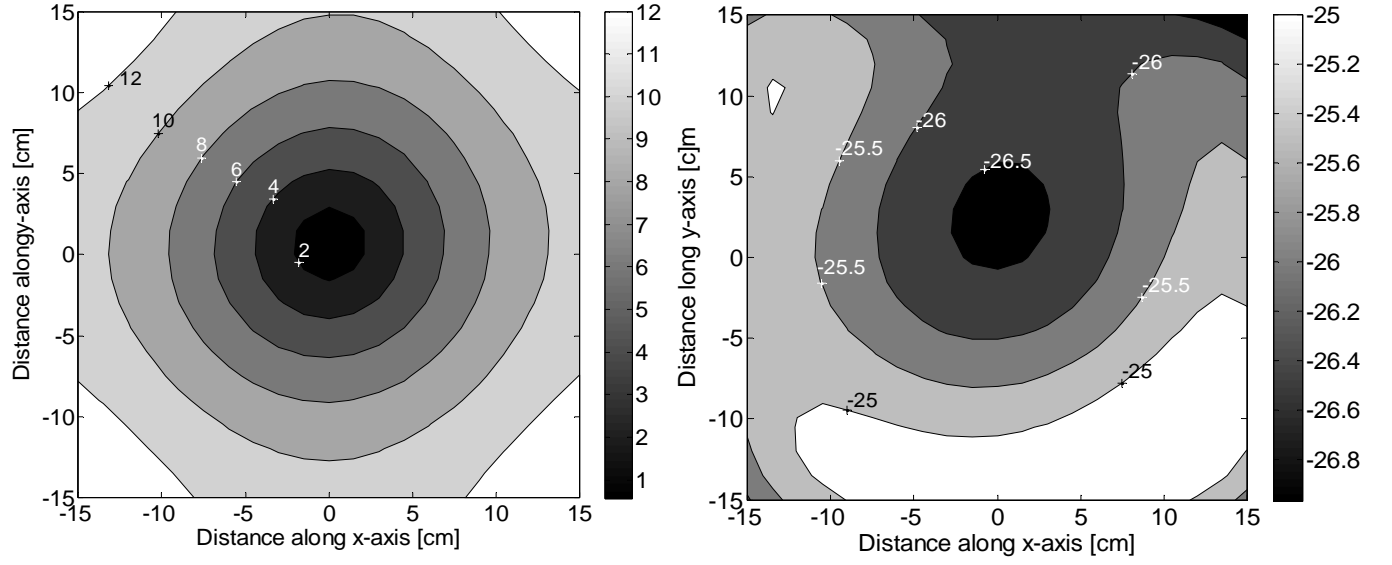


**Figure 2.22.** Comparisons between actual and predicted data for a sphere subject to GEM-3D+ excitation: (a)  $x$ -component, (b)  $y$ -component.

Similarly, using these amplitudes of the NSMS layer we estimate the vector and scalar potentials  $\tilde{\mathbf{A}}_1^{\text{sc}}$  and  $\tilde{\psi}_1^{\text{sc}}$  at the same  $9 \times 9$  grid at elevation  $h_2 = 26$  cm in order to determine the coordinates of the center of the sphere using (2.7). The predicted  $\sqrt{x_c^2 + y_c^2}$  and  $z_c$  are depicted in Figure 2.23. The results illustrate that the algorithm can predict the object's location from actual  $H_z$  data.

To demonstrate the superior performance of the HAP technique combined with the NSMS approach, we apply the algorithm to frequency-domain GEM-3D+ blind-test data. These were collected for eight targets, of which three were clutter and five were UXO: a BLU-26 bomblet, a Rockeye, an 81-mm projectile, a 60-mm mortar, and a 57-mm bullet. For all these items detailed data were collected under controlled conditions, which were used to determine the total NSMS  $Q(f)$  for each target. We then determined the locations and orientations of the objects using the HAP algorithm. The true and estimated locations and orientations of the targets are given in Table 2.3. The results show that inverted and true values of position and orientation are in general very close. After that we calculated the total NSMS for each of the eight objects and compared them to the total NSMS values stored in a library of six UXO items. In all cases the inverted NSMS closely matches its corresponding UXO items (see Figure 2.24), which means that the algorithm was able to identify all items with 100% accuracy.

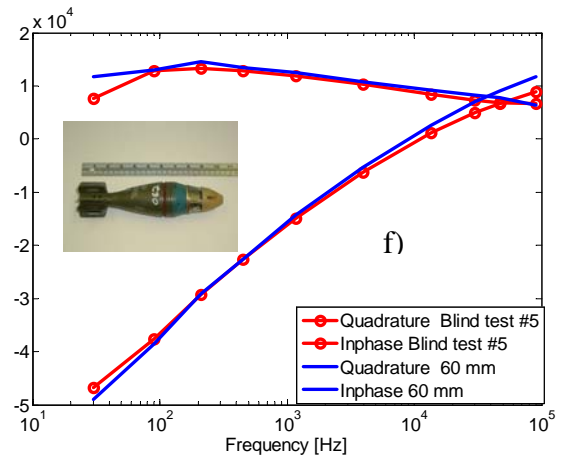
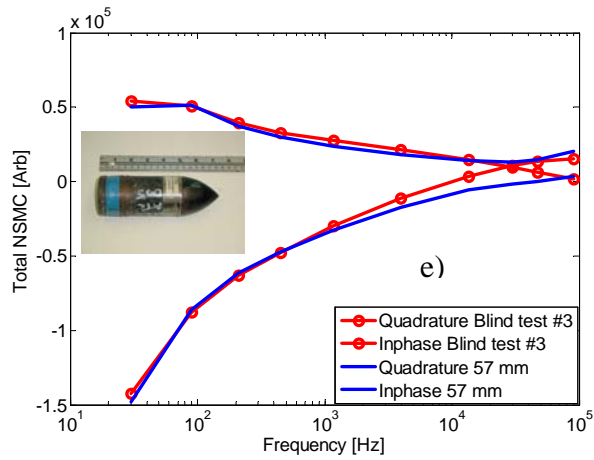
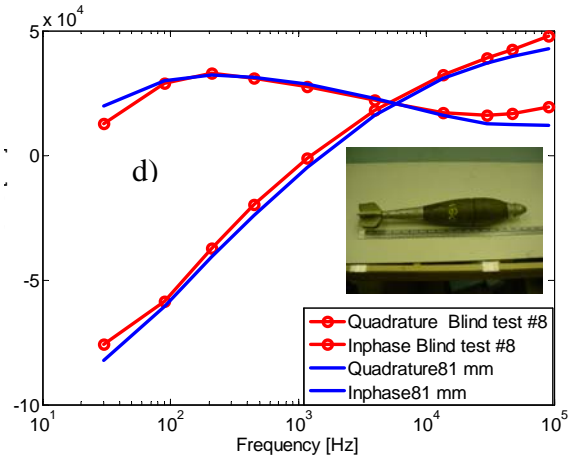
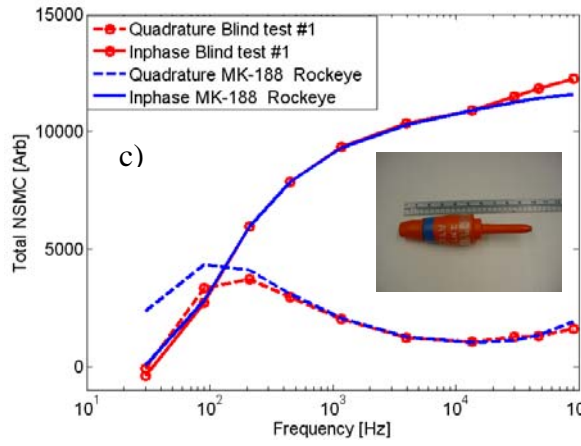
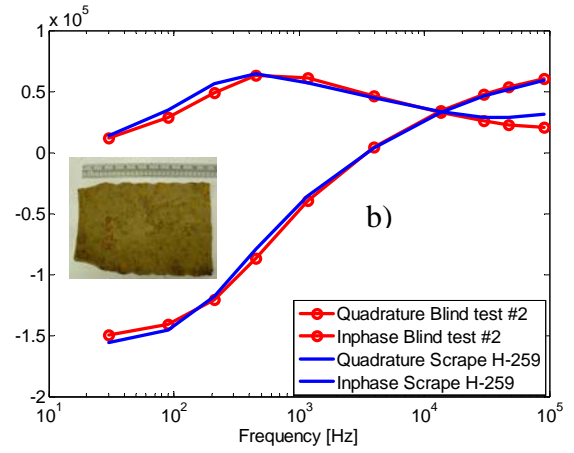
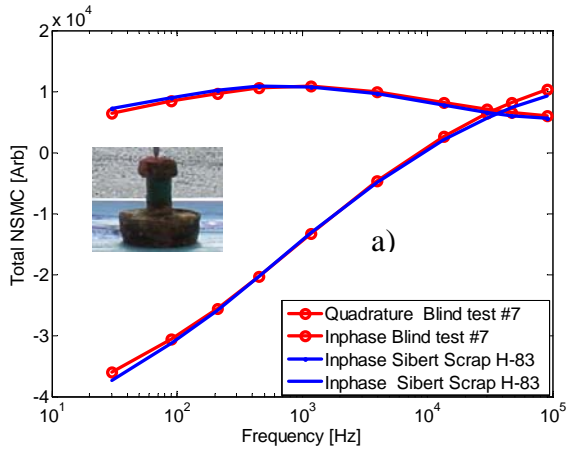




**Figure 2.23.** Estimated  $\sqrt{x_c^2 + y_c^2}$  (left) and  $z_c$  (right) for the steel sphere. The true  $z_c = 26$  cm.

**Table 2.3.** Estimated and actual positions and orientations for the GEM-3D+ blind-test data runs.

Blind test #	Estimated (Actual)				
	$\theta$ ( $^\circ$ )	$\phi$ ( $^\circ$ )	$x_0$ (cm)	$y_0$ (cm)	$z_0$ (cm)
1	93.60 ( 45)	90.0 ( 90)	3.0 ( 0)	0.01( 1.5)	-29.68(-28)
2	86.17 ( 90)	20.9 (135)	-5.5 ( -5)	5.03( 5)	-34.46(-31)
3	105.36 ( 0)	76.4 (arb)	-15.6 (-20)	-15.8 (-15)	-43.46(-42)
4	91.08 (arb)	2.25(arb)	18.2 ( 20)	-0.5 ( 0)	-25.19(-22)
5	81.05 (135)	10.11(135)	20.2 ( 15)	-0.7 ( 5)	-26.22(-26)
6	86.34 (180)	67.05(arb)	5.3 ( 10)	-12.64(-20)	-20.25(-18)
7	65.56 ( 90)	16.63( 45)	12.9 ( 18)	4.13( 12)	-25.81(-20)
8	66.06 ( 90)	14.01( 90)	3.35 ( 5)	15.45( 10)	-43.10(-40)



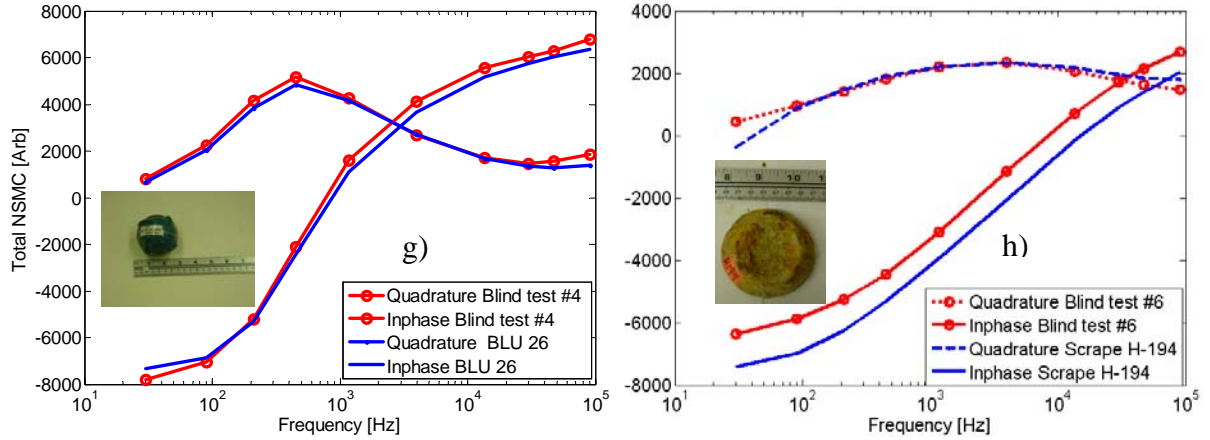


**Figure 2.24.** Comparison between GEM-3D+ blind tests inversions and library NSMS.

#### 2.8.7.b. Time-domain EMI-63 data

The algorithm was also applied to data from the time domain EM-63 sensor made by Geonics LTD (McNeill and Bosnar, 1996). The EM-63 sensor consists of a  $1\text{ m} \times 1\text{ m}$  square transmitter loop and two receiver loops: (1) the main receiver loop is  $0.5\text{ m} \times 0.5\text{ m}$  in size with a center that coincides with the transmitter coil's center, and (2) the same size receiver loop that is placed 60 cm above the main receiver coil. These receivers measure the complete transient response from  $180\text{ }\mu\text{s}$  to 25 ms. The time-domain measurements were conducted at the UXO test-stand at the U.S. Army Corps of Engineers, Engineer Research and Development Center (ERDC) Laboratory, Vicksburg, MS. The measurement platform, which is made with nonmetallic fiberglass materials, has a usable measurement area of  $3 \times 4\text{ m}$  in extent. The sensor is mounted on a robotic arm that can be moved and controlled around the measurement area using software running on a remote personal computer. Automated remote controls are used to position an ordnance item at an accurate depth (within 1 cm) below the measurement area. The sensor can be positioned with an accuracy of approximately 1 mm. All data presented here were collected by Sky Research personnel.

The time domain data were collected at a  $h = 60\text{ cm}$  elevation at 441 points for a horizontally oriented 81-mm UXO. Again, the scattered magnetic field is modeled as a superposition of the magnetic field produced by a set of surface magnetic dipoles placed on a fictitious surface just 20 cm below the real surface. After determining the amplitudes of the NSMS on this surface, the magnetic field and the potentials are estimated, and the object's location is approximated using the method presented here. The estimated  $z_c$  location of the

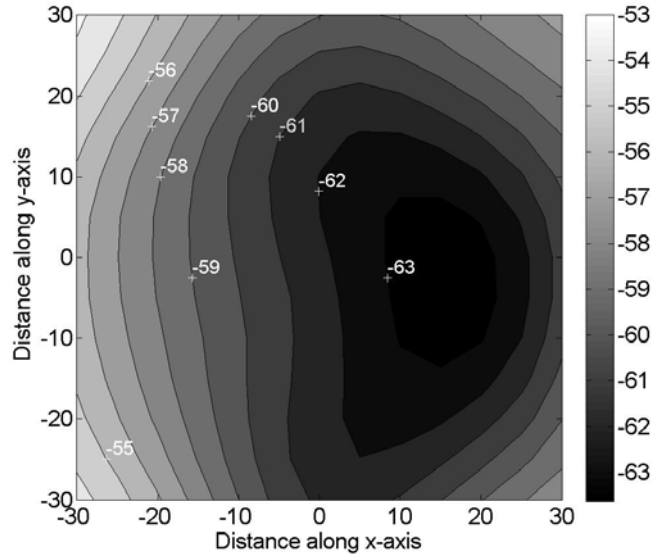


**Figure 2.25.** Estimated  $z_c$  for the 81-mm UXO.

The true  $z_c = 60\text{ cm}$ .

object's center is depicted on Figure 2.25, and the good agreement indicates that the proposed approach is applicable for TD EMI data as well. These results were obtained using only the first time channel, but our studies indicate that other time channels produce similar results. Multiple data channels can simultaneously be used to obtain more reliable estimates of the object's position.

### 2.8.7.c. MPV-TD data blind-test analysis

We also tested the NSMS technique and the HAP approach using TD MPV sensor data. The MPV TD sensor consists of two transmitter loops with 37.5-cm radii and five triaxial receiver loops/cubes (see Figure 26). The receivers are located as follows: Cube #0 upper center; Cube #1 lower center; Cube #2 left of center ( $x = -39.6$  cm); Cube #3 forward of center ( $y = 39.6$  cm); and Cube #4 right of center ( $x = 39.6$  cm). These receivers accurately measure the complete transient response over a wide dynamic range of time going from 100  $\mu$ s to 25 ms. The measurements were conducted by G&G personnel at the UXO test stand of the USACE-ERDC Laboratory in Vicksburg, MS. The measurement platform, which is made of nonmetallic fiberglass materials, has a usable measurement area of  $3 \times 4$  m in extent. The sensor is mounted on a robotic arm that can be moved and controlled around the measurement area using software running on a personal computer. Automated remote controls are used to position ordnance items at an accurate depth (to within 1 cm) below the measurement area. The sensor can be positioned with an accuracy of approximately 1 mm. All data presented here were collected by personnel from G&G Sciences Inc. The data were collected on an 89 point grid for objects at different orientations and depths. The response of each object was represented with only five NSMS belts.

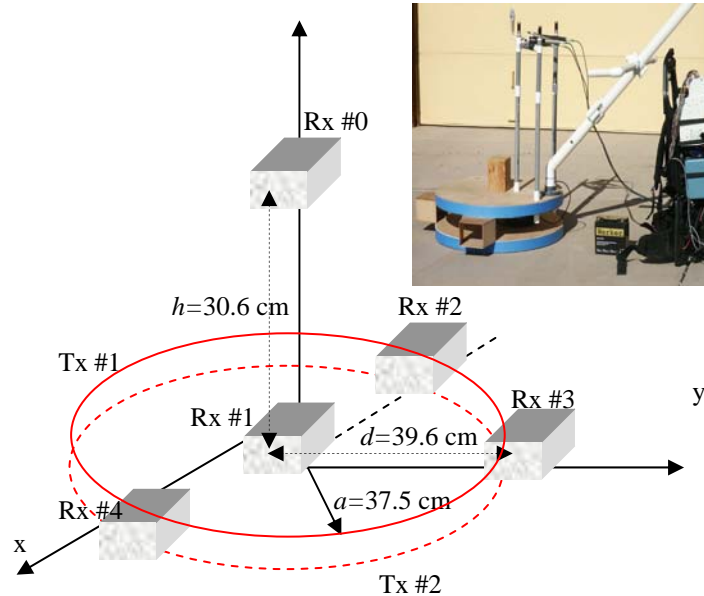


**Figure 2.26.** Actual and schematic diagram of the MPV-TD sensor.

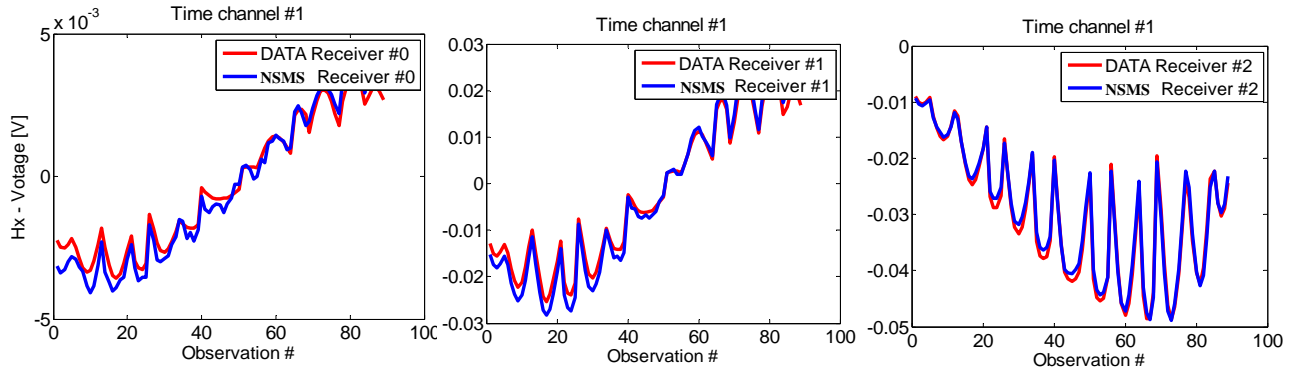


**Figure 2.27.** Predicted and actual TD MPV data for a 60-mm UXO.

We first test the accuracy of the NSMS technique against well controlled test-stand data for a 60-mm UXO. Figure 2.27 compares predicted and actual data at a fixed time gate for the  $x$  components of the scattered magnetic fields as measured by three receivers (Cubes #0, 1, and 2; see Figure 2.26). The results clearly show that the NSMS can predict the EMI response of the 60-mm UXO.

Once the accuracy of the NSMS has been established, we proceed to apply the technique to TD-MPV blind test data. These blind test data were collected for five unidentified targets at CRREL facilities by CRREL personnel using the MPV. The test objects considered were five UXO (a BLU-26 bomblet, 105-mm and 81-mm projectiles, a 60-mm mortar, and a 57-mm bullet) for which very detailed data were collected under controlled conditions at the USACE-ERDC test site in Vicksburg. Using those data sets we determined the total NSMS  $Q(t)$  values for the known UXO. Target EMI responses were measured over 34 grid points at two elevations, but in this study only data at one elevation were used. First, the locations and orientations of the objects were determined using the new algorithm. The true locations and orientations of the five targets are given in Table 2.3; the inverted estimates are summarized in Table 2.4.

The comparison between inverted and true values for position and orientation shows that the predicted values in general are very close to the true values. Sometimes the azimuthal angle  $\phi$  is seen to be flipped; this is mainly due to BOR symmetry and does not constitute an error.

Once the targets' locations and orientations were determined we computed the total NSMS for the five objects and compared them to the five total NSMS values stored in the library of UXO items. Comparisons between the total NSMC Target #1 and those of the library UXO are depicted in Figure 2.28. Note that the NSMS library was created using TD MPV data collected at the UXO test-stand site when the objects were oriented horizontally (dip =  $90^\circ$ ) with respect to the measurement grid. The comparison shows that the total NSMS (a scalar discriminator) is directly related to the object's size and material properties: as the size of the object increases so does the total NSMS amplitude. In addition, the inverted total NSMS for Target #1 correctly identified the actual target. This demonstrates that the total NSMS is independent of the target's location and orientation and is characteristic of the object. In this test we used TD-MPV data collected at 17 points and one elevation.

**Table 2.4.** Ground truth for the MPV-TD blind-test data runs.

Target	ID	x0 (cm)	y0 (cm)	z0 (cm)	$\phi$ ( $^{\circ}$ )	dip ( $^{\circ}$ )
1	81-mm	-23.26	22.5	56.16	0	18.3
2	105-mm	-20.26	22.5	69.14	180	18.6
3	BLU-26	0.00	22.5	43.21	0	0.0
4	57-mm	5.22	22.5	51.45	180	306.6
5	60 -mm	0.00	22.5	54.50	0	0.0

**Table 2.5.** Inverted results for position and orientation for MPV-TD blind-test data.  
Numbers with an asterisk are arbitrary due to BOR considerations.

Target	ID	x0 (cm)	y0 (cm)	z0 (cm)	$\phi$ ( $^{\circ}$ )	dip ( $^{\circ}$ )
1	81-mm	-21.16	23.6	56.56	0	-2
2	105 mm	-5.98	23.7	67.57	170	-20.8
3	BLU-26	0.25	22.8	47.55	*0	*180.0
4	57-mm	0.75	22.6	58.19	0	320.4
5	60- mm	0.67	19.3	54.02	*3	0.0

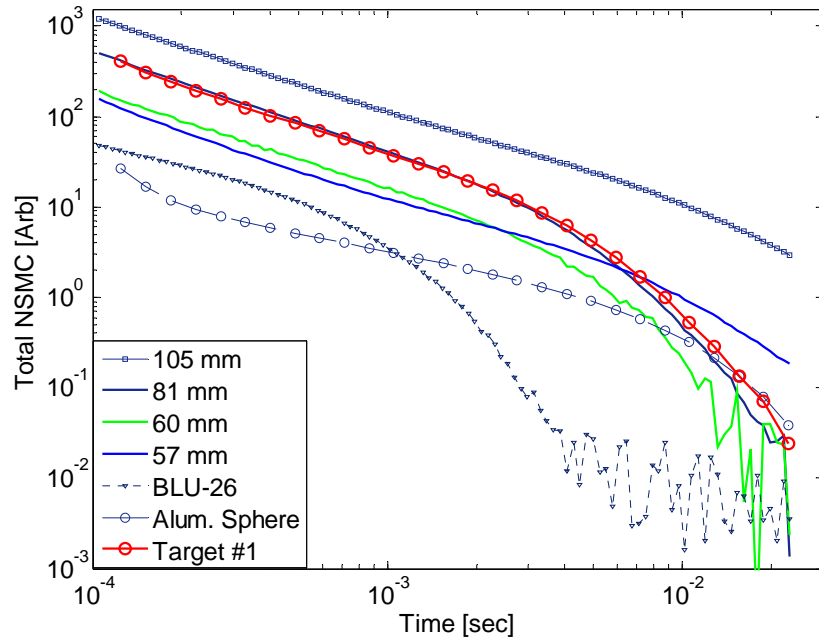


**Figure 2.28.** NSMS model comparison to library for Target #1.

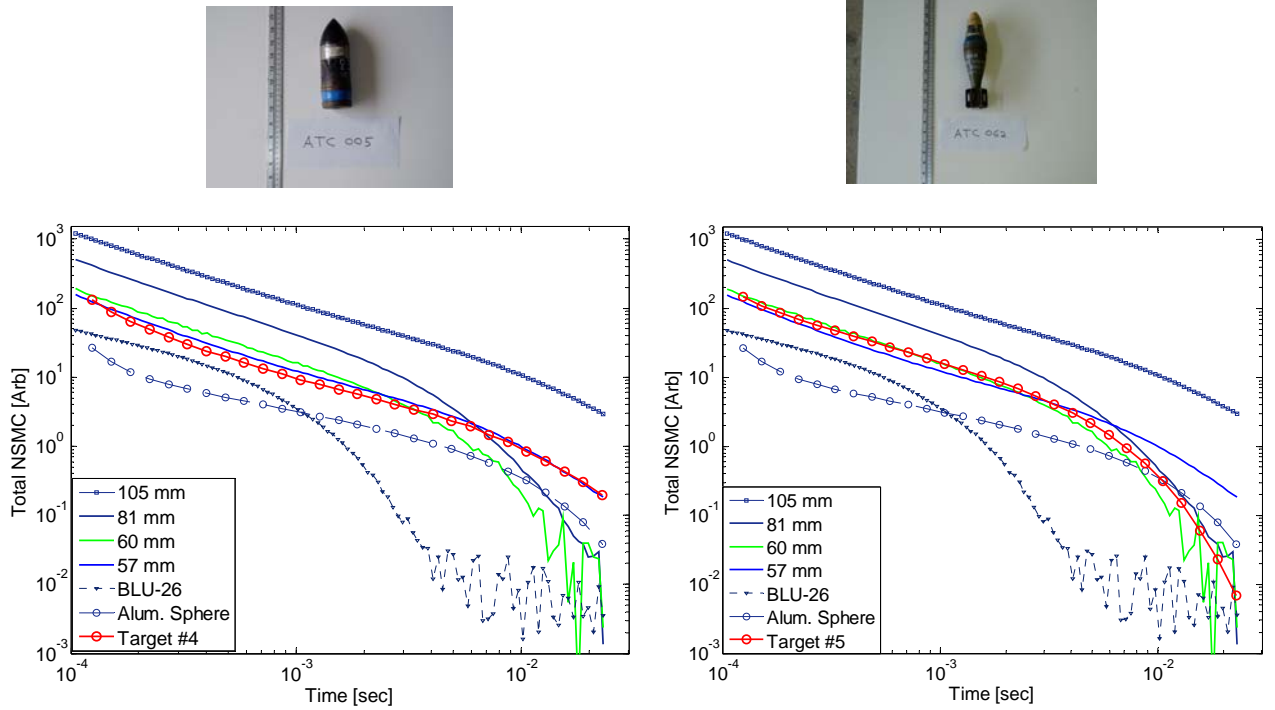


**Figure 2.29.** NSMS model comparison to library for Target #4 (left) and Target #5 (right).

The algorithm identified correctly all remaining targets. It is worth noticing, in the case of Targets #4 and #5, that the total NSMS was able to differentiate between the 57-mm and 60-mm UXO even though they have comparable geometrical sizes (Figure 2.29). The results show that at early times/high frequencies the total NSMS from both objects are similar, due to the small skin depth; however, at late times/low frequencies the skin depth becomes significant and the total NSMS of sizable objects is separable and depends on the object's material properties and metal content, demonstrating a good discrimination capability. To further illustrate how the object's EMI response affects the total NSMS, on Figure 2.30 we added the total NSMS of a non-permeable sphere. The non-permeable sphere has the same size as the BLU-26, which is made of permeable steel. The results show that at early times the NSMS amplitudes of the two spherical targets are similar; at late times, two objects of similar geometric size but different material properties have different total NSMS.

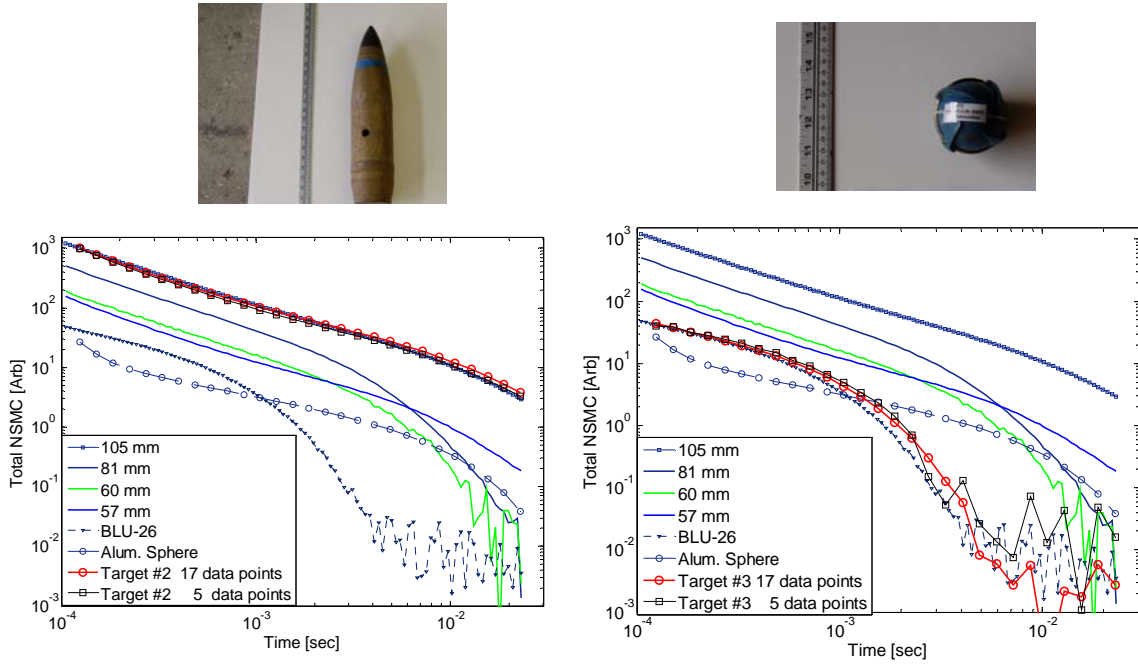


**Figure 2.30.** NSMS model comparison to library for Target #2 (left) and Target #3 (right).

Finally we investigate the data density requirement issue for UXO discrimination. UXO cleanup demands real/near-real time detection and discrimination systems to keep cleanup costs reasonably low by minimizing the time spent on each anomaly; moreover, such systems should discriminate between UXO and non-UXO items accurately and reliably. To address this problem here we study the TD-MPV data-density requirements for the NSMS model. Studies were done for Targets #2 and #3. The targets' total NSMS, as well as their positions and orientations, were inverted using either 17 or 5 measurement points. The inverted total NSMS values as functions of time for both cases are similar and they correctly coincide with the true object's total NSMS. Thus the results suggest that the amplitude of the total NSMC remains stable as the number and density of data points are reduced substantially for single-object discrimination.



#### 2.8.7.d. EMI Array

Finally the HAP method was adapted to the recently developed time domain EMI sensor array. The sensor consists of 25 transmit/receive pairs in a  $5 \times 5$  array of time-domain EMI sensors with a 35-cm diameter transmitter loop and a 25-cm receiver loop. The sensor transmits signal at a time in sequential order for 1 to 25, and for each transmitter all receivers receive. The receivers measure the complete transient response over a wide dynamic range of time going approximately from 100  $\mu$ s to 25 ms. The sensor provides 625 spatial data with unprecedented position accuracy. The data were collected by NRL personnel at Blossom Point. The actual and schematic diagram of the NRL EMI sensor are shown on Figures 2.31 and 2.32 respectively. The measured data distribution for the Camp Sibert 4.2-inch mortar are illustrated on Figures 2.33 and 2.34. On these figures each subplot corresponds to a fixed transmitter in subsequent order from 1 to 25. The HAP method was applied to the Camp Sibert 4.2-inch UXO TD EMI array data. The target was placed under the sensor at  $x_0 = y_0 = 0$ ,  $z_0 = -60$  cm. The TD data were for each transmitter and 123 time gates. The object's position was inverted for each time channel and transmitter using the HAP technique. Figure 2.35 shows inverted location versus transmitter number for each time channel. The results demonstrate the superior performance of the HAP method for predicting an object's position.



**Figure 2.31.** EMI TD array sensor in operation.

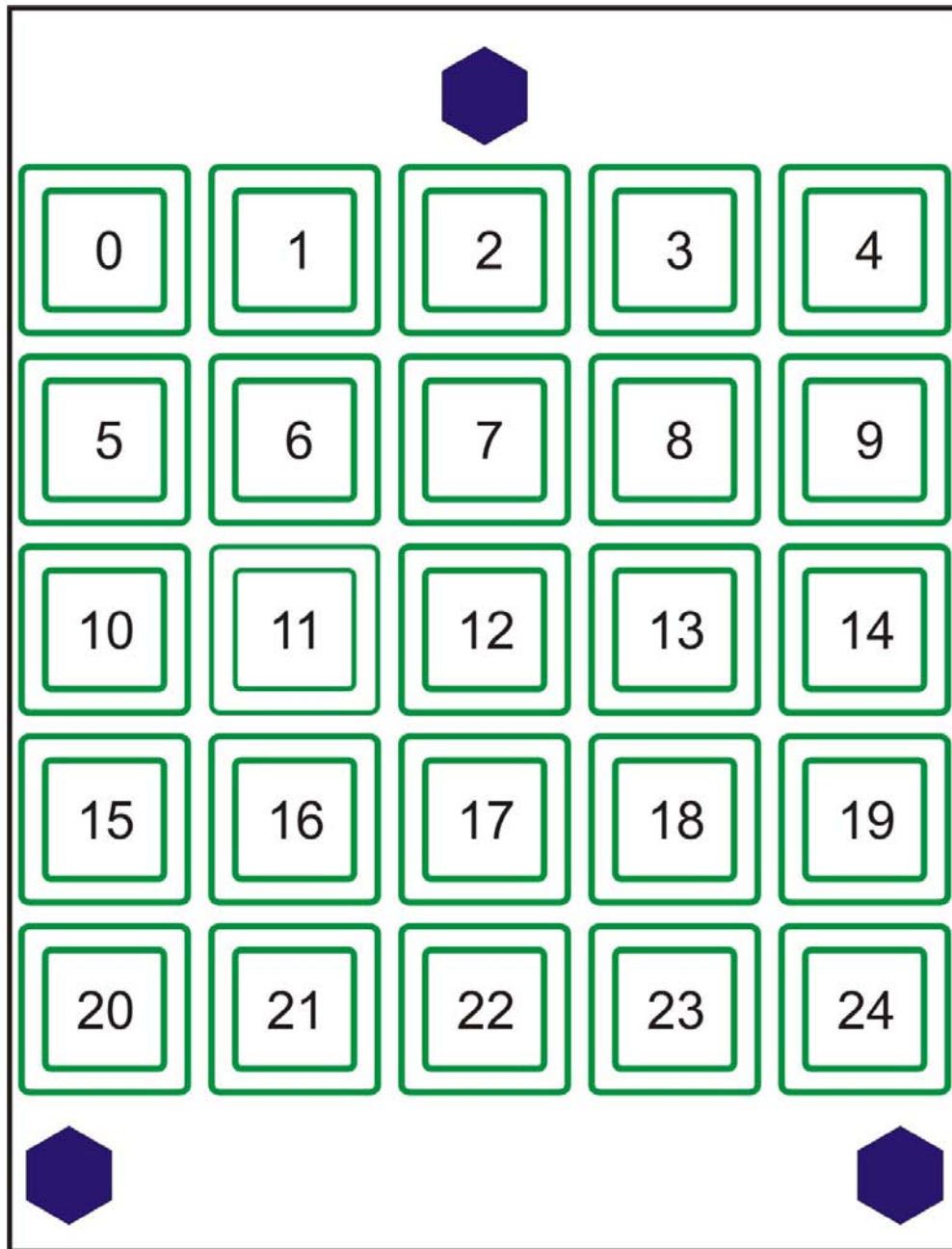


**Figure 2.32.** Schematic diagram of the EMI TD array sensor.

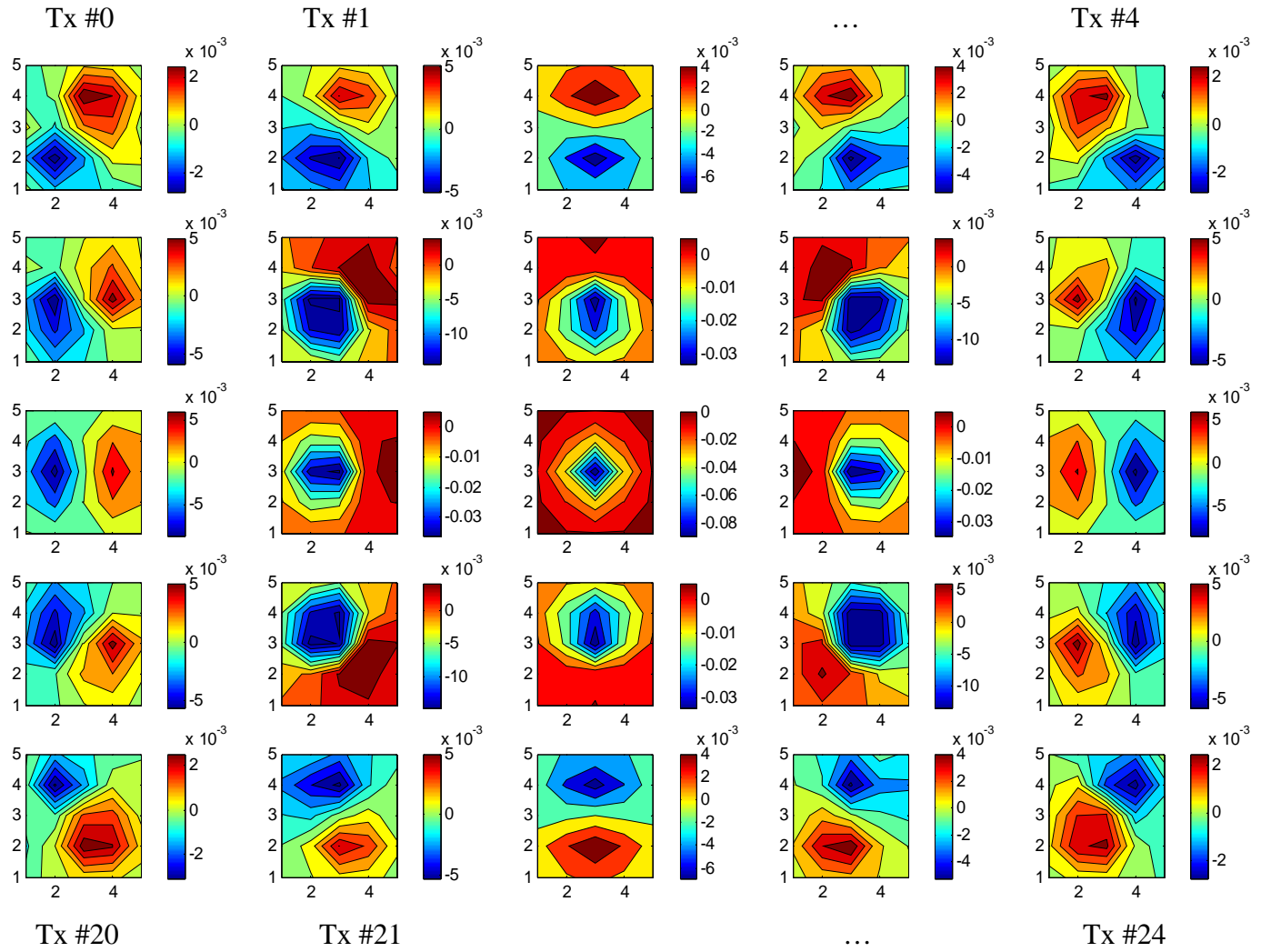


**Figure 2.33.** Measured EM field distribution on  $5 \times 5$  array receivers for time channel #1 for different (from 0 to 24) transmission; each subplot corresponds to a fixed trasmitter.

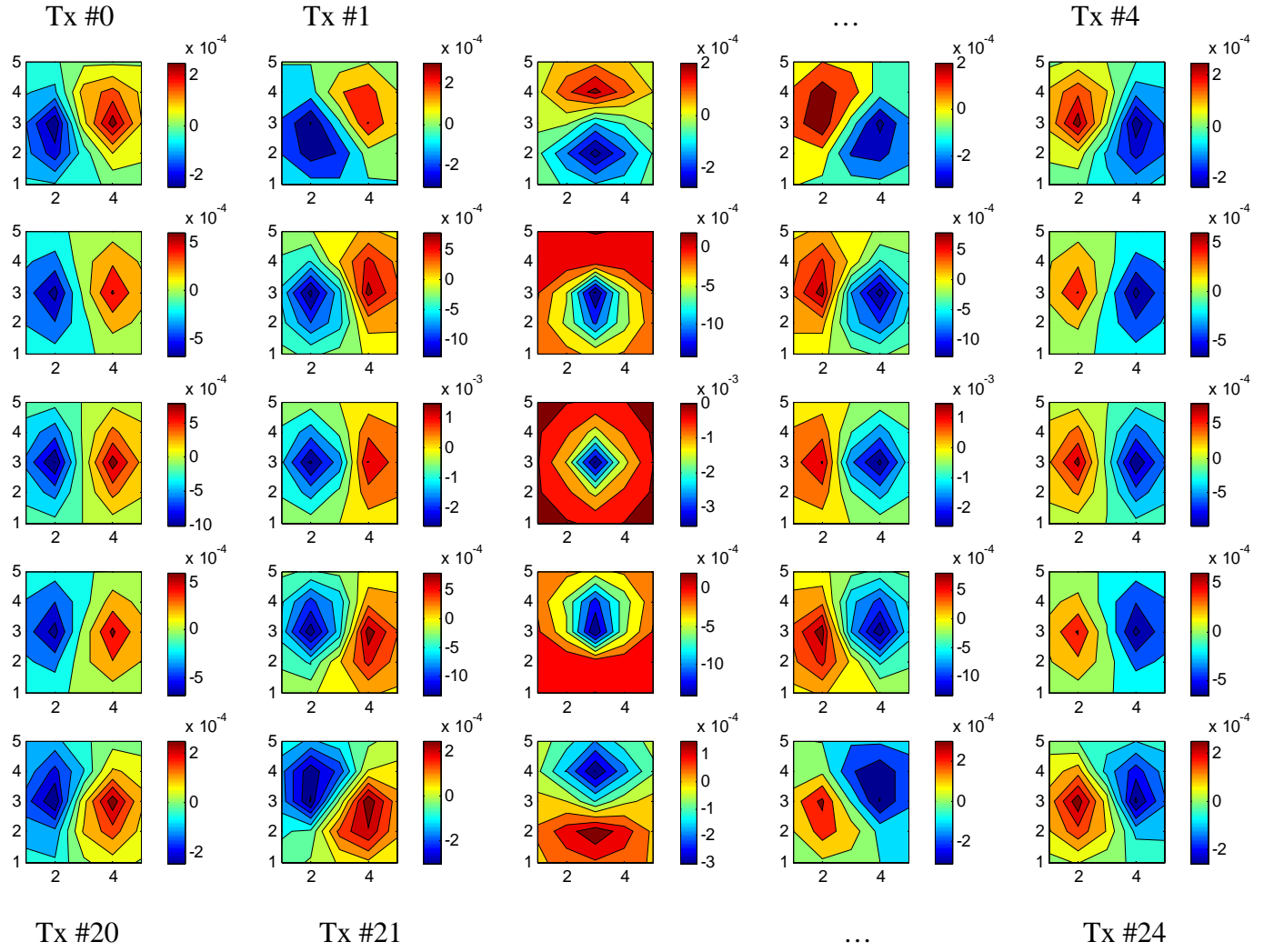


**Figure 2.34.** Measured EM field distribution on  $5 \times 5$  array receivers for time channel #40 for different (from 0 to 24 transmission); each subplot corresponds to a fixed transmitter.

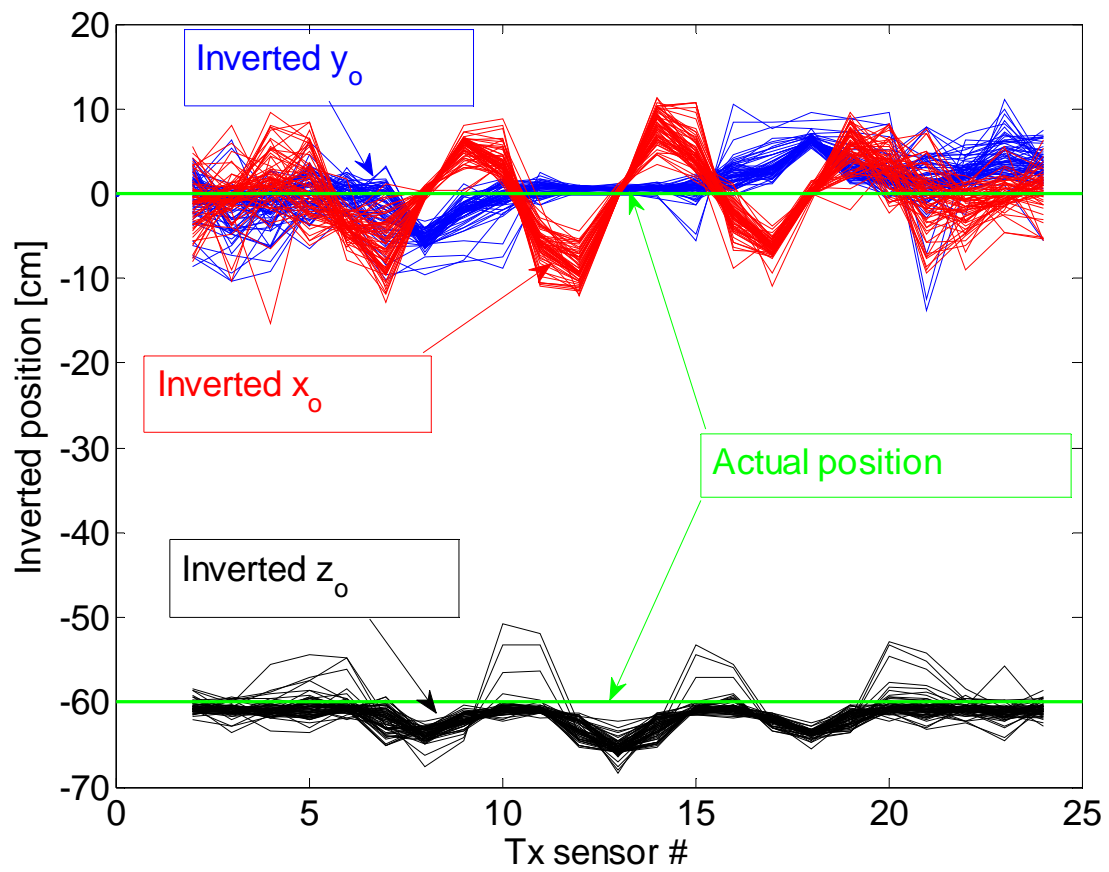


**Figure 2.35.** Inverted position for Camp Sibert 4.2-inch UXO vs. transmission number at different time channels.

## 2.9. Conclusion

A new physics-based analytic expression was developed for estimating a buried object's location, orientation, and magnetic polarizability without solving the traditional ill-posed inverse problem. The approach uses only three global quantities: the magnetic field  $\mathbf{H}$ , the vector potential  $\mathbf{A}$ , and the scalar potential  $\psi$ . The algorithm was tested using both time- and frequency-domain synthetic data as well as actual EMI data for dipoles, spheres and UXO, with and without added noise. The approach is valid for both land-based and underwater UXO scenarios. The 2D normalized surface magnetic source (NSMS) model has been developed to find an estimate of the scattered magnetic field and vector and scalar potentials from magnetic field data in the case of monostatic data. The method is a generalized surface dipole model approach for approximating EMI responses from highly conducting and permeable metallic objects. The procedure of determining the NSMS amplitudes distributed on a fictitious surface just beneath the measurement grid points is realized in a collocation based algorithm from monostatic as well as multistatic data.

Blind-test analyses were carried out for the MPV-TD and GEM-3D+ sensors using the normalized total surface magnetic source model in order to classify between UXO and non-UXO items. In these tests the NSMC model was combined with a physics-based approach for estimating buried objects' positions and orientations. During the blind-test UXO discrimination study we first estimated object positions and orientations via the HAP technique. Then we determined the amplitudes of the total NSMS from data for each unknown target, and finally the inverted total NSMC time/frequency dependent curves were used as discriminators by comparing them with the total NSMS of known UXO types from a pre-computed library. In all cases reported here the method was able to identify with reasonable accuracy the targets' positions and orientations, and at the end the NSMS was able to find the correct UXO among the possible ordnance and clutter items.

The HAP methods were extended for the NRL EMI array TD sensor as well. The results reported here clearly demonstrate the superior performance of the HAP technique for estimating location and orientation of single or aggregate buried targets when using actual EMI data from the NRL TD EMI array, MPV-TD, GEM-3D, and EM63 instruments. Moreover, the method is robust with respect to noise.



## Chapter 3

# Pole-series and pseudospectral approaches for estimating a buried object's depth

### 3.1. Introduction

In this chapter we consider the pole-series-expansion (PSE) and pseudospectral approaches to estimate the locations and orientations of buried objects. The PSE uses measured scattered electromagnetic (EM) field information at a given set of points to provide a very fast approximation for estimating the scattered EM field back to its origin at any spatial resolution. The method requires a bi-static scattered-field distribution on the spatial grid. Since most if not all sensors output mono-static scattered fields, here we combine the pole-series approach with the normalized surface magnetic source (NSMS) method to predict buried objects' locations and orientations: initially the NSMS is used to generate bi-static EMI data from measured mono-static data, and then the pole-series expansion is employed to localize scattered field singularities (SFS), *i.e.*, to find the objects.

Another technique considered here for locating buried objects is the pseudospectral finite-difference (PSFD) method, which is derived from spatial finite-difference (FD) approximations. In the magnetoquasistatic regime, this technique is based on a volumetric sampling of the magnetic field within and around the region of interest. In the standard FD technique, the spatial sampling is set by the user at a sub-spatial-wavelength resolution in order to sample properly the highest *spatial frequencies* thought to be important in the physics of the problem. This requirement on the space discretization has allowed the successful application of FD methods to solve Laplace's equation for a wide range of electromagnetic problems using second-order-accurate central differences on a staggered, uncollocated Cartesian lattice. To determine the location of the SFS in the EMI frequency regime it is necessary to solve simultaneously the curl-free and divergence-free Maxwell equations for the scattered magnetic field, which requires the use of different staggered, uncollocated Cartesian space lattices. This Yee-type space stepping is the source of numerical dispersion errors. To minimize the dispersion error in the computation of spatial derivatives we employ the pseudospectral FD method along the orthogonal  $x$ - and  $y$ -directions. The pseudospectral time-domain (PSTD) method calculates spatial derivatives using the differentiation theorem for Fourier transforms; this process converges with infinite-order accuracy for grid-sampling densities of two or more points per spatial wavelength. Our procedure models magnetic-field derivatives along the  $x$ - and  $y$ -directions with the PSTD method while keeping second-order central differences on a staggered, uncollocated Cartesian lattice along the  $z$ -axis; this allows the refocusing of the scattered magnetic field backward in space.

### 3.2. The pole-series-expansion approach in EMI

This method for estimating the depth of a buried object requires an essentially continuous representation of the object's response over a specific spatial range above the measurement

surface. Measuring the scattered EM field with sufficient resolution can be very expensive and time-consuming, especially when performing real-field UXO detection and discrimination. However, this problem can be overcome by employing the NSMS technique.

The spatial distribution of a linear system's EMI response may be optimally represented by Cauchy's method. Consider the rational expansion

$$F(s) = \frac{N(s)}{D(s)} + \text{Error}(s) = \frac{\sum_{i=0}^n N_i s^i}{\sum_{i=0}^d D_i s^i} + \text{Error}(s), \quad (3.1)$$

where  $F$  is the response of the system and  $s$  the coordinate. The error in this approximation depends on the maximum orders  $n$  and  $d$  of the power series expansions in the numerator  $N$  and denominator  $D$  as well as on the method used to determine the coefficients  $N_i$  and  $D_i$ . A simple technique to compute these parameters is to multiply (3.1) by  $D$  and evaluate it at a set of  $m$  depth points  $s_k$ :

$$F(s_k) \sum_{i=0}^d D_i s_k^i - \sum_{i=0}^n N_i s_k^i = \text{Error}(s_k) \sum_{i=0}^d D_i s_k^i = E_k, \quad k = 1, \dots, m, \quad (3.2)$$

where  $E$  is a vector of unknown errors. When  $F$  is known at  $m \geq n + d + 1$  points  $s_k$ , (3.2) is a linear system of  $m$  equations. One then can evaluate the parameters  $D_i$  and  $N_i$  in such a way that the square norm of the error vector is minimized. Before this is done, one should note that not all parameters are independent because the numerator and denominator in (3.1) may be scaled by an arbitrary factor. For this reason, one of the parameters may be set equal to 1. It is reasonable to set  $D_d = 1$ . One then obtains

$$F(s_k) \sum_{i=0}^{d-1} D_i s_k^i - \sum_{i=0}^n N_i s_k^i = -F(s_k) s_k^d + E_k = R_k + E_k, \quad k = 1, \dots, m, \quad (3.3)$$

where  $R$  is a known right-hand-side vector. Note that (3.2) can be solved in such a way that the error vector  $E$  is zero when  $m = m_0 = n + d + 1$ , because one then obtains a square matrix system. This does not imply that  $\text{Error}(s)$  becomes zero as well. Especially when the sample values  $F(s_k)$  are only approximately known—which is always the case in practice—it is more reasonable to work with an overdetermined system of equations in which  $m > m_0$ . Reasonable overdetermination should implicitly provide a “noise” minimization. The most difficult problem is to determine the required maximum orders  $n$  and  $d$  of the power series of the numerator and denominator. Both depend very much on the size of the space of interest, the desired accuracy, and the complexity of the system. Since the scattered field has  $1/R^3$  singularities, it is reasonable to limit the maximum orders  $n$  and  $d$  by a value typically not higher than 6 and to subdivide the spatial interval into two or more additional parts when the PSE approximation is not accurate enough. The algorithmic block scheme of the PSE procedure used for predicting object depths is presented on 0. The method is adaptive and starts with small orders—*i.e.*,  $n$  and  $d$  values—and with a small number of test points according to an overdetermination factor specified by the user. It then increases the order by 1 and compares the resulting PSE approximations. When the differences between the two approximations are below a user-defined error bound over the entire burial depth range and when all  $s$  parameters are within the range  $[0,1]$ , the PSE approximation is



good enough and the procedure stops. Otherwise, the algorithm inserts new test points within the depth range as follows: if an  $s$  parameter is out of the range, it inserts a new test point at the depth where the biggest distance from the range  $[0,1]$  is encountered. Otherwise, it searches for the maximum difference between the current and previous PSE approximation and sets the new test point at the corresponding depth.

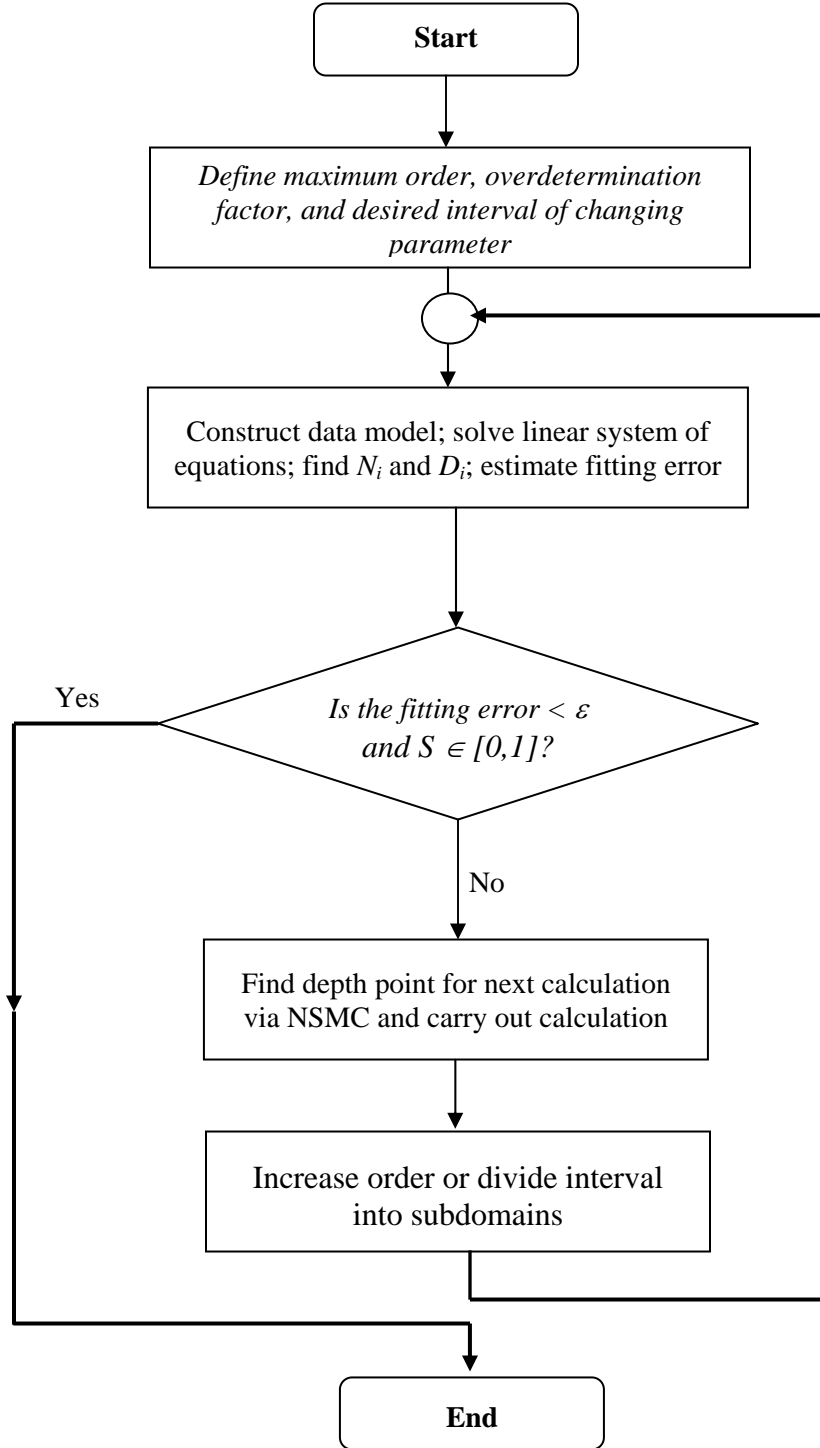


**Figure 3.1.** Schematic diagram of the PSE algorithm.

### 3.3. Pseudospectral FD scheme in EMI

The objective of this section is to outline the basic theory of the pseudospectral finite-difference (PSFD) method to invert for the location of a buried object via a finite-difference (FD) backward scheme. The first step of the proposed technique is to obtain measured EMI data at a plane with  $z = h$ ,  $x \in [-a, a]$ ,  $y \in [-b, b]$ . Then the entire volume is divided into subvolumes/cells characterized by the triple index  $(I, j, k)$  with  $I = 1, \dots, N_x$ ,  $j = 1, \dots, N_y$ ,  $k = 1, \dots, N_z$ . The PSFD technique is combined with the NSMS. First the NSMS amplitudes are determined from the measured data at the plane  $z_{N_z} = h$ ,  $x_i = -a + dx(I - 1)$ ,  $y_j = -b + dy(j - 1)$  (where  $dx$ ,  $dy$ , and  $dz$  give the size of the  $(I, j, k)$  cell) by solving a linear system of equations. At the next step a scalar magnetic field potential  $\psi$  is generated via SMS on the plane  $z_{N_z} = h + dz/2$ ,  $x_i + dx/2$ ,  $y_j + dy/2$  ( $I = 1, \dots, N_x$ ,  $j = 1, \dots, N_y$ ). We can then use the scalar magnetic potential  $\psi$  at  $z_{N_z} = h + dz/2$ ,  $x_i + dx/2$ ,  $y_j + dy/2$  and the magnetic field  $H_z$  at  $z_{N_z} = h$ ,  $x_i + dx/2$ ,  $y_j + dy/2$  to recover both the magnetic field and the scalar potential by solving  $\mathbf{H} = -\nabla \psi$  and  $\nabla \cdot \mathbf{H} = 0$  at each  $(I, j, k)$  cell.

To illustrate the technique, let us consider an object placed in free space and illuminated with a primary magnetic field. The primary magnetic field penetrates the object and induces eddy currents within it; these eddy currents in turn produce a measurable secondary magnetic field outside the object. Our goal is to use the magnetic fields at two surfaces ( $x$ - $y$ ,  $z = h$  and  $x$ - $y$ ,  $z = h + dz/2$ ) to predict the scattered magnetic field below the surface  $x$ - $y$ ,  $z = h$ . To do that let us combine the  $x$  and  $y$  components of the curl-free Maxwell equation for the scattered magnetic field  $\mathbf{H}^{\text{sc}}$  with the divergence-free equation:

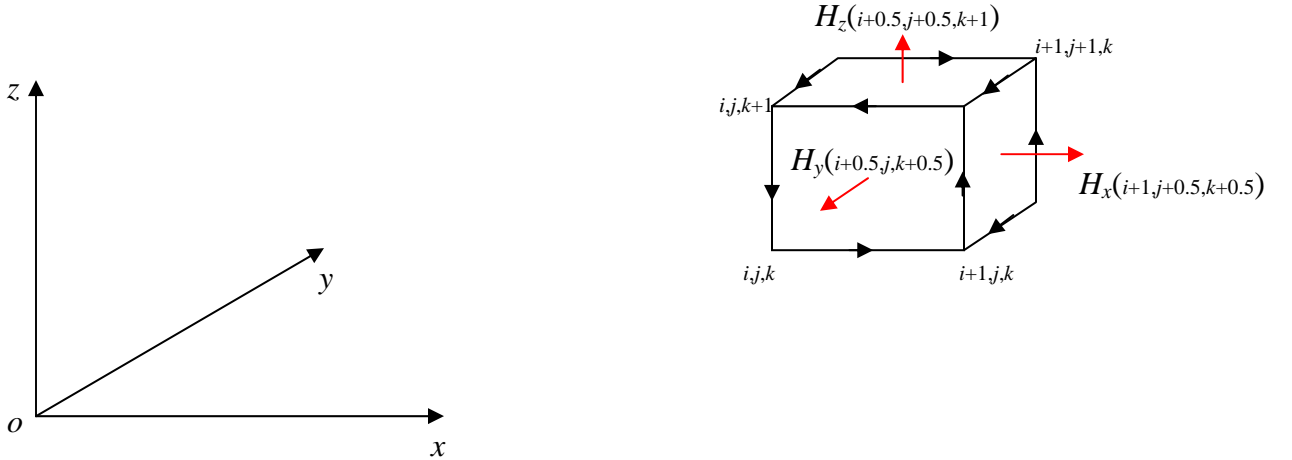


Figure 3.2. Yee FD scheme for the PSFD approach.

$$\begin{cases} \frac{\partial H_x^{sc}}{\partial z} = \frac{\partial H_z^{sc}}{\partial x} \\ \frac{\partial H_y^{sc}}{\partial z} = \frac{\partial H_z^{sc}}{\partial y} \\ \frac{\partial H_z^{sc}}{\partial z} = -\left( \frac{\partial H_x^{sc}}{\partial x} + \frac{\partial H_y^{sc}}{\partial y} \right) \end{cases} \quad (3.4)$$

By using the standard FD scheme (3.4), the curl- and divergence-free Maxwell equations for  $\mathbf{H}^{sc}$  in FD form can be written as

$$\frac{H_x^{sc}(i+0.5, j, k) - H_x^{sc}(i+0.5, j, k-1)}{\Delta z} = \frac{H_z^{sc}(i, j, k+0.5) - H_z^{sc}(i-1, j, k+0.5)}{\Delta x} \quad (a)$$

$$\frac{H_y^{sc}(i, j+0.5, k) - H_y^{sc}(i, j+0.5, k-1)}{\Delta z} = \frac{H_z^{sc}(i, j, k+0.5) - H_z^{sc}(i, j-1, k+0.5)}{\Delta y} \quad (b)$$

$$\begin{aligned} \frac{H_z^{sc}(i+0.5, j+0.5, k) - H_z^{sc}(i+0.5, j+0.5, k-1)}{\Delta z} = \\ -\left( \frac{H_x^{sc}(i, j+0.5, k+0.5) - H_x^{sc}(i-1, j+0.5, k+0.5)}{\Delta x} + \frac{H_y^{sc}(i+0.5, j, k+0.5) - H_y^{sc}(i+0.5, j-1, k+0.5)}{\Delta y} \right) \end{aligned} \quad (c)$$

(3.5)

where the subscripts  $i, j$ , and  $k$  are the Cartesian coordinate indices of the spatial sampling point  $(i \Delta x, j \Delta y, k \Delta z)$  in the three-dimensional (3-D) lattice. According to the standard FD scheme the curl-free equations (3.5)(a) and (3.5)(b) and the divergence-free equation (3.5)(c) require difference lattice points (see Figure 3.2: black and red arrows apply to the curl and divergence equations respectively). This complicates the applicability of the standard FD scheme to refocus the scattered magnetic field backwards to its origin. To overcome this difficulty and avoid the spatial derivatives on a staggered, un-located grid, we employ a pseudospectral FD (PSTD) technique for calculating the derivatives with respect to the  $x$ - and  $y$ -coordinates. The PSTD method utilizes discrete Fourier transforms to evaluate spatial derivatives on unstaggered, collocated grids. For example, the  $x$ -derivative of a general field component  $\Psi$  that is known at all grid points  $i$  along the  $x$ -direction can be computed as follows:

$$\left. \frac{\partial \Psi}{\partial x} \right|_i = F^{-1} [-jk_x F(\Psi)], \quad (3.6)$$

where  $k_x$  is the Fourier-transform variable representing the  $x$ -component of the numerical wave vector and  $F$  and  $F^{-1}$  denote, respectively, the forward and the inverse discrete Fourier transforms along the  $x$ -direction. The Fast Fourier Transform (FFT) algorithm is used to implement the approximation. The potential limitation caused by the periodic boundary conditions inherent in the FFT can be eliminated by use of absorbing boundary conditions. Note that, according to the Nyquist sampling theorem, the representation of approximation (3.6) is exact for grid-sampling densities of two or more cells per wavelength. Hence any dispersion errors in the PSFD method introduced here arise only from the second-order-accurate central differences on the staggered, uncollocated Cartesian space lattice along the  $z$ -direction. We note

that there is a potential problem with the PSFD for focused, compact, delta-function type sources, since this type of source, which represents a spatially discretized delta function, may cause difficulties when using the FFT. However, we can avoid this difficulty by employing the pole-series expansion technique described above. After combining (3.5) and (3.6), the magnetic field at height  $z_{k-1}$  can be expressed with the magnetic field and its derivative on the unstaggered grid as

$$\begin{cases} H_x(i, j, k - 0.5) = H_x(i, j, k + 0.5) - \Delta z \cdot F^{-1}[-jk_x F(H_z)] \\ H_y(i, j, k - 0.5) = H_y(i, j, k + 0.5) - \Delta z \cdot F^{-1}[-jk_y F(H_z)] \\ H_z(i, j, k - 0.5) = H_z(i, j, k + 0.5) + \Delta z \cdot [F^{-1}[-jk_x F(H_x)] + F^{-1}[-jk_y F(H_y)]] \end{cases} \quad (3.7)$$

### 3.4. Noise analysis in the PSE and PSFD approaches

The relation between a measured data point  $d_j$  and the prediction of a forward model at the same point (which we denote  $F_j$ ) can be expressed as

$$d_j = F_j(\mathbf{m}) + \varepsilon_j, \quad (3.8)$$

where  $j$  is one of  $N$  data points,  $\mathbf{m}$  is a vector of model parameters, and  $\varepsilon_j$  is the error of the  $j$ -th datum. In general the error can fall into one of two categories: a) those related to the uncertainties in modeling parameters (like sensor positioning and orientation) not included in the model vector  $\mathbf{m}$  which produce errors in the predicted data, and b) those that are strictly related to the sensor, even in the absence of a target: the effects of instrument drift and electronics noise, among others. All of these errors in the data enter (3.8) as an additive term, and usually appear in the inverse problem through the data covariance matrix. The data covariance matrix adjusts  $d_j$ , the relative contribution of each data point to the objective function, and therefore controls how closely each datum is fit by the predicted data. In our subsequent analysis we assume independently distributed Gaussian random errors.

## 3.5. Results

### 3.5.1 PSE applied to a dipole

We designed various studies to demonstrate the applicability of the PSE approach for determining SFS and hence for estimating the location of a buried object. We initially placed a magnetic dipole at the origin of a Cartesian coordinate system and calculated its magnetic field from 30 cm to 40 cm. We used the field values in this segment to determine the PSE expansion coefficients and then predict the magnetic field at a segment between  $-60$  cm and  $60$  cm. A comparison between the PSE predictions and the actual fields, depicted on Figure 3.3, shows that the PSE has a reasonable predicting power.

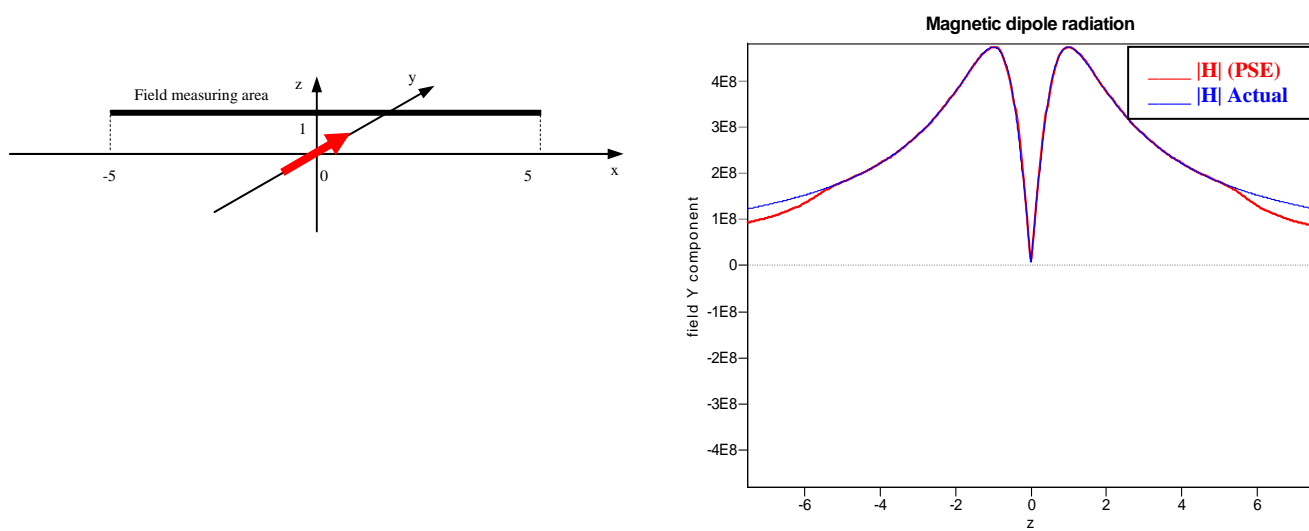
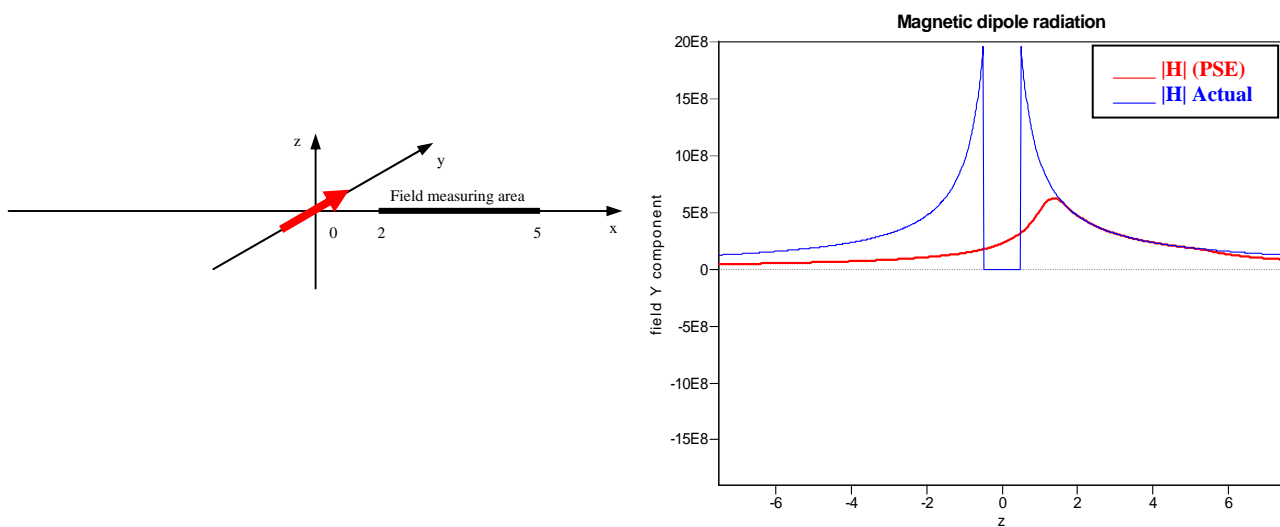


**Figure 3.3.** Comparison between predicted and actual fields for a magnetic dipole.

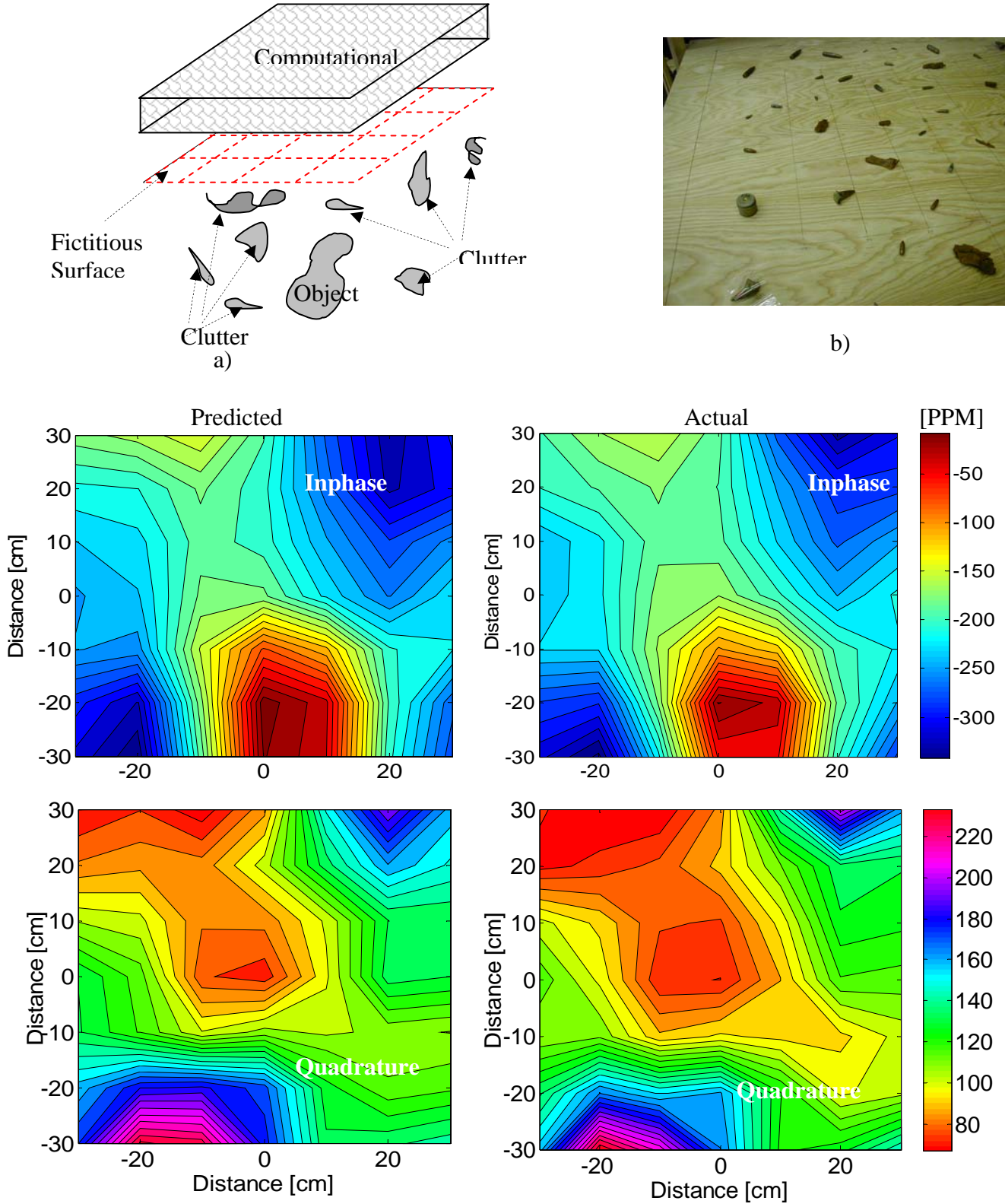


**Figure 3.4.** (a) Experimental setup for  $H_z$  field upper continuation and (b) clutter items used in the experiment. Plots: Inphase (top) and quadrature (bottom)  $H_z$  field distribution on the measurement plane as predicted by NSMS (left) and measured by the GEM-3 (right).

### 3.5.2. Extending the EMI field upwards

In this section we present results of further numerical experiments carried out to assess the applicability of the combined NSMS/PSFD method for determining the location of a buried object without having to solve a time-consuming minimization problem. First we compare an extended EMI magnetic field computed via NSMS to measured frequency-domain data. In these tests, the NSMS model was used to extend monostatic EMI data above the measurement plane (which corresponds to the bottom plane of the “computational space” shown on Figure 3.4). The scattered magnetic field is produced by a set of magnetic charges placed on a fictitious surface. This fictitious surface is divided into small patches (Figure 3.4), and at each subsurface the normal component of the primary magnetic field is determined. The amplitudes of the magnetic charges at each subsurface are scaled by the normal component of the actual primary magnetic field. The NSMS amplitudes are determined by matching the modeled magnetic field to the measured field at a selected set of grid points on the measurement plane. Once these amplitudes are found, the scattered EMI field is extended into the computational space. Note that the NSMS sources are distributed on a fictitious plane surface placed between the ground and the computational space, corresponding to the red grid on 0. In this arrangement the NSMS reproduce the magnetic fields radiated by all the metallic objects distributed beneath the fictitious surface. For NSMS validation, we distributed various clutter items (shown in 0) on the plane surface and collected data at  $7 \times 7$  grid points on two surfaces using a GEM-3 sensor. The GEM-3 consists of two parallel concentric circular transmitter loops with currents flowing in opposite directions and scaled so that the total primary field vanishes at the common center, where a receiver coil is located. The transmitter loops are idealized as infinitely thin line sources with radii  $a_1$  and  $a_2$  and currents  $I_1$  and  $I_2 = -I_1 a_2/a_1$ . The NSMS were distributed on a plane surface 5 cm above the clutter surface. Matching the NSMS-modeled magnetic field to the actual data at  $h = 10$  cm above the clutter surface enabled us to determine the amplitudes of the NSMS, which we then used to compute the scattered mono-static field at  $7 \times 7$  points on a plane 15 cm above the clutter surface. The GEM-3 data were collected on the same surface and using the same grid points. The actual GEM-3 data, at 210 Hz, are depicted on the right column of Figure 3.4; the left column shows the  $z$ -component of the magnetic field as predicted by the NSMS model. We find very good agreement between the predicted field and the measured data, which demonstrates that the NSMS model can be used successfully to extend EMI data in a given computational space.

### 3.5.3. Combining NSMS and PSE

A nice feature of the NSMS technique is that it can be used to generate both monostatic and bistatic data for any given sensor. Bistatic data is important when determining locations and orientations of buried objects using the pole-series expansion technique described here. However, most if not all current state-of-the-art EMI sensors are monostatic. The NSMS method readily clears this hurdle by performing an accurate data conversion from monostatic to bistatic. To illustrate this we solve the complete EMI scattering problem for a highly permeable and conductive cylinder using a method of auxiliary sources/thin skin approximation (MAS-TSA) code and use the results to determine the MAS-based standardized excitation approach (MAS-SEA) coefficients. We then generate MAS-SEA monostatic data on the grid  $x \in [-60 \text{ cm}, 60 \text{ cm}]$ ,  $y \in [-60 \text{ cm}, 60 \text{ cm}]$ ,  $z = 45 \text{ cm}$  at 10-cm increments for the cylinder subject to the primary magnetic field of the GEM-3 sensor. In the next step we distribute NSMS sources on a flat surface with  $x \in [-80 \text{ cm}, 80 \text{ cm}]$ ,  $y \in [-80 \text{ cm}, 80 \text{ cm}]$ ,  $z = 20 \text{ cm}$ , that is conformal to but does not coincide with the measurement surface. In this arrangement, the NSMS reconstructs the

magnetic fields radiated by all metallic objects distributed in the space  $z < 0$ . The amplitudes of the NSMS are determined by solving a linear system of equations and enable us to simulate the bistatic scattered EMI field on the grid, which we can then compare with the data generated by the MAS-SEA code. Figure 3.5 shows one such comparison, both on a grid (panels (a) and (b)) and along a transect (panel (d)). Panel (c) shows the difference between simulated and predicted data. We see that the NSMS method can reconstruct bistatic data from monostatic data very accurately.

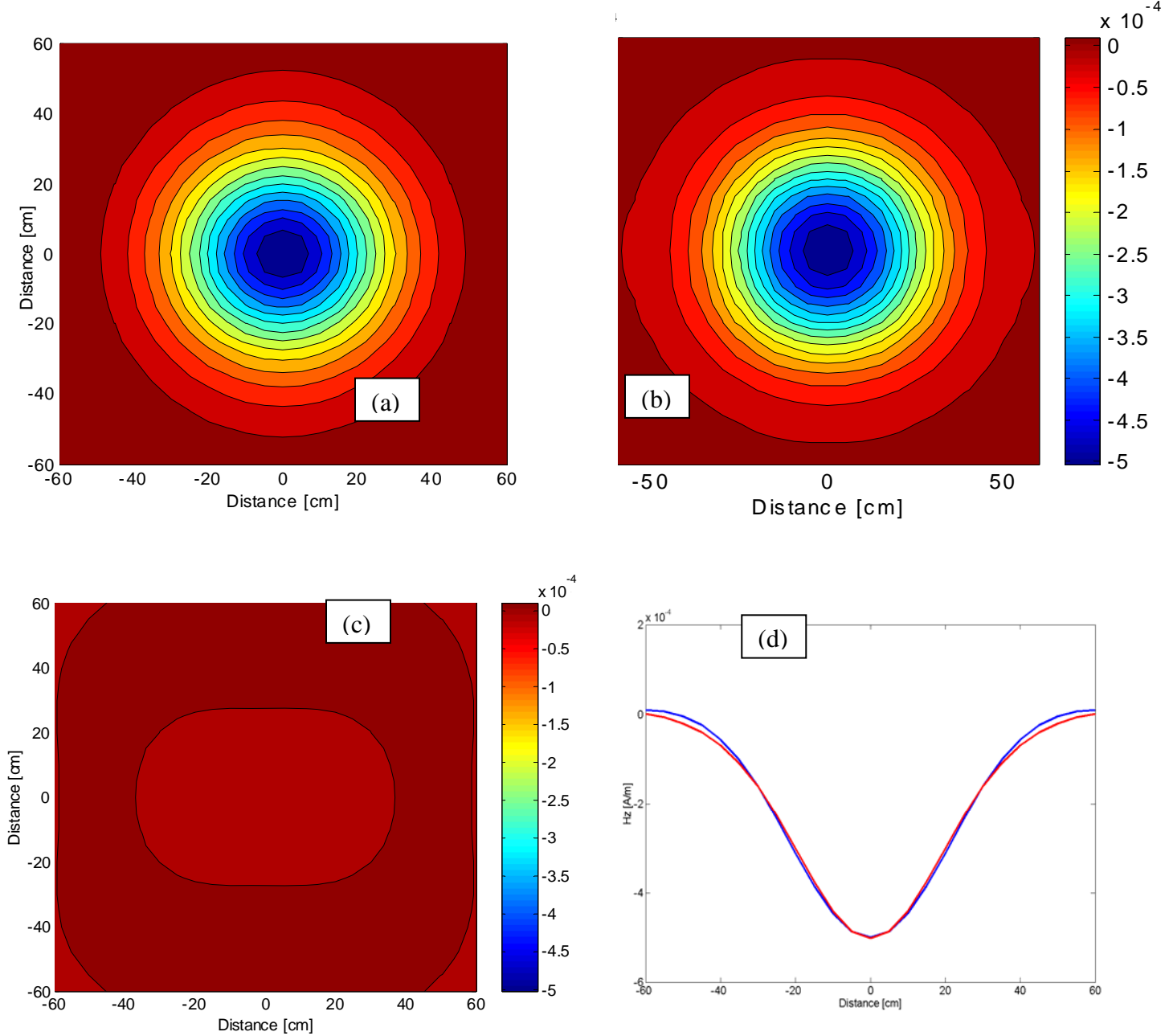


**Figure 3.5**  $H_z$  bistatic magnetic field on a grid.

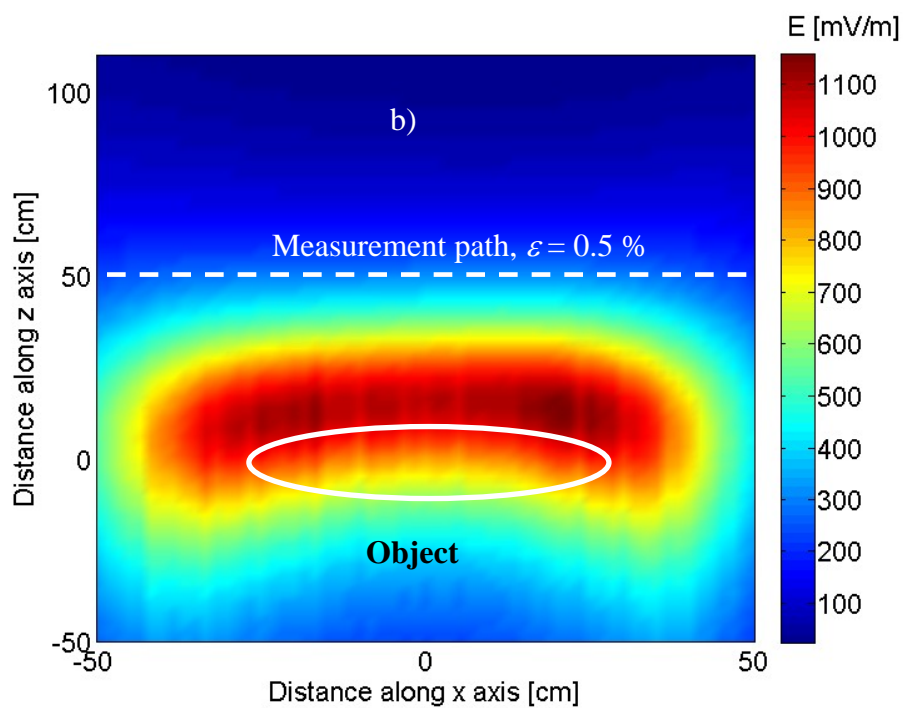
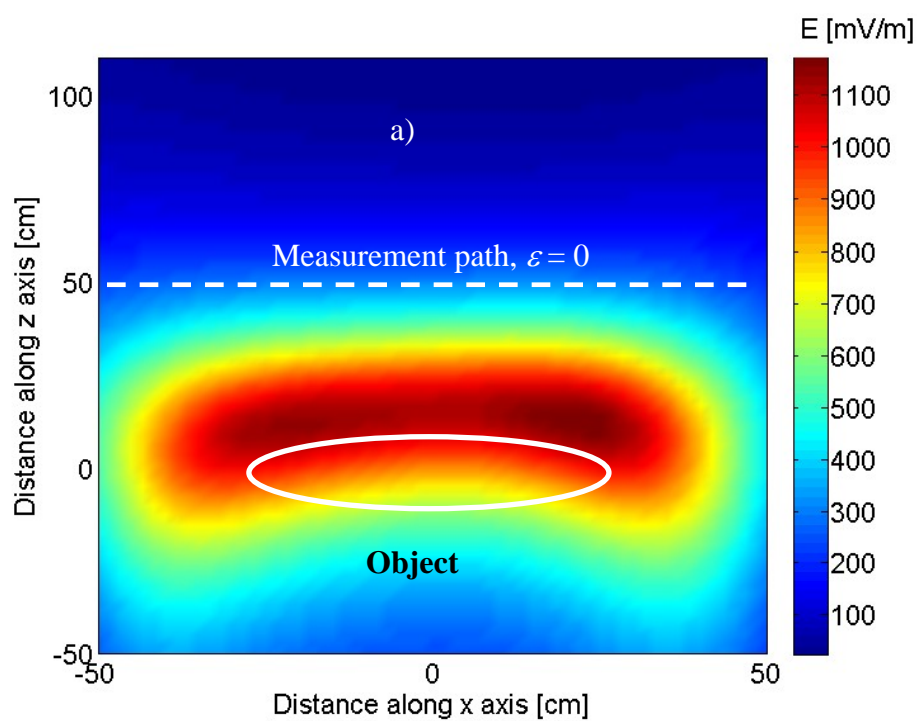


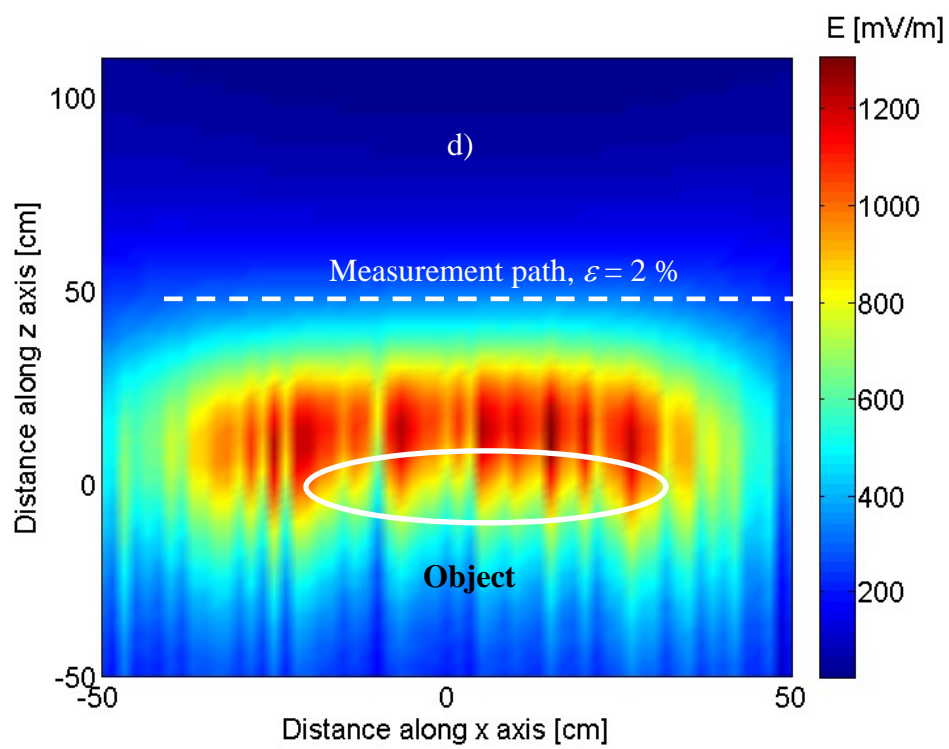
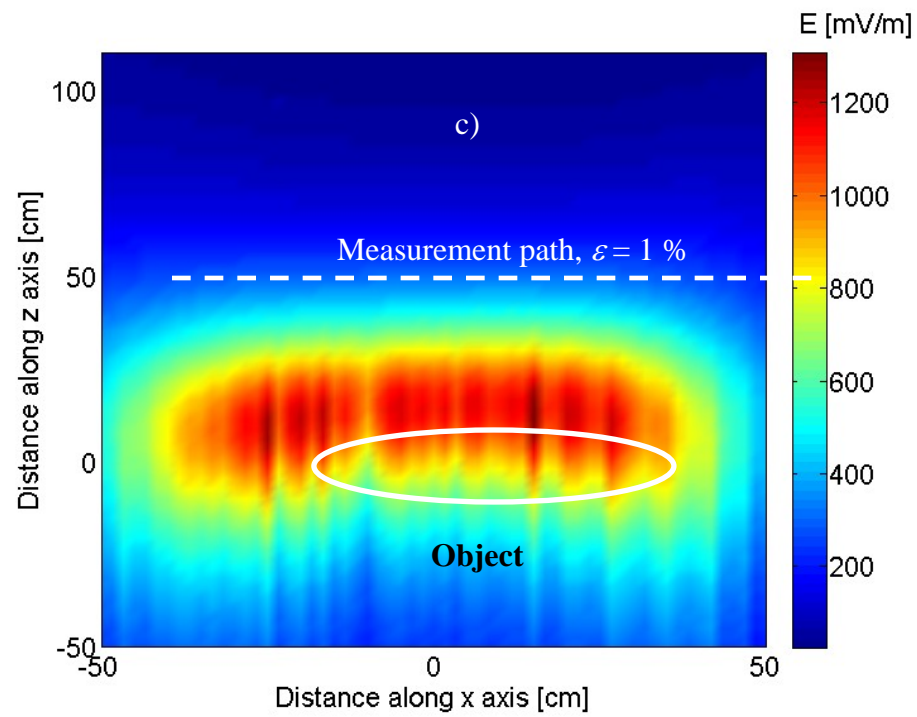
### 3.5.4. PSE-NSMS applied to measured EM-63 data

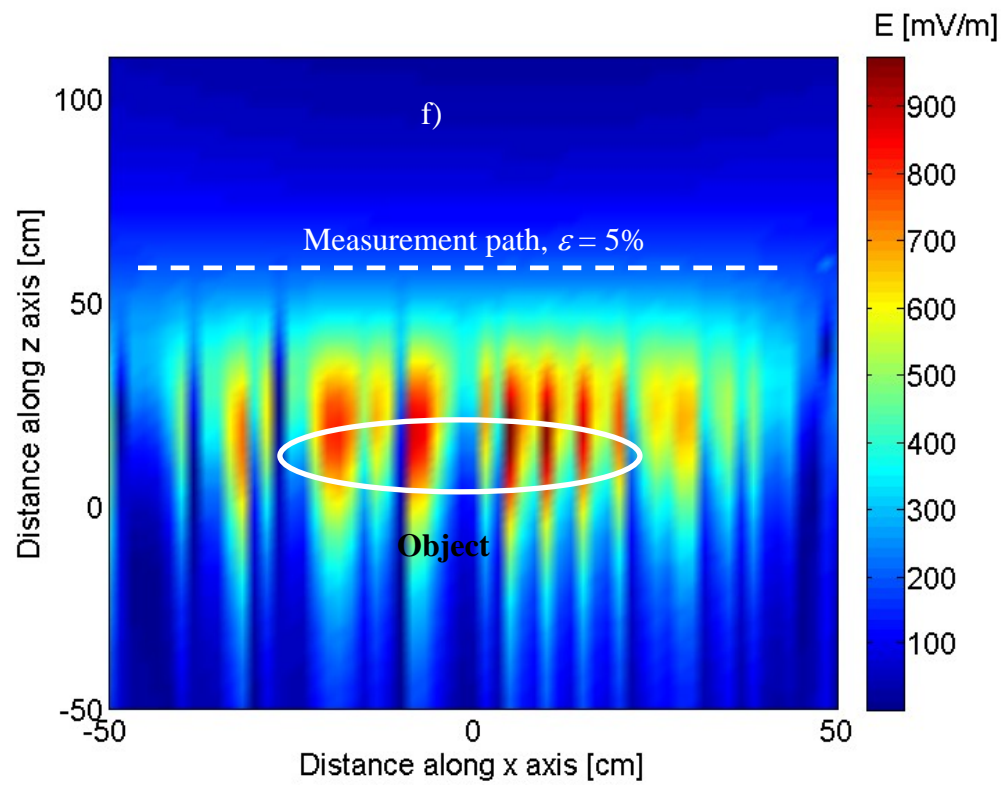
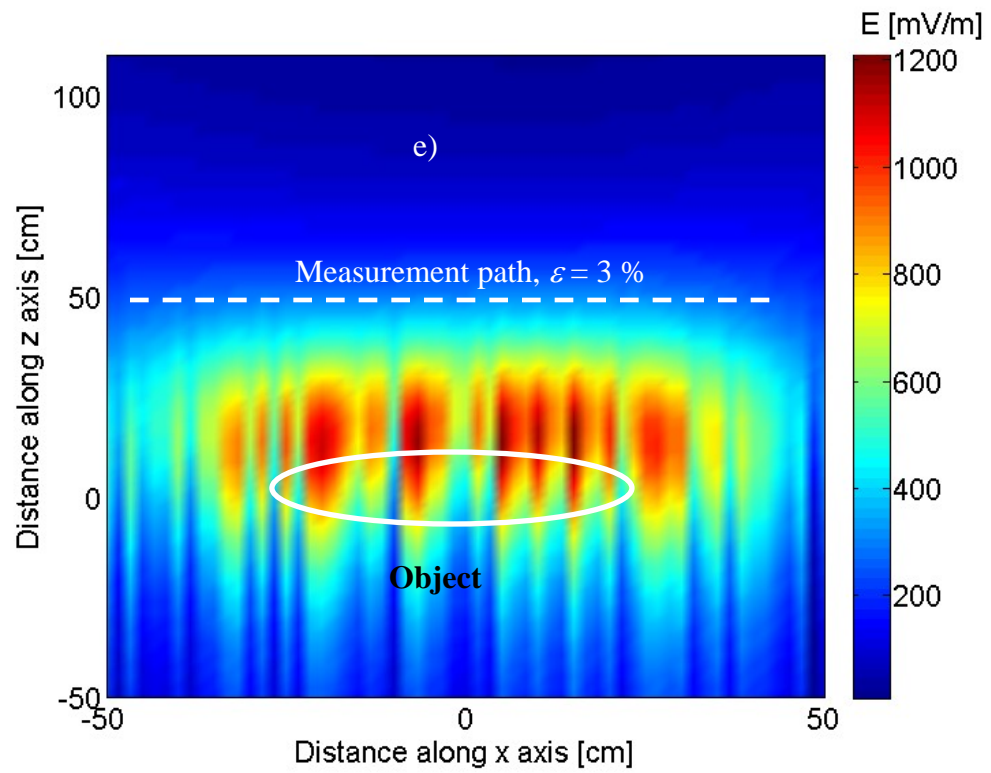
To demonstrate the applicability of the combined NSMS-pole series expansion method we then placed an actual UXO (a 2.75-inch projectile) in the magnetic field of the EM-63 sensor. Data were collected at the UXO test-stand site over a set of grid points on a surface with  $x \in [-1.5 \text{ m}, 1.5 \text{ m}]$ ,  $y \in [-1.5 \text{ m}, 1.5 \text{ m}]$ ,  $z = 60 \text{ cm}$ . NSMS were distributed on a flat surface with the same  $x$ - $y$  range as the measurement surface and  $z = 0$ . In this arrangement, the NSMS reconstruct the magnetic fields radiated by all metallic objects distributed in the space  $z < 0$ . The NSMS amplitudes were determined by solving a linear system of equations and used to extend the scattered EMI field above the measurement surface at  $z = 60 \text{ cm}$ . In order to illustrate the full potential of the PSE-NSMS approach for position determination we also conducted a noise analysis: to the NSMS-predicted  $H_z(x, y, z)$  magnetic field signals we added random noise as

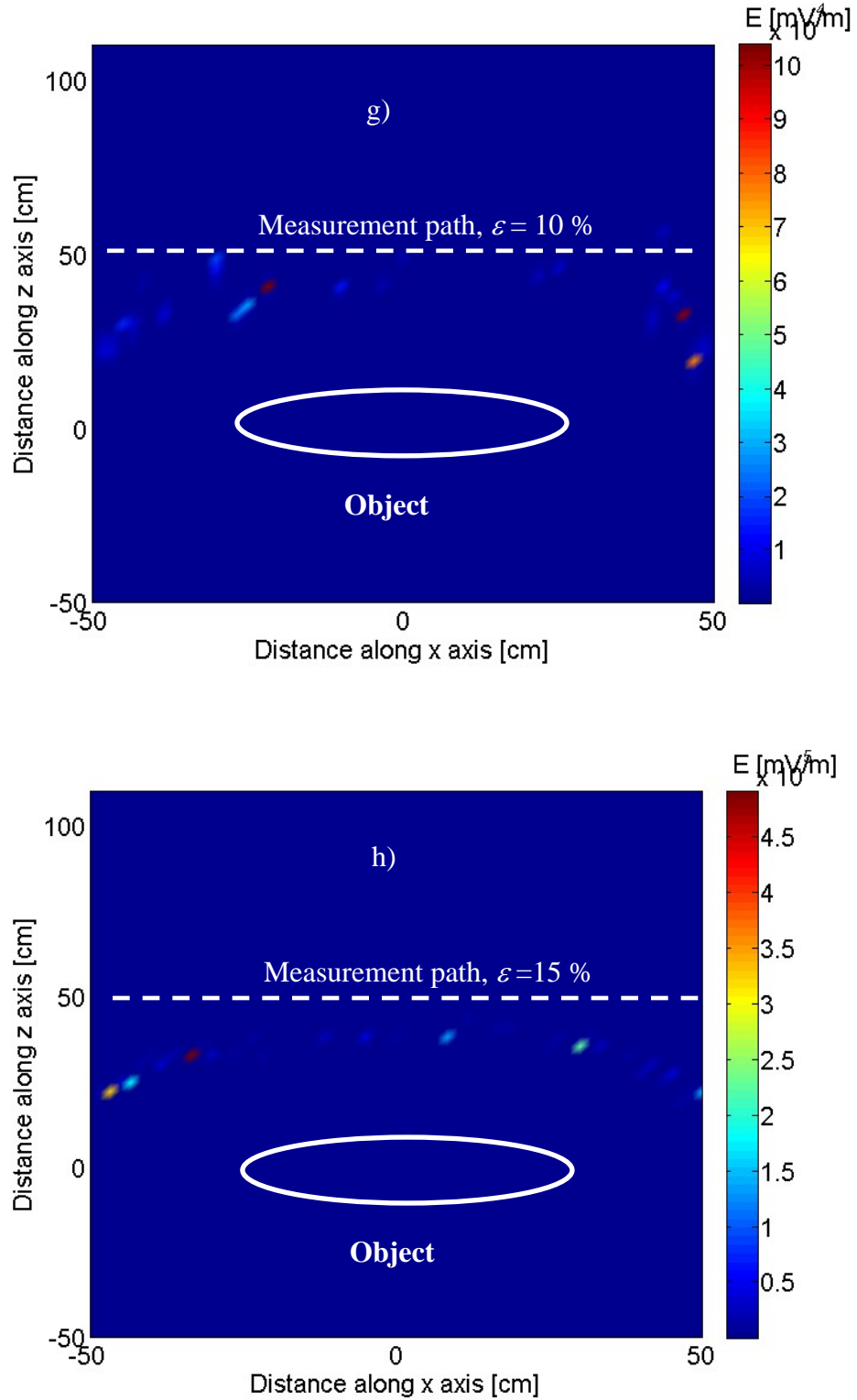
$$H_z(x, y, z) = H_z^{\text{nsms}}(x, y, z) + \varepsilon(z), \quad (3.9)$$

where  $H_z^{\text{nsms}}(x, y, z)$  is the scattered magnetic field above the measurement surface and  $\varepsilon(z)$  is a Gaussian random variable. The magnetic field predicted by the NSMS model at the first time channel is depicted in Figure 3.6 for different noise levels over the  $x$ - $z$  plane with  $y = 0$ . The scattered magnetic field is computed on a plane with  $x \in [-50 \text{ cm}, 50 \text{ cm}]$  and  $z \in [-50 \text{ cm}, 110 \text{ cm}]$ ; the target is oriented horizontally. For each fixed  $x$  we use the field values along the  $z$ -axis to determine the pole expansion coefficients (with  $n = 6$ ,  $d = 6$ ) and reconstruct the magnetic field. The computation is straightforward and very fast. The maximum of the reconstructed field distribution (*i.e.*, the SFS) is found to be near the object for very low noise levels (5% or less); however, as the noise level increases the algorithm becomes unstable and the predicted field distribution scatters around. Similar tests were performed for the same 2.75-inch mortar inclined  $45^\circ$ . The results, depicted on Figure 3.7, lead to the same conclusion as before: the maximum of the inverted field is distributed around the object and is sensitive to the noise. We can also see that the object's orientation is very difficult to estimate.

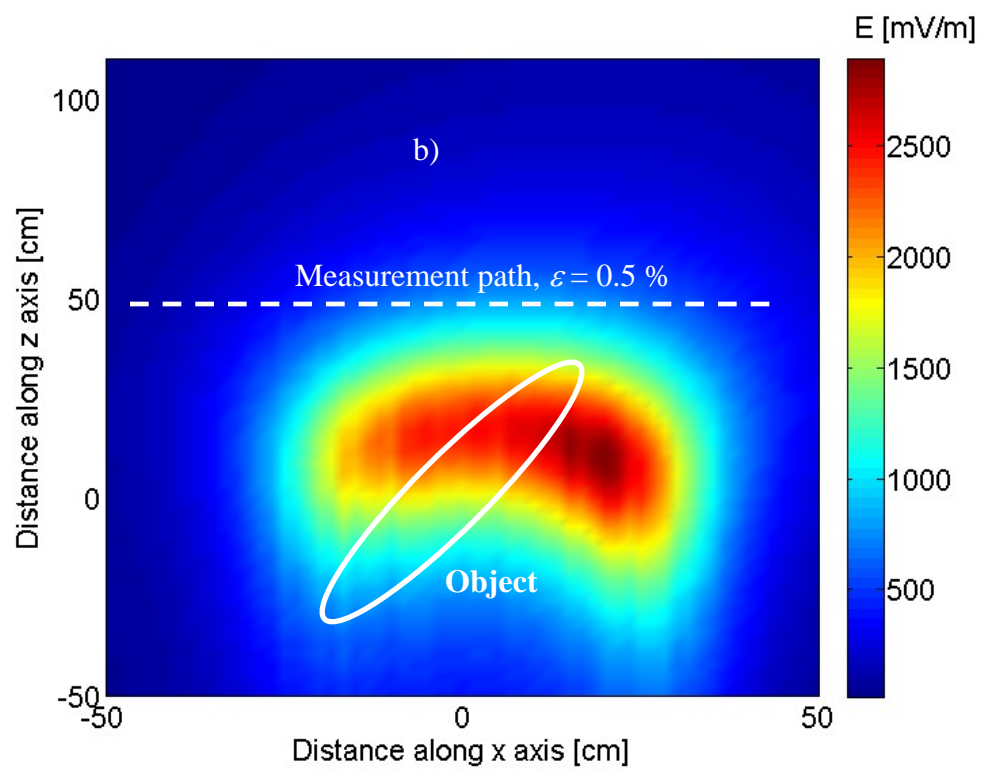
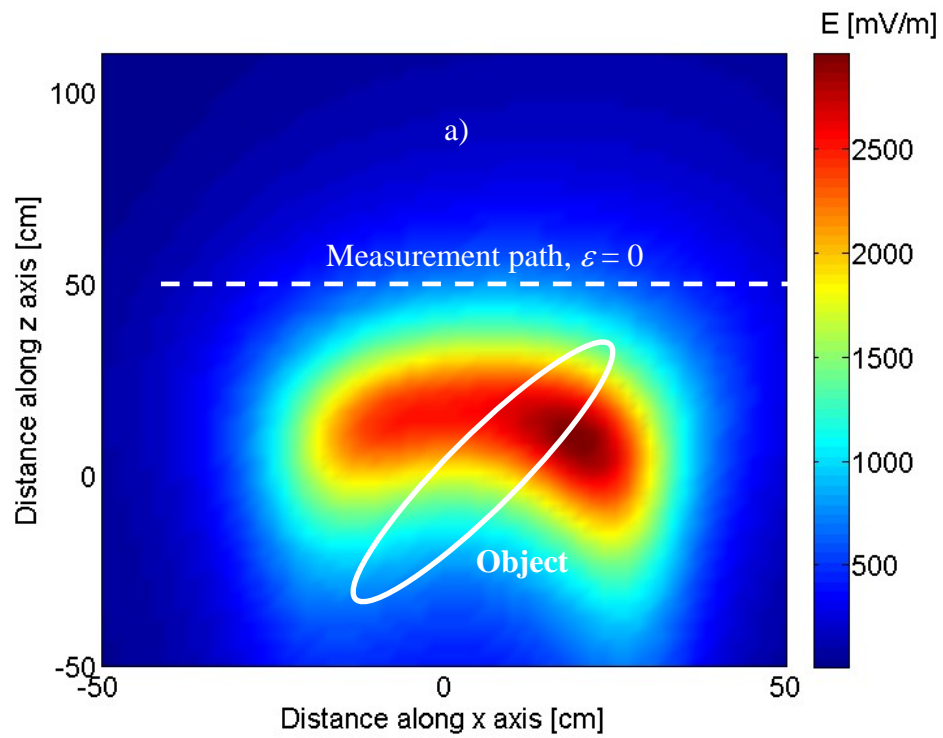


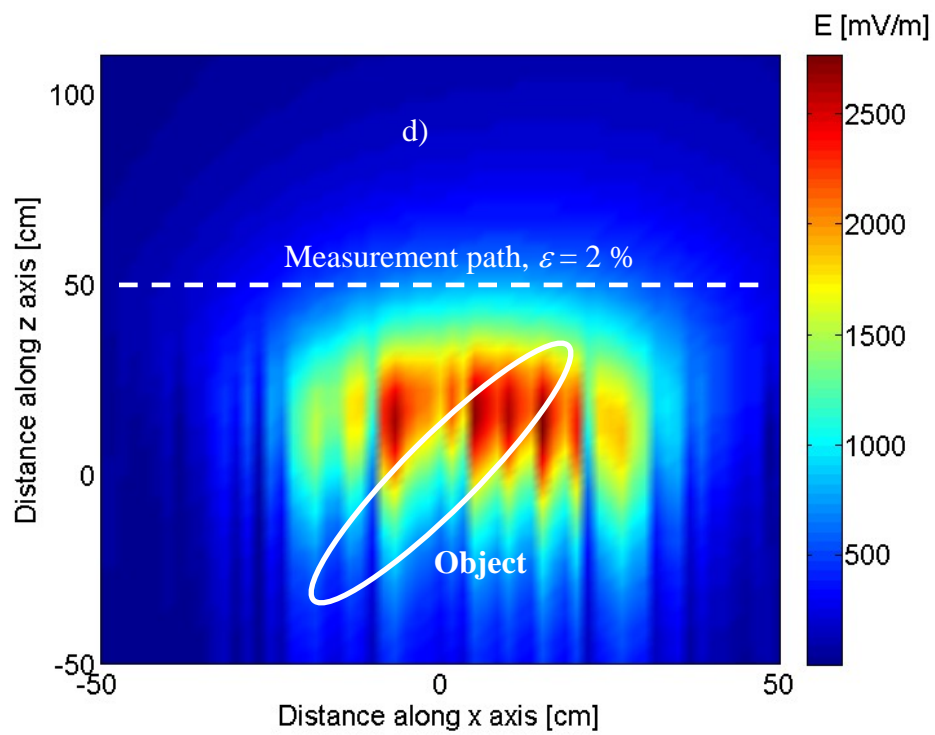
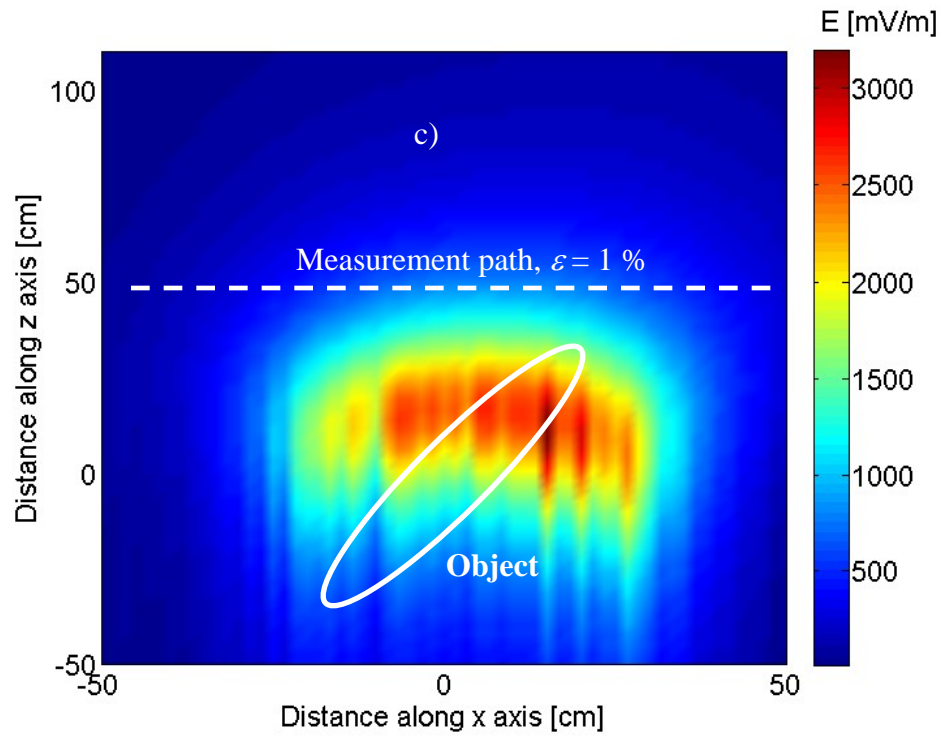




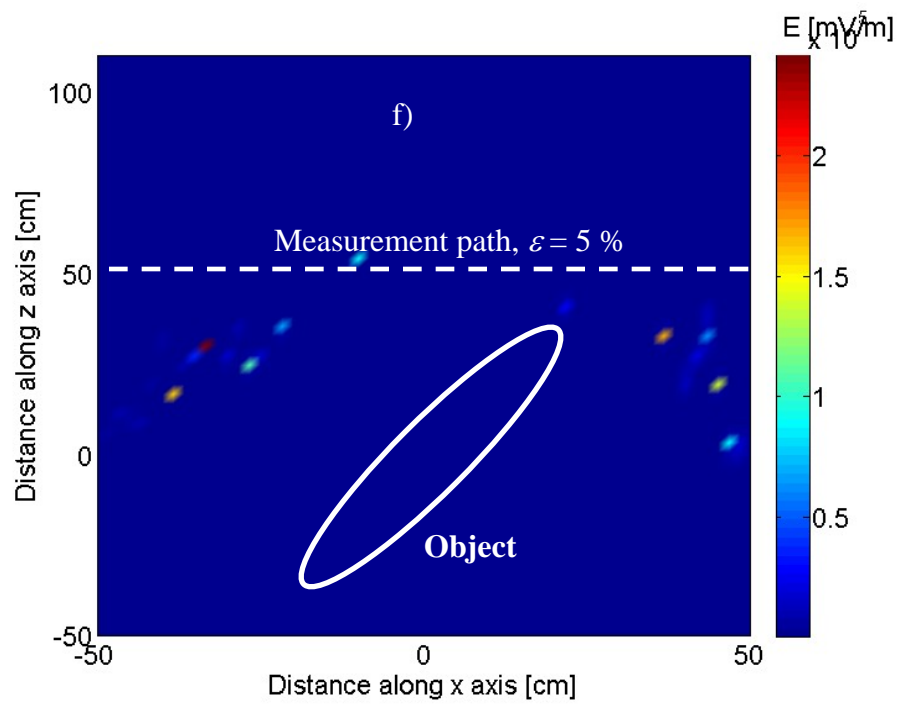
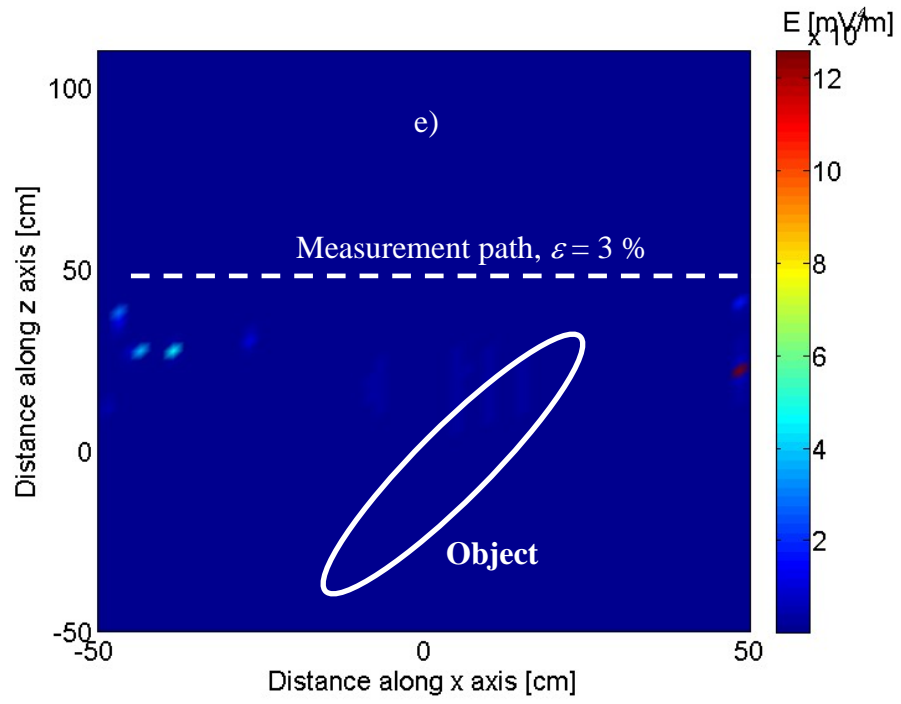


**Figure 3.6.** Distribution of predicted  $H_z$  magnetic field intensity over the  $x$ - $z$  plane for a 2.75-inch rocket oriented horizontally and interrogated by the GEM-3 sensor. The different panels correspond to increasing noise levels: (a) 0%, (b) 0.5%, (c) 1%, (d) 2%, (e) 3%, (f) 5%, (g) 10%, (h) 15%.











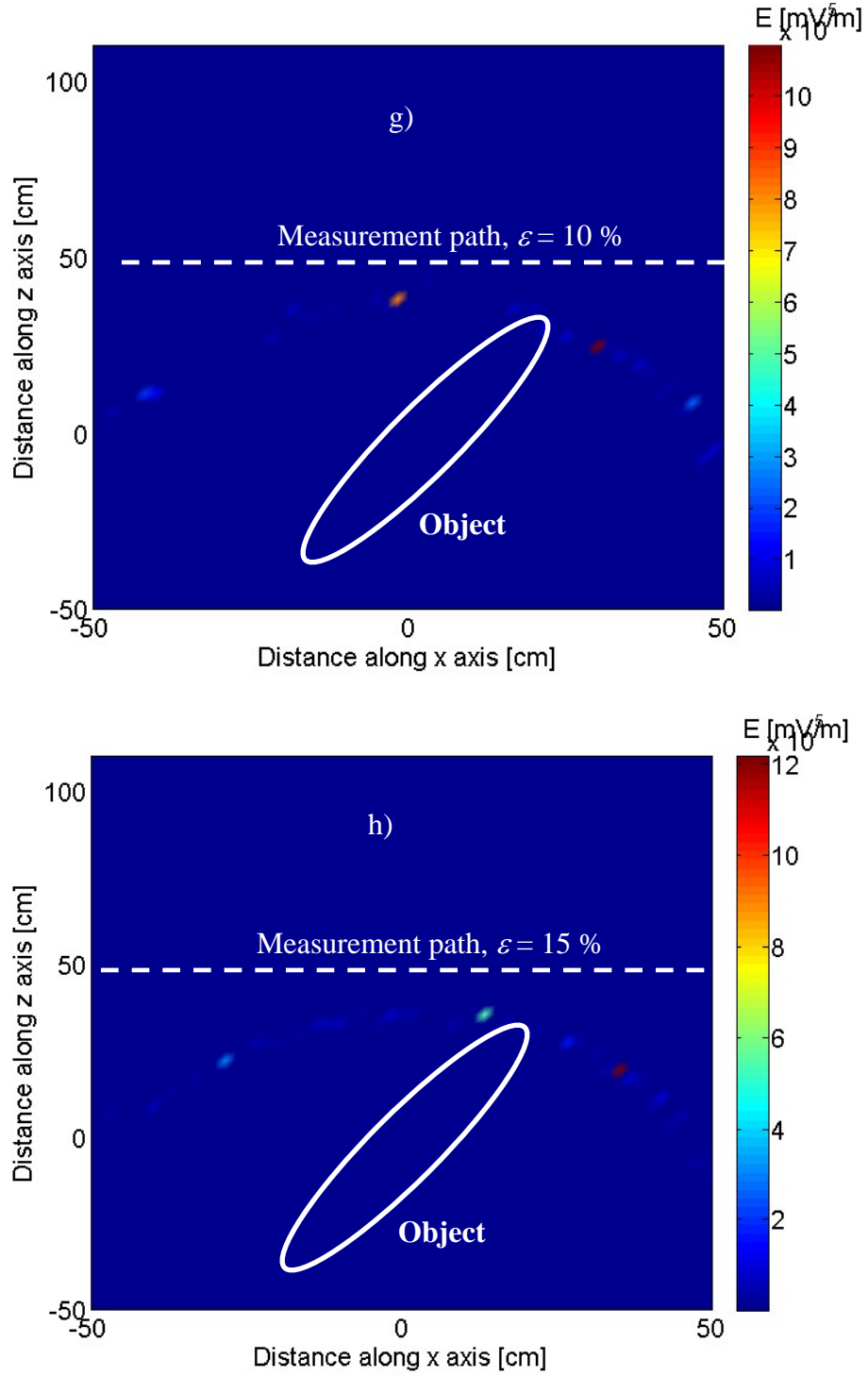


**Figure 3.7.** Distribution of predicted  $H_z$  magnetic field intensity over the  $x$ - $z$  plane for a 2.75-inch rocket at  $45^\circ$  inclination and interrogated by the GEM-3 sensor. The different panels correspond to increasing noise levels: (a) 0%, (b) 0.5%, (c) 1%, (d) 2%, (e) 3%, (f) 5%, (g) 10%, (h) 15%.

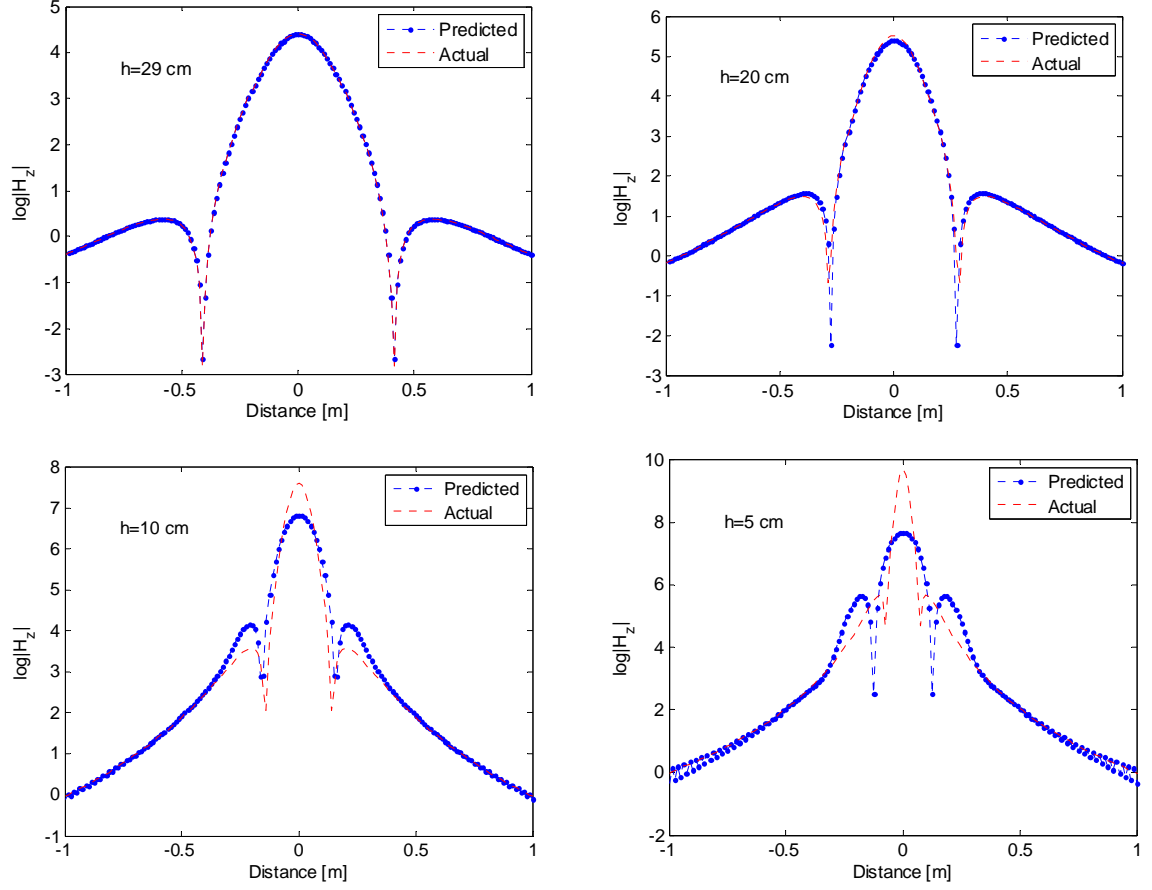


**Figure 3.8.** Predicted and actual scattered magnetic field of a sphere at different heights above the sphere center. The y-scale is logarithmic.

### 3.5.5. PSFD for refocusing the scattered magnetic field

In this final subsection we use the PSFD to determine the location of a buried object by refocusing the scattered magnetic field backwards to its origin. The PSFD technique requires bistatic data, which can be readily computed from monostatic data by using the NSMS method as described above. We consider a sphere placed in the primary magnetic field of the GEM-3 sensor. We generated synthetic data at a set of grid points on a surface with  $x, y \in [-2 \text{ m}, 2 \text{ m}]$  at heights  $h = z = 30 \text{ cm}$  and  $h = z + \Delta z$  in the Cartesian coordinate system of Figure 3.2. Figure 3.8 compares the actual magnetic fields of the sphere and the predictions based on (3.7) at different heights when  $\Delta z = 1 \text{ cm}$ . The predicted magnetic field matches the ground truth at  $h = 29, 20$ , and  $10 \text{ cm}$ . However, when the observation line is just above the sphere there are significant differences which arise because the secondary source is very concentrated. This situation causes difficulties for the FFTs in the PSFD approach but can be overcome by using the pole-series expansion method described in this chapter. Similar tests with  $\Delta z = 2 \text{ cm}$  yielded identical results, indicating that the PSFD method converges.

### 3.6 Conclusion

In this chapter we combined the pole-series expansion and pseudospectral finite-difference method with the normalized surface magnetic source approach to invert for the location of a buried object without solving a traditional ill-posed optimization problem. We first used NSMS to extend an EMI scattered field. Numerical tests confirmed that, as demonstrated in the previous chapter, the NSMS method accurately predicts monostatic EMI responses. We then employed the PSE or PSTD to focus a scattered magnetic field back to its origin. PSE-NSMS studies were done for a dipole and a 2.75-inch mortar under different levels of noise. We found that the PSE-NSMS technique is potentially able to estimate the depth of a buried object to an accuracy of plus or minus one characteristic length, which could be used as the initial guess in a nonlinear optimization. On the other hand, this technique is very sensitive to the noise level, which limits its usefulness for actual UXO detection and discrimination problems. We also tested the PSFD-NSMS approach for a sphere. Our results demonstrate that the PSFD-NSMS method can reconstruct the scattered magnetic field to an accuracy of plus or minus one sphere radius; however, it is difficult to make correct depth estimates with this algorithm, which moreover is computationally expensive and sensitive to noise.

## Chapter 4

### Scatterer localization using a left-handed-medium slab

#### 4.1. Introduction

Back in 1968, V. G. Veselago theoretically investigated materials with simultaneously negative permittivity and permeability, henceforth referred to as left-handed materials (LHMs), and pointed out some of their electrodynamic properties, such as the reversal of Snell's law, of the Doppler effect, and of Cerenkov radiation (Veselago, 1968). Veselago's ideas did not receive much attention at the time and were eventually forgotten because of the unavailability of LHMs. However, in 1996 the first artificial LHM was realized using periodic structures (Pendry *et al.*, 1996), and since then intense study has been conducted on the theory, experimental behavior, and potential applications of LHMs. As predicted by Veselago, a LHM slab can refocus electromagnetic waves from a point source. J. Pendry and collaborators (1996) extended Veselago's ideas and further predicted that evanescent waves could be amplified through an LHM slab and that the source information could be reconstructed at the perfect imaging point without loss of amplitude (Pendry *et al.*, 1996; 1999). Similar tests have been done for spatially distributed sources (such as Gaussian beams) propagating through a slab of a left-handed medium (Ziolkowski, 2003), and it has been reported that Gaussian beams at normal incidence can be focused in a planar LHM slab. Since then most of the research activity on LHMs has focused on the development of actual LHM devices, such as perfect lenses, resonators, etc. The aim of this project was to investigate the possibility of applying LHMs and their refocusing properties as a virtual mathematical tool to help determine the location and geometric parameters of a buried object from measured data without having to solve an ill-posed inverse-scattering problem. We would like to emphasize that this approach does not require any hardware, since it is based exclusively on the mathematical properties of LHMs.

#### 4.2. Governing equations in the EM wave regime

According to Maxwell's equations, in a LH medium characterized by  $\varepsilon < 0$  and  $\mu < 0$  the plane-wave relations between electric ( $\mathbf{E}(\mathbf{r}) = \mathbf{E}_0 e^{-j\mathbf{k} \cdot \mathbf{r}}$ ) and magnetic ( $\mathbf{H}(\mathbf{r}) = \mathbf{H}_0 e^{-j\mathbf{k} \cdot \mathbf{r}}$ ) fields take the form

$$\mathbf{k} \times \mathbf{E} = -\omega |\mu| \mathbf{H} \quad (4.1)$$

and

$$\mathbf{k} \times \mathbf{H} = \omega |\varepsilon| \mathbf{E}, \quad (4.2)$$

where a time dependence  $e^{j\omega t}$  is assumed. As a result, the electric field, the magnetic field, and the wave vector  $\mathbf{k}$  form a left-handed triad. Thus the wave vector  $\mathbf{k}$ , and therefore also the phase

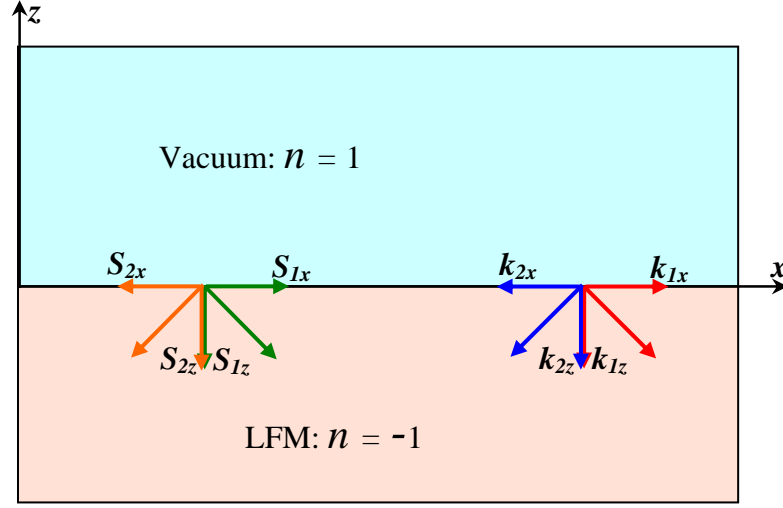


**Figure 4.1.** Configuration of Poynting vectors ( $\mathbf{S}$ ) and wave vectors ( $\mathbf{k}$ ) in a LHM half-space.

velocity  $\mathbf{v}_\phi$ , exhibit a *sign opposite* to that in a conventional right-handed medium (Figure 4.1). At the same time, Poynting's theorem is still given by

$$\mathbf{S} = \mathbf{E} \times \mathbf{H}^*, \quad (4.3)$$

which indicates that the electric and magnetic fields and the Poynting vector  $\mathbf{S}$  are still related through the *right-hand rule* (see Figure 4.1). Thus the Poynting vector  $\mathbf{S}$ , and therefore also the group velocity  $\mathbf{v}_{\text{gr}}$ , point in the same direction as the propagation of energy, as in right-handed (RH) media, thereby satisfying the causality requirement. Combining observations of the directions of  $\mathbf{k}$  and  $\mathbf{S}$  demonstrates that in a LHM the phase and group velocities are *antiparallel* (*i.e.*, of opposite sign), and that the wave fronts travel *toward the source*.

To better understand EM scattering and refocusing phenomena in LH materials, let us consider a TE-polarized wave (electric field perpendicular to the plane of incidence) incident on a LHM half-space, as shown in Figure 4.2. The reflected and transmitted waves are known to satisfy the law of reflection and Snell's law:

$$\theta_i = \theta_r, \quad (4.4)$$

$$n_t \sin \theta_t = n_i \sin \theta_i, \quad (4.5)$$

where the index of refraction of each medium ( $\beta = i, t$ ) is given by the expression

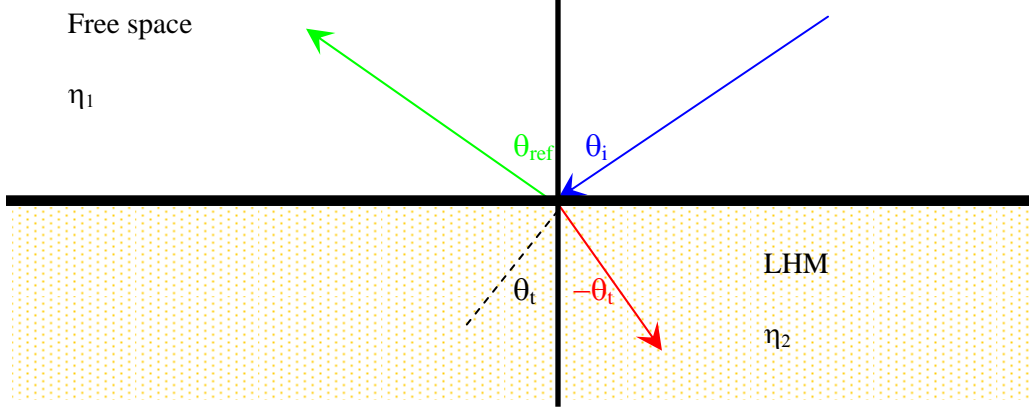


**Figure 4.2.** Interface between free space and a LHM showing a negative angle of refraction.

$$n_i = \sqrt{\frac{\epsilon_i}{\epsilon_o}} \sqrt{\frac{\mu_i}{\mu_o}} = \sqrt{\mu_r} \sqrt{\epsilon_r}, \quad (4.6)$$

where  $\epsilon_o$  and  $\mu_o$  are respectively the permittivity and the permeability of free space. The reflection and transmission coefficients are given by

$$R = \frac{\eta_t \cos \theta_i - \eta_i \cos \theta_t}{\eta_t \cos \theta_i + \eta_i \cos \theta_t} \quad (4.7)$$

and

$$T = \frac{2\eta_t \cos \theta_i}{\eta_t \cos \theta_i + \eta_i \cos \theta_t}, \quad (4.8)$$

where the wave impedance in medium  $\beta$  is

$$\eta_\beta = \sqrt{\frac{\mu_\beta}{\epsilon_\beta}}. \quad (4.9)$$

In most cases below we consider a left-handed metamaterial matched to free space. This means that  $\epsilon_r < 0$  and  $\mu_r < 0$  so that  $n < 0$ , and that  $\eta_t = \eta_i$ . Consequently, for a LHM with  $n = -1$  one finds  $R = 0$  and  $T = 1$ . Moreover, Snell's Law indicates that the transmitted angle is negative for oblique incidence (at any angle) on the interface. The negative angle of refraction has the effect of refocusing the electromagnetic field back to the origin. In other words, the planar LHM behaves as a perfect lens.

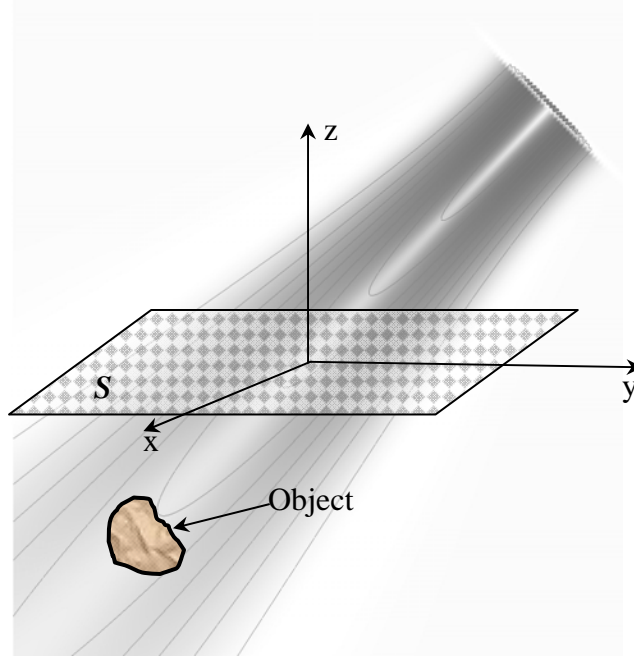


**Figure 4.3.** Schematic diagram of a 2D EM problem.

### 4.3. Boundary conditions at a free-space/LHM interface

Let us examine now the boundary conditions (BCs) for electromagnetic fields at the interface between free space and a LH medium. The *tangential* components of  $\mathbf{E}$ ,  $\mathbf{H}$ , and  $\mathbf{k}$  do not “see” the discontinuity and are therefore transmitted from one medium to another unaffected. Mathematically, the boundary-value problem for the tangential components can be summarized as follows:

$$\hat{\mathbf{n}} \times (\mathbf{H}^{\text{pr}} + \mathbf{H}^{\text{obj}}) = \hat{\mathbf{n}} \times \mathbf{H}^{\text{LHM}} \quad (4.10)$$

$$\hat{\mathbf{n}} \times (\mathbf{E}^{\text{pr}} + \mathbf{E}^{\text{obj}}) = \hat{\mathbf{n}} \times \mathbf{E}^{\text{LHM}}$$

where  $\hat{\mathbf{n}}$  is a unit vector normal to the surface,  $\mathbf{E}^{\text{pr}}$  and  $\mathbf{H}^{\text{pr}}$  are the primary electric and magnetic fields,  $\mathbf{E}^{\text{obj}}$  and  $\mathbf{H}^{\text{obj}}$  are the measurable/recordable scattered electric and magnetic fields due to the object, and  $\mathbf{E}^{\text{LHM}}$  and  $\mathbf{H}^{\text{LHM}}$  are the total electric and magnetic fields inside the LHM, which we wish to reconstruct. In contrast, the *normal* components of the electric and magnetic vectors undergo a *change of sign* at the interface in addition to the usual discontinuity in magnitude. The sign changes for  $E_n$  and  $H_n$  come directly from the conditions  $\varepsilon_1 E_{1n} = \varepsilon_2 E_{2n}$  with  $\varepsilon_2 < 0$  and  $\mu_1 H_{1n} = \mu_2 H_{2n}$  with  $\mu_2 < 0$ , while the change of sign for  $k_n$  is a consequence of the condition  $n < 0$ .

#### 4.4. Refocusing of the scattered EM field using LHM

Let us consider a permeable and conducting two-dimensional metallic object buried in soil and illuminated with a primary electromagnetic field (Figure 4.3). (A time dependence  $e^{j\omega t}$  is assumed and suppressed throughout.) The primary electromagnetic field induces electric currents on the scatterer's surface, which in turn produce a secondary or scattered field outside. The scattered electromagnetic field is measured/recorded at a set of measurement points. Our goal is to use this measured secondary EM field to determine the location of the object. To do so, we first assume that the measurement surface is a boundary between free space and a LHM. Then the scattered EM field is considered as a primary EM field on the virtual/fictitious free-space/LHM boundary. Third, the electromagnetic boundary-value problem is solved, and finally the EM field is mapped inside the LHM. In the regime considered here the electromagnetic fields are governed by vector wave equations. In the 2D case an electromagnetic field can be represented with a scalar potential that satisfies the Helmholtz equation,

$$(\nabla^2 + k_\beta^2) U = -J_z \delta(\mathbf{\rho} - \mathbf{\rho}'), \quad (4.11)$$

where  $k_\beta$  is the wave number (measured in  $\text{m}^{-1}$ ) in medium  $\beta$  and  $U$  is the scalar potential. Thus the problem is cast in terms of solutions of the Helmholtz equation inside each medium. This boundary-value problem can be solved using the method of auxiliary sources.

#### 4.5. The method of auxiliary sources for LHM in the EM-wave regime

The method of auxiliary sources (MAS) is a numerical technique originally developed for solving a wide class of scattering and radiation electromagnetic problems that recently has also been applied to various electromagnetic induction (EMI) problems (Zaridze *et al.*, 2002; Shubitidze *et al.*, 2002; Anastassiou *et al.*, 2002; Shubitidze *et al.*, 2004). It has been widely demonstrated to be a general, robust, and accurate numerical method for the study of EMI scattering by highly conducting and permeable targets, and has been used to solve complex large-scale electromagnetic scattering and antenna problems. Because of its reduced computational complexity, the method shows great potential for simulating realistically elaborate electromagnetic situations, particularly those involving multiple objects. Briefly, in the MAS, boundary value problems are solved numerically by representing the electromagnetic fields in each domain of the structure under investigation by a finite linear combination of analytic solutions of the relevant field equations, corresponding to sources situated some distance away from the boundaries of each domain. The “auxiliary sources” producing these analytical solutions are chosen to be elementary currents located on fictitious surfaces that usually conform to the actual surface(s) of the structure. In practice, only points on the auxiliary and actual surfaces are required, so it is not necessary to resort to the detailed mesh structures required by other techniques such as the finite element method and the boundary element method.

For a simple one-dimensional uniform half-space with given permittivity and permeability we require two auxiliary surfaces, one inside and one outside the scattering object (*i.e.*, the half-space). The fields outside the half-space (region 1) are considered to originate from a set of auxiliary sources  $\{a_i\}$  placed inside the half-space (surface  $S_1^{\text{aux}}$ ), while the interior fields (region 2) arise from a set of auxiliary sources  $\{b_i\}$  placed outside (surface  $S_2^{\text{aux}}$ ). The auxiliary currents  $\{a_i\}$  and  $\{b_i\}$  radiate in an unbounded homogeneous space filled respectively with the



characteristics of region 1 and region 2. The electric and magnetic fields in regions 1 and 2 are linked by the boundary conditions (4.10), which are enforced at an array of selected points on the physical surface  $S$  corresponding to the interface.

The electric field generated by this current density is described by

$$\mathbf{E}(x, z) = -\frac{\omega\mu_0}{4} I_o H_o^{(2)}(k_o \sqrt{(x-x_o)^2 + (z-z_o)^2}), \quad (4.12)$$

where  $H_0^{(2)}$  is the zeroth-order Hankel function of the second kind and  $k_0$  and  $\mu_0$  are the free-space wave number and magnetic permeability, respectively. The intensity of the radiated magnetic field is obtained via Faraday's law. The primary EM field impinges at the interface between the free half-space of region 1 and the dissipative medium of region 2; consequently, two secondary EM fields are generated. The first one, denoted by  $\mathbf{E}^{\text{obj}}$  and  $\mathbf{H}^{\text{obj}}$ , is the scattered field, which propagates in the free half-space, and the second one, denoted by  $\mathbf{E}^{\text{LHM}}$  and  $\mathbf{H}^{\text{LHM}}$ , is the refracted field that propagates in the LH medium. The incident field (and thus the entire geometry) is independent of the spatial  $y$  variable, and thus the problem can be worked out entirely on a plane. The scope of the next section is the determination of the EM fields within region 2—that is, the fields in the virtual LHM. Once the fields within each region are known, pertinent quantities of interest can be readily evaluated: the spatial electric current distribution that accounts for the electric loss mechanism, the polarization current induced in the lossy dielectric, and the total radiated field, among others.

Following a standard MAS formulation, two equivalent simulated situations are set up to mimic the original ones in regions 1 and 2. In region 1, the scattered field is simulated by the total field generated by a set (set I) of auxiliary sources, which are fictitious  $y$ -directed current filaments. As shown in Figure 4.4, these filaments are homogeneously distributed along an auxiliary surface parallel to the plane, at positions given by  $\mathbf{p}_{1i} = x_i \hat{\mathbf{x}} - d_1 \hat{\mathbf{z}}$  for the  $i$ -th auxiliary source of set I, where  $d_1$  is the distance between the physical interface and the auxiliary surface on which the current sources of set I lie. These filaments carry unknown currents and are treated as sources radiating in an unbounded free space. The unknown scattered electric field at the observation point in region 1 is described by the superposition of the radiated EM fields of the auxiliary sources of set I:

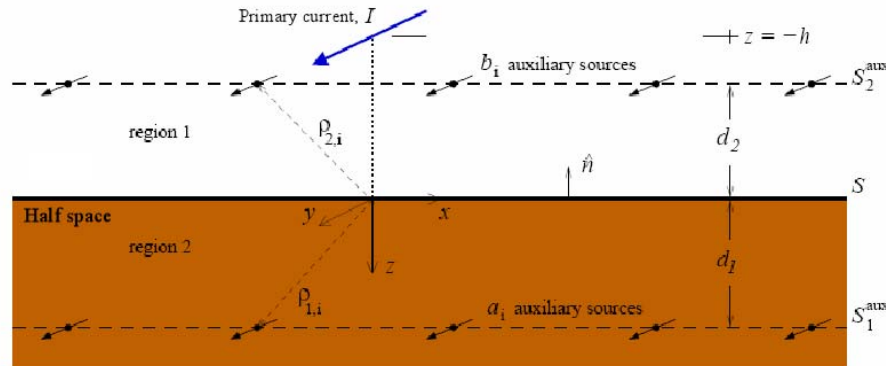


**Figure 4.4.** MAS geometry for a uniform half-space model.

$$E_y^{obj}(x, z) = -\frac{\omega\mu_0}{4} \sum_i a_i H_o^{(2)}(k_o \sqrt{(x-x_i)^2 + (z+d_1)^2}) . \quad (4.13)$$

Accordingly, the corresponding magnetic field components are expressed as

$$H_x^{obj}(x, z) = jk_0 \sum_i \frac{z+d_1}{4\sqrt{(x-x_i)^2 + (z+d_1)^2}} x \cdot a_i H_1^{(2)}(k_o \sqrt{(x-x_i)^2 + (z+d_1)^2}) , \quad (4.14)$$

$$H_z^{obj}(x, z) = -jk_0 \sum_i \frac{x-x_i}{4\sqrt{(x-x_i)^2 + (z+d_1)^2}} \cdot a_i H_1^{(2)}(k_o \sqrt{(x-x_i)^2 + (z+d_1)^2}) . \quad (4.15)$$

Similarly, in the dissipative half-space of region 2, as shown in Figure 4.4, the field is simulated by the superposition of the radiated fields of a set (set II) of  $b_i$  auxiliary sources, which are also  $y$ -directed current filaments and are once again homogeneously distributed along an auxiliary surface parallel to the plane. The  $i$ -th auxiliary source of set II is located at  $\mathbf{p}_{2i} = x_i \hat{\mathbf{x}} + d_2 \hat{\mathbf{z}}$ , where  $d_2$  is the distance between the physical interface and the auxiliary surface containing the auxiliary current sources of set II. The filaments carry unknown currents and are treated as sources radiating in an unbounded space filled with the LMH medium of region 2. The EM field within region 2 is then

$$E_y^{LHM}(x, z) = -\frac{\omega\mu_0}{4} \sum_i b_i H_o^{(2)}(k_1 \sqrt{(x-x_i)^2 + (z-d_2)^2}) . \quad (4.16)$$

The corresponding magnetic field components in the LHM can be expressed as

$$H_x^{LHM}(x, z) = jk_1 \sum_i \frac{z-d_2}{4\sqrt{(x-x_i)^2 + (z-d_2)^2}} \times a_i H_1^{(2)}(k_1 \sqrt{(x-x_i)^2 + (z-d_2)^2}) \quad (4.17)$$

and

$$H_z^{LHM}(x, z) = -jk_1 \sum_i \frac{x-x_i}{4\sqrt{(x-x_i)^2 + (z-d_2)^2}} \times b_i H_1^{(2)}(k_1 \sqrt{(x-x_i)^2 + (z-d_2)^2}) , \quad (4.18)$$

where

$$k_1 = k_o \sqrt{\varepsilon^{LHM}} \sqrt{\mu^{LHM}} \quad (4.19)$$

is the wave number in the LH material of region 2 and depends on the relative dielectric permittivity and magnetic permeability. The relation between the EM fields inside and outside the LH medium is dictated by the boundary conditions (4.10). More specifically, the tangential components of the electric and magnetic intensities must be continuous across the boundary plane. The unknown complex currents  $\{a_i\}$  and  $\{b_i\}$ ,  $i = 1, 2, 3, \dots, N$ , can then be calculated by imposing the boundary conditions (4.10) on  $2N$  collocation (matching) points on the interface. The enforcement of the boundary conditions at  $z = 0$  leads to the following equations:

$$\begin{aligned} H_o^{(2)}(k_1 \sqrt{x_m^2 + h^2}) + \sum_i A_i H_o^{(2)}(k_o \sqrt{(x_m - x_i)^2 + d_1^2}) \\ - \sum_i B_i H_o^{(2)}(k_1 \sqrt{(x_m - x_i)^2 + d_2^2}) = 0 \end{aligned} \quad (4.20)$$

for  $m = 1, 2, 3, \dots, M$ , and

$$\begin{aligned} \frac{-h}{\sqrt{x_m^2 + h^2}} H_1^{(2)}(k_o \sqrt{x_m^2 + h^2}) + \\ \sum_i A_i \frac{d_2}{\sqrt{(x_m - x_i)^2 + d_1^2}} H_1^{(2)}(k_o \sqrt{(x_m - x_i)^2 + d_1^2}) \\ - \sum_i B_i \frac{-d_2 k_o}{k_1 \sqrt{(x_m - x_i)^2 + d_2^2}} H_1^{(2)}(k_1 \sqrt{(x_m - x_i)^2 + d_2^2}) = 0 \end{aligned} \quad (4.21)$$

for  $m = 1, 2, 3, \dots, M$ , where  $A_i = a_i / I_0$  and  $B_i = b_i / I_0$  are the normalized currents of the filamentary fictitious current sources of sets I and II with respect to the current of the primary source  $I_0$ . The auxiliary sources of sets I and II and the collocation points are taken to be evenly spaced on their respective surfaces. The two boundary conditions (4.10) are strictly imposed at  $M = N$  or, alternatively, at  $M > N$  selected points on the plane, in which case the solution of (4.10) is correct in a least-squares sense. Usually we consider the former situation, in which the number of matching points is identical to the number of auxiliary sources; this leads to a linear matrix equation that can be subsequently solved (via standard square-matrix inversion techniques) for the  $2N$  unknown quantities  $A_i$  and  $B_i$  which correspond to the unknown currents. Once the linear system is solved, the EM fields in each region are readily computable using expressions (4.13)–(4.19).

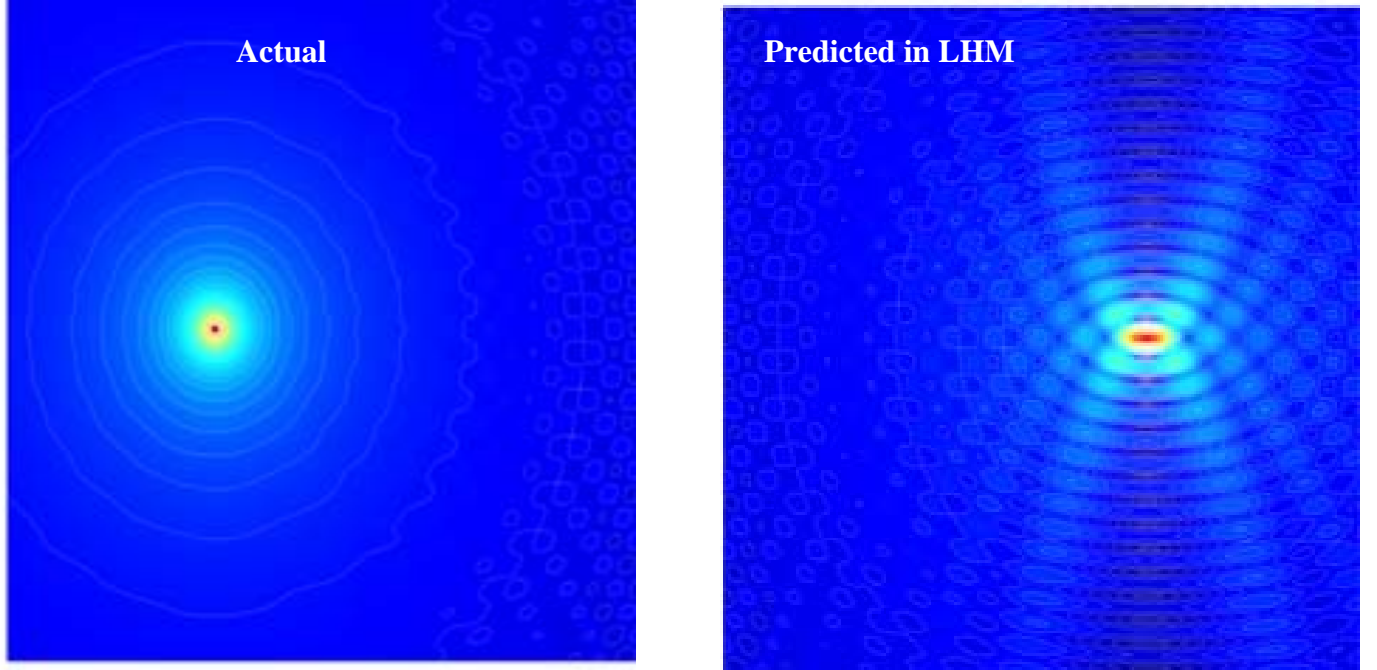


**Figure 4.5.** Electric field distribution around a point source (left) and MAS-predicted electric field distribution in a virtual LHM half-space with  $n = -1$  (right).

## 4.6. Numerical results

In this section we present numerical results that illustrate the capabilities of the LHM approach for estimating the location of a buried object. A computational code has been developed using the formulation of the previous sections and assuming equal numbers of inner and outer auxiliary sources. Imposing the EM boundary conditions at matching points with  $z = 0$  results in a square matrix system. Both the auxiliary sources and the collocation points are uniformly distributed along their respective surfaces. In our subsequent analysis we will assume  $\epsilon^{\text{LHM}} = \mu^{\text{LHM}} = -1$ . First, numerical tests are done in the electromagnetic wave regime, where the target's size is comparable to the relevant wavelength. Obviously this situation is very different from that encountered in UXO detection and discrimination using current EMI technologies. Therefore, at the end of this chapter we mention several steps that we took to extend the capabilities of the LHM approach to the EMI regime and discuss its practical implementation for realistic applications.

### 4.6.1. Point-source and Gaussian-beam illumination results

We consider point-source and Gaussian-beam illumination cases to study whether a planar LH medium can refocus the incident beam or not. We first investigate the point-source refocusing problem. A point source placed at a distance  $h = 30$  cm produces a field on the boundary between free space and the fictitious LH material which we take as the incident field on the interface. Using the boundary conditions we can determine the amplitudes of the internal and

external auxiliary sources and then use those to simulate the EM fields inside the virtual LHM space. Figure 4.5 shows the actual field from a point source (left) and the field predicted using the MAS responding amplitudes (right). Comparing the two panels we can see that the predicted field is a mirror image of the actual source field, up to the source location. The distance between the interface and the original and image sources is virtually the same.

Next we consider a Gaussian beam impinging obliquely on the boundary. The beam was constructed using a complex radiation source. The amplitude of the incident field varies spatially as  $\exp(-(x^2 + y^2)/w)$  and has many wave vectors associated with it. The wave vectors off the beam axis point away from the axis for a diverging beam and towards it for a converging beam. It was expected that a LHM with negative index of refraction would focus the beam; *i.e.*, it would bend the wave vectors of a diverging beam back towards the beam axis. The electric field intensity produced by the Gaussian beam source in free space is shown on the left panel of Figure 4.6. The highest values are colored red; the lowest values are blue. The beam is clearly diverging as it propagates away from the origin.

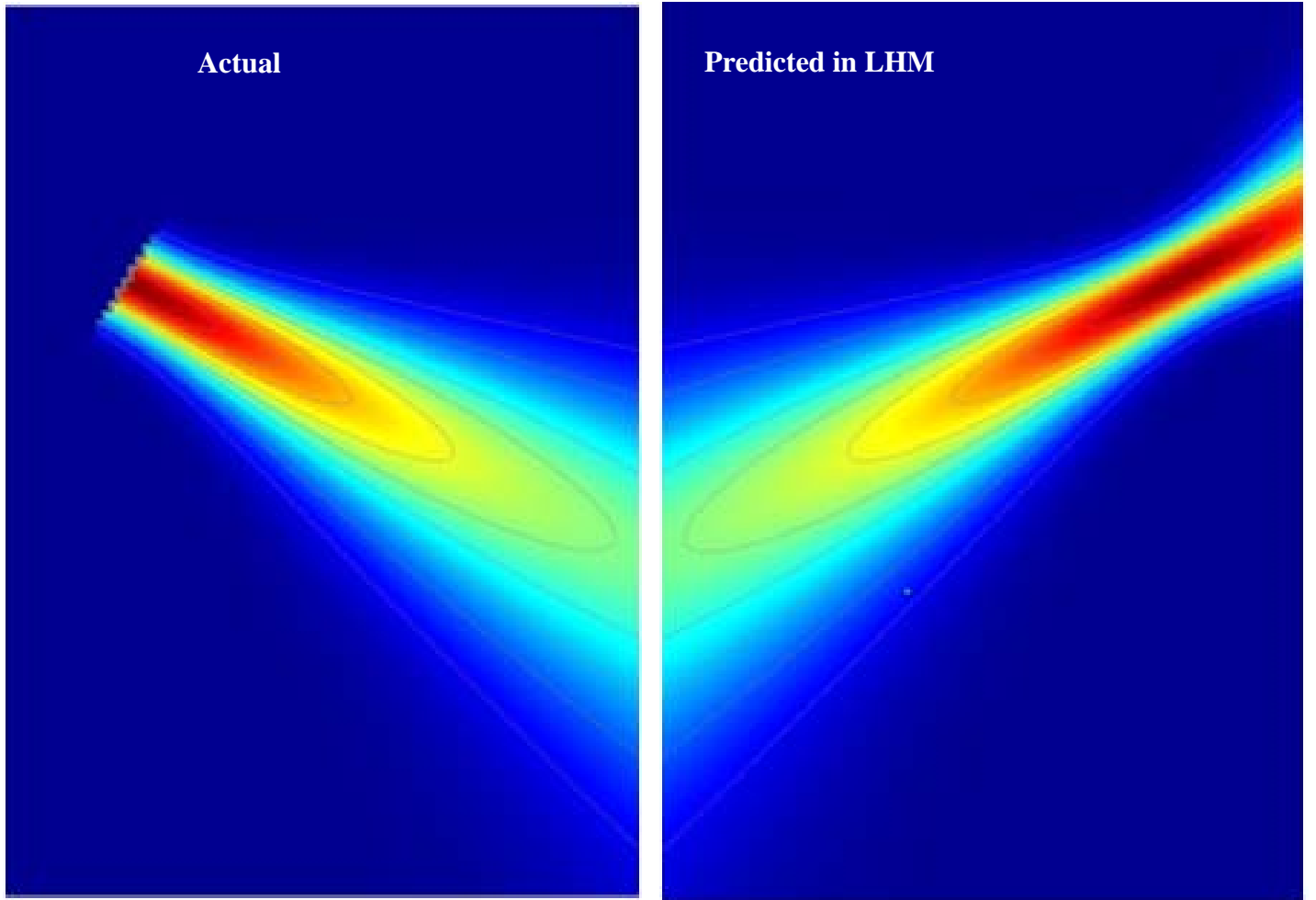


**Figure 4.6.** Electric field distribution from a Gaussian beam (left) and MAS-predicted electric field distribution in a virtual LHM half-space with  $n = -1$  (right).

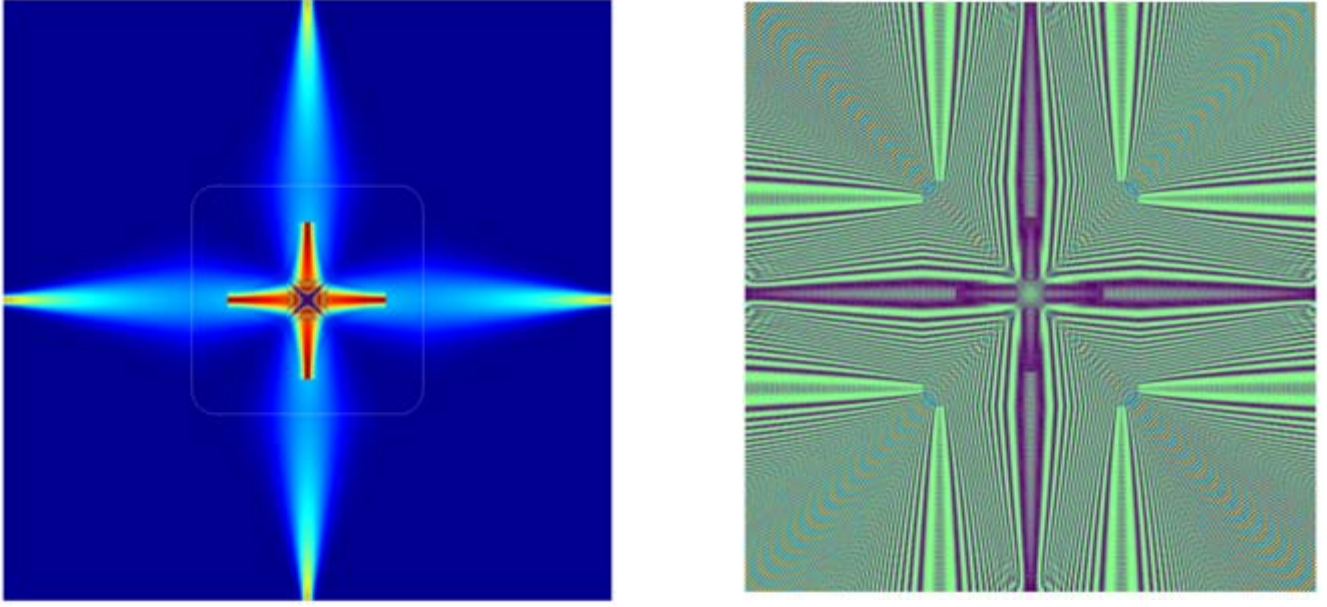


**Figure 4.7.** Four Gaussian beam sources placed in a virtual LHM space with  $n = -1$ . Left: electric field-intensity distribution. Right: phase distribution.

The right-hand panel of Figure 4.6 shows the reconstructed beam inside a LHM half-space with  $n = -1$  after solving the full EM problem. The beam source in the simulation was placed at a distance of 50 cm, and the wavelength is 3 cm; the interface boundary ranged between  $-5$  m and  $5$  m. The predicted result clearly shows that the LH planar medium turns the diverging wave vectors toward the beam focus point and, hence, acts as a lens that focuses the beam. As mentioned in the previous paragraph, the distance between the interface boundary and the original source coincides with that between the boundary and the reconstructed source. This means that the LHM half-space ideally reproduces the actual beam in the high-frequency EM regime.

#### 4.6.2. LHM applied to multiple sources and objects

In this section the LHM approach is applied to scenarios involving multiple objects. We first consider the reconstruction of four Gaussian beam sources enclosed within a virtual LHM with  $n = -1$ . The MAS technique is used to solve the EM boundary value problem and predict the EM field in the LHM space. The resulting field-intensity and phase distributions are shown in Figure 4.7. The field-intensity distribution clearly shows that the LHM refocuses the EM field from the individual targets without losing information on the individual scatterers. In addition, the phase distribution illustrates that the LHM technique requires very accurate matching conditions on the boundary. This indicates that the technique could potentially face problems in the detection and discrimination of subsurface objects in noisy environments (as is the case in any realistic UXO-related application).



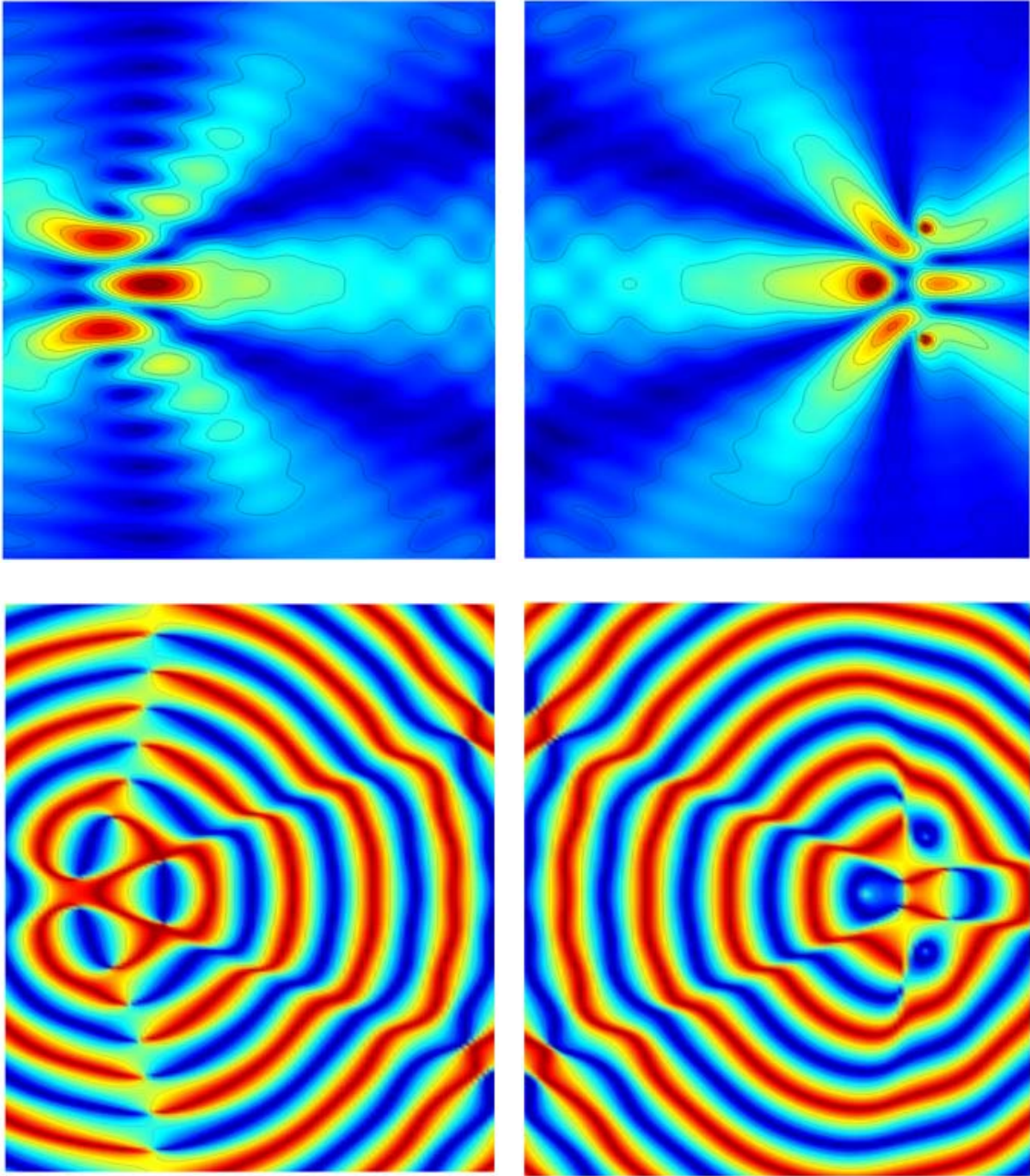


**Figure 4.8.** Actual (in free space, at left) and reconstructed (in a LHM with  $n = -1$ , at right) electric field-intensity (top row) and phase (bottom row) distributions for three point sources.

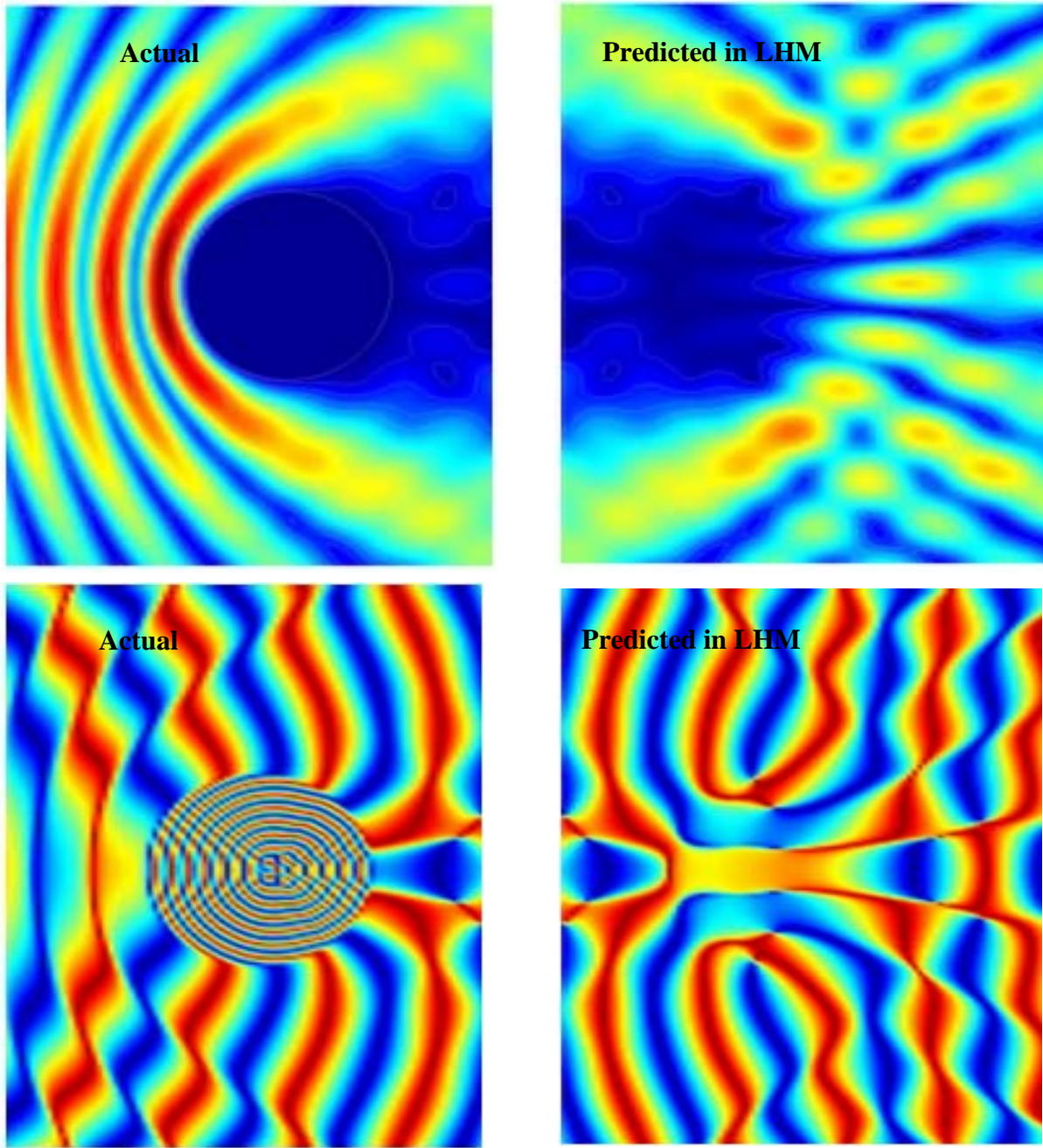


**Figure 4.9.** Actual (in free space, at left) and reconstructed (in a LHM with  $n = -1$ , at right) electric field intensity (top row) and phase (bottom row) distributions for a cylindrical scatterer.

To further illustrate the capability of the virtual LHM as a way of detecting and separating radiating objects we consider three point sources placed in free space and separated by one wavelength. The LHM reconstruction algorithm is implemented as before: the EM fields from the sources are calculated on the boundary between free space and the virtual LHM. No other information is given. By solving a linear least-squares problem we can reconstruct the EM fields inside the virtual LHM space. The actual (left) and reconstructed (right) distributions of



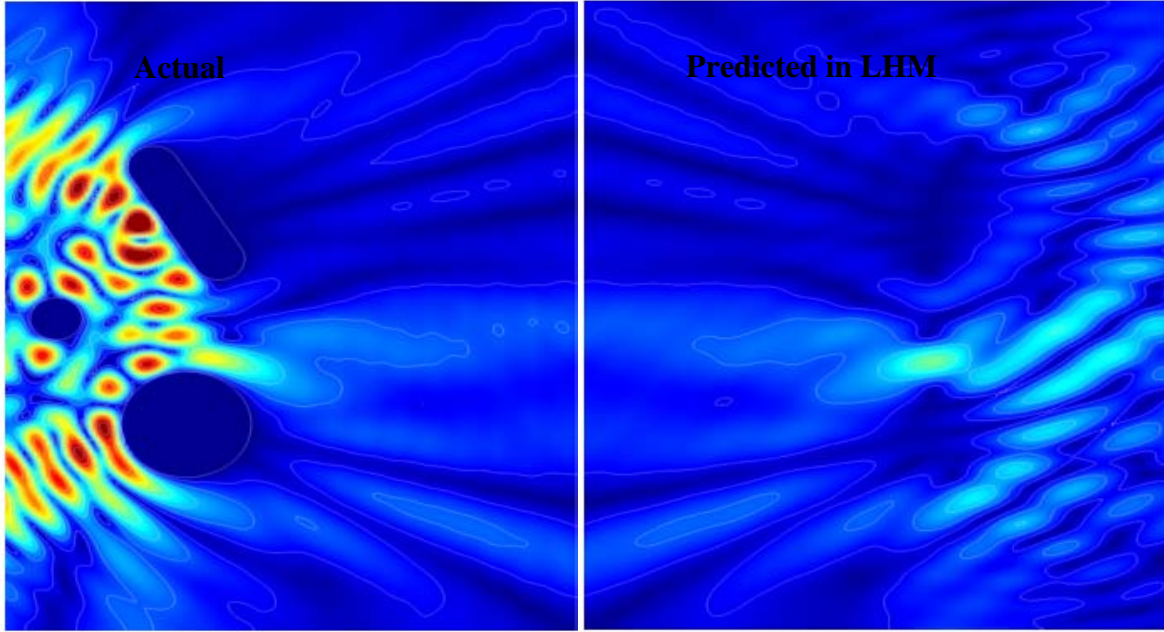


**Figure 4.10.** Electric field intensity distribution for three objects: actual (in free space, at left) and reconstructed (in a LHM with  $n = -1$ , at right).

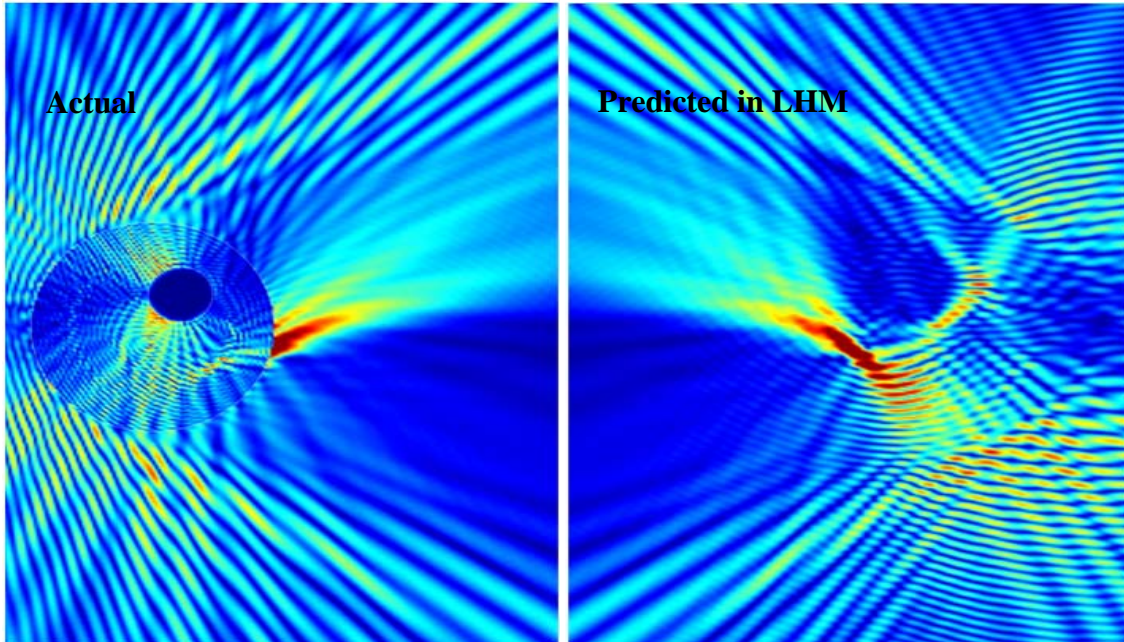


**Figure 4.11.** Magnetic field intensity ( $H_x$ ) distribution for two objects: actual (in free space, at left) and reconstructed (in a LHM with  $n = -1$ , at right).

electric field intensity (top row) and phase (bottom row) are depicted in Figure 4.8. The results clearly show that the proposed technique is capable of inferring the locations of multiple objects if the scatterers are separated by at least one wavelength. The analysis has been done in the wave regime while keeping in mind that it should eventually be reimplemented in the low-frequency EMI regime if it is to be applied to the UXO detection and discrimination problem. Next we study the EM scattering from an extended object, a cylinder. The results appear in Figure 4.9.

In our next example we reconstruct the EM field due to three objects separated by more than one wavelength and illuminated by a Gaussian beam. The results, given on Figure 4.10, depict the actual electric field intensity (left) and the reconstructed intensity in the virtual LHM (right). The LHM reconstruction algorithm is able to infer the targets' locations and predicts very accurately the EM field distribution between the free-space/LHM boundary and the objects. On the other hand, the reconstructed fields *behind the objects* diverge from the actual field; this is because the scattered field at the free-space/LHM interface does not contain information about the EM field due to the objects' invisible parts.

Finally, we apply the LHM reconstruction technique to a cylindrical object immersed in another cylinder. The targets are illuminated by a Gaussian beam source; the immersed object has a size equal to one wavelength. The scattered EM field from the targets is computed on the surface of the LHM half-space and then reconstructed inside the medium. The actual and reconstructed  $H_x$  and  $H_y$  magnetic fields are depicted on Figures 4.11 and 4.12 respectively. The results show that the algorithm is able to detect and correctly identify the scatterers' geometries and positions using different components of the scattered magnetic field.

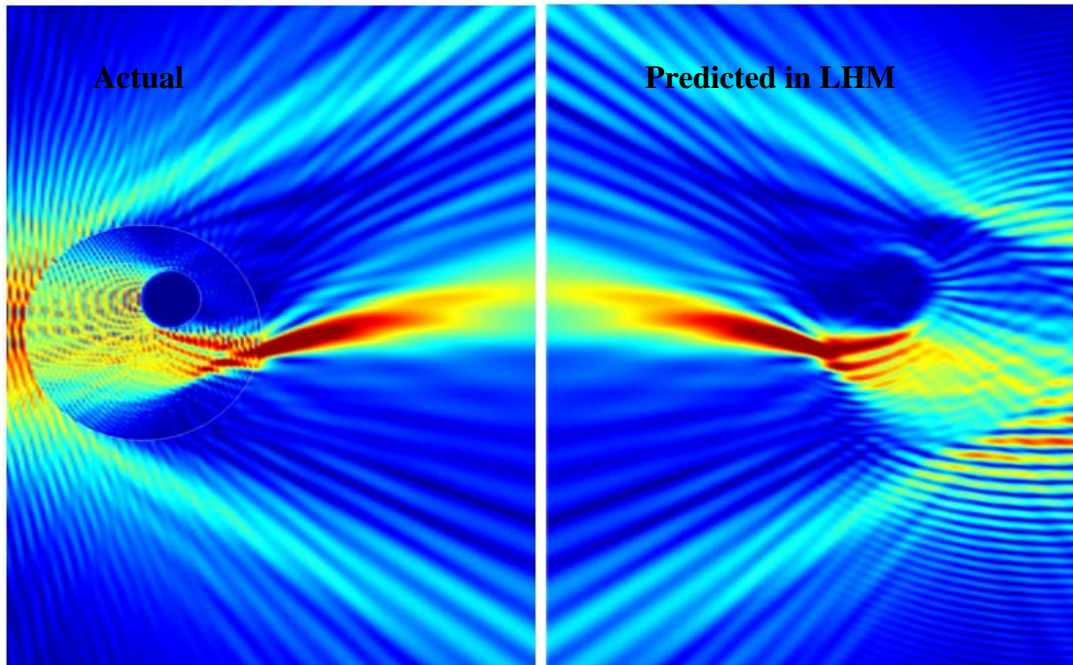


**Figure 4.12.** Magnetic field ( $H_y$ ) intensity distribution for two objects: actual (in free space, at left) and reconstructed (in a LHM with  $n = -1$ , at right).



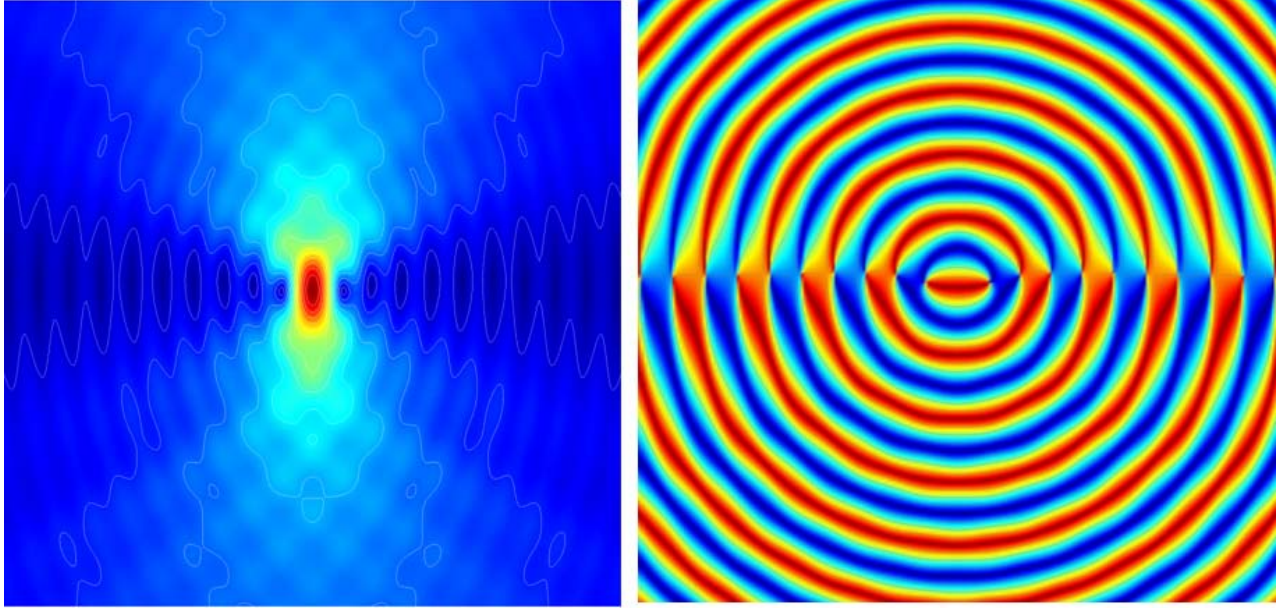


**Figure 4.13.** Reconstructed electric field-intensity (left) and phase (right) distributions for three point sources in a LHM with  $n = -1$  when the wavelength is 1000 times greater than the distances between the objects.

#### 4.6.3. An attempt to extend the LHM approach to the EMI regime

*In the EMI (low-frequency) regime the relevant wavelengths are much larger than the sizes of the scatterers, and as a consequence there are no waves, but rather diffusion and potential fields.* In order to illustrate the performance of the LHM approach in the low-frequency case we revisit the problem reported in Figure 4.8 but make the wavelength be 1000 times greater than the distance between the objects. The results appear in Figure 4.13. Now the three objects seem to behave as a single target, and it becomes very difficult to identify their locations correctly.

This suggests that we cannot directly apply LHM wave phenomena to the EMI case, as there is no field propagation *per se*. However, we thought that by using a spatial distribution of EMI measured data we could generate a synthetic/theoretical Gaussian beam. As is well documented in the optics literature, a Gaussian (paraxial) beam is a plane wave  $e^{-jkz}$  (with wave number  $k = 2\pi/\lambda$  and wavelength  $\lambda$ ) modulated by a complex envelope  $A(\mathbf{r})$  that is a slowly varying function of position. The complex amplitude is thus

$$U(\mathbf{r}) = A(\mathbf{r}) e^{-jkz}. \quad (10)$$

The envelope is assumed to be approximately constant within a neighborhood of size  $\lambda$ , so the beam behaves locally like a plane wave. The spatial distribution of the envelope  $A(\mathbf{r})$  determines the beam shape (Gaussian, rectangular, sine or cosine) and the factor  $e^{-jkz}$  describes wave propagation. In EMI we cannot incorporate this latter term, but we can still try to match the

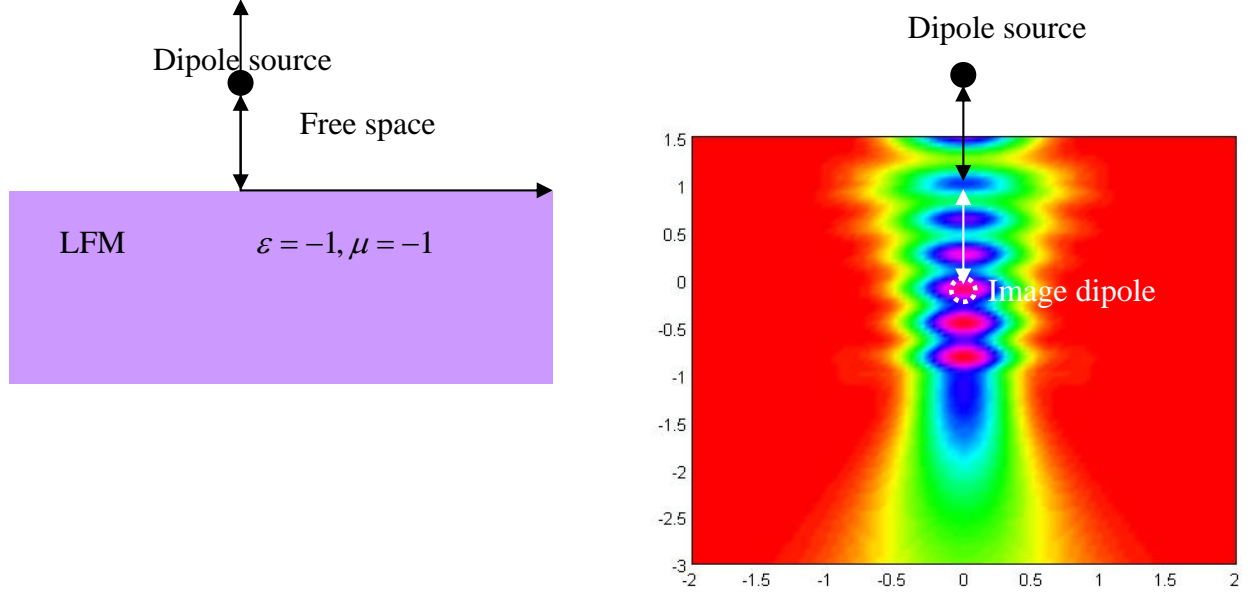


**Figure 4.14.** Problem geometry (left) and reconstructed magnetic-field intensity distribution (right) for a dipole.

spatial distribution of the envelope  $A(\mathbf{r})$  to monostatic or bistatic data  $D(\mathbf{r})$  measured on a set of grid points; this can be either (1) the magnetic field  $H_z$  measured by the GEM sensor, (2) the induced voltage in the EM-63 sensor, or (3) the amplitude of the total scattered magnetic field as measured by the new GEM-3D sensor.

To demonstrate the applicability of the proposed technique to the EMI problem we focus on a simple example. Above a LHM slab we place a static magnetic dipole oriented along the  $z$ -axis (see Figure 4.14). Using the Biot-Savart law we can compute the spatial distribution of the  $H_z(\mathbf{r})$  magnetic field on the top boundary of the LHM slab and take it to be the shape of the envelope:  $A(\mathbf{r}) = H_z(\mathbf{r})$ . We then solve the full EM scattering problem for normal incidence of the Gaussian beam on the slab. The reconstructed near-field distributions inside and outside the LHM are shown in Figure 4.14. It is worth noting that the distance from the top boundary of the LHM to the first focus (white arrow) equals the distance from the first focus to the dipole (black arrow). This illustrates that LHM techniques could potentially be used to locate buried objects. However, in this test we chose a “synthetic” wavelength  $\lambda$  comparable to the distance between the matching boundary and the dipole. Further studies demonstrated that the predicted dipole location depends on  $\lambda$ , and that in general the reconstructed locations for low-frequency cases are very sensitive to the actual locations and to the spatial range and density of the measured data. The least-squares problems (4.20) and (4.21) are also sensitive to the noise level. All of these facts make the LHM approach less attractive for UXO detection and discrimination.

## 4.7. Conclusion

In this chapter we investigated the LHM approach as a potential candidate for estimating the location of a buried object without having to solve a traditional ill-posed inverse scattering problem. We discussed in detail the theoretical basis and the numerical realization of the method in the high-frequency EM-wave regime and then used it to reconstruct the field and infer the location of a point source, a Gaussian beam, and different combinations of multiple objects. The results demonstrated the refocusing property of a planar LHM half-space (*i.e.*, the fact that it sends signals backward to the origin) and its ability to estimate the location and geometry of an object. These results suggest a number of interesting applications of the LHM approach. For example, it could be used as a new tool for solving inverse scattering problems in the microwave and optical frequency regimes. Another potential application could be image reconstruction with sub-wavelength resolution.

We then applied the proposed technique to low-frequency cases in order to assess its potential usefulness in the context of the UXO problem. Our studies show that in the low-frequency regime the LHM refocusing approach is impractical because the necessary wavelength is much larger than the size and depth of any potentially interesting target. We attempted to construct a Gaussian beam by combining a monostatic EMI spatial distribution with an empirically assigned wave-phase part. However, our studies reveal that the approach is very sensitive to the object's orientation and to the wave number. Thus the refocused EM fields have maxima whose locations depend quite strongly on the phase distribution on the boundary. In addition we found that the method is very sensitive to noise. The fact that real UXO detection and discrimination problems always involve very noisy data leads us to conclude that the LHM approach is more suitable for the EM wave regime than it could be for UXO discrimination.

# Chapter 5

## Discussion and Conclusions

### 5.1. Objectives

The objective of the proposed work was to develop new non-traditional physics-based inverse approaches that could let us determine the location and orientation of buried objects starting from actual EMI data but without solving an ill-posed inverse scattering problem. The specific technical objectives were the following:

1. Develop an approach combining NSMS and the physics-based pole distribution and prove that this combination can be used to determine the location and orientation of a buried object starting from measured spatially distributed EMI data without having to resort to the traditional inverse-scattering procedure.
2. Determine if the directional vectors corresponding to the energy gradient of the scattered magnetic field always cross at a single point, and whether or not this point is always inside the scatterer. Use NSMS to perform upward continuation on the measured data in a defined space, compute the magnetic field gradient at each point in the space, determine the gradient's directional vectors toward the ground, find the point where these vectors cross, and relate the crossing point to the buried object's location.
3. Determine the feasibility of exploiting the physical properties of new left-handed media (LHM), in particular the possibility of making perfect lenses out of them, to determine the location and orientation of an object. Construct a paraxial (Gaussian) beam with the spatial part of an actual set of EMI measurements, define a left-handed-medium slab, and refocus the beam inside the slab, thus determining the object's location.
4. Evaluate and document the robustness of the proposed approaches for most realistic scenarios, in which an object's response is contaminated by complex, heterogeneous noise associated with the positioning accuracy of the sensor, uncertainties in orientation, and the possibility of response from cluttered background involving two or more objects.

Under this project we developed three methods: (1) HAP, (2) Pole-series expansions and (3) LHM-based approaches. We assessed the ability of each technique to predict the location and orientation of a buried object by comparing inversion results to the ground truth. We found that all three techniques have the potential to estimate position and orientation at different frequencies. However, when objects' responses are contaminated with additive noise, the performance of the pole-series-expansion and LHM methods degrade significantly compared to that of the HAP technique. In addition, the computational time required by the PSE and LHM approaches and similar practical considerations prevented us from further testing and developing those two techniques, leaving the HAP as our weapon of choice for determining buried objects' locations and orientations.

## 5.2. HAP method

The HAP method is a new physics-based analytical/numerical technique that uses global quantities—the magnetic field  $\mathbf{H}$ , the vector potential  $\mathbf{A}$ , and the scalar potential  $\psi$ —to estimate the location, orientation, and magnetic polarizability of a buried object. The method should be valid for both land-based and underwater UXO surveys. To find  $\mathbf{A}$  and  $\psi$  from measured  $\mathbf{H}$  (in monostatic or multistatic cases) we developed a two-dimensional version of the normalized surface magnetic source (NSMS) model, in which fictitious sources are distributed on an auxiliary surface just below the measurement grid and their responding amplitudes are determined using a collocation algorithm. We tested the HAP technique in the time and frequency domains, using both synthetic and measured data, in noise-free and noisy environments, and with point dipoles, spheres, and actual UXO as scatterers.

We carried out blind-test analyses using real UXO interrogated by the MPV-TD and GEM-3D+ sensors. We first estimated the positions and orientations of the objects via HAP, and then to perform classification we used a three-dimensional NSMS method with dipole responding sources distributed on a spheroid surrounding the object: for each unknown target we determined the NSMS amplitudes, integrated those to find a total time/frequency-dependent NSMS curve, and used the curves as discriminators by comparing them to pre-computed samples belonging to a library of known UXO types. The method was able to identify with reasonable accuracy the positions and orientations of the targets and had 100% success classifying them into UXO and clutter and identifying the UXO type.

We also adapted the HAP method to the EM63 and NRL EMI array TD sensors. Our results, reported in Chapter 2, clearly demonstrate the superior performance (and the robustness with respect to sensor noise) of the HAP technique as a method for estimating the locations and orientations of single or aggregate buried targets.

## 5.3. Outlook

The work presented here has demonstrated that the HAP approach has the potential to make UXO discrimination more reliable and faster by providing a trustworthy means to determine location and orientation. However, a substantial research and development effort must be undertaken before the technique can be applied to real-world UXO problems. This effort should address, among others, the following issues:

- **Comparison to nonlinear inverse-scattering models:** Nonlinear inverse-scattering models are the most commonly used techniques for determining the position of a buried object. In this study, we did not investigate if the HAP approach represents a significant improvement over traditional nonlinear inverse-scattering methods. We have found HAP to be fast, accurate, and not plagued by local minima, which suggests that the technique can be used in combination with physically complete models—such as NSMS and GSEA—to perform UXO discrimination in real or near real time. We would expect that, once an object’s position and orientation are accurately known, a UXO discrimination approach based on physically complete forward models would be much faster and better than the traditional nonlinear inverse models because the target’s intrinsic parameters could be determined much more exactly. Our studies show that the HAP model is robust with respect to noise. Now that we have established a method for recovering an object’s

location and orientation, we should be in a position to compare our algorithm to more traditional approaches with regard to stability and generality.

- **EMI data density and sensitivity analysis:** For application to practical UXO discrimination problems, it is critical to determine the data fidelity required for HAP techniques. In order to estimate the 2D NSMS responding amplitudes and the polarizability tensor of the induced magnetic dipole we need to determine a minimum number of data points (or a minimum data density) as a function of signal-to-noise ratio, spatial data coverage, positional error, and other survey/instrument characteristics.
- **Multiple Targets:** The data considered in this study were from single, isolated targets. However, separating and performing discrimination on overlapping signals from multiple objects using the HAP or any other existing technique is still an open question. To extend HAP into an  $N$ -target locator technique, one that will reliably say how many targets are present in the sensor's field of view, where they are, and what tilt they have, all of this without resorting to computationally taxing optimizations, is a highly desirable and important step that the UXO community must take.
- **Geologic background:** Signals coming from background geology always pose additional problems during UXO discrimination. We need to investigate how the presence of magnetically susceptible soil affects the performance of HAP; *i.e.*, we need to incorporate the soil's response into the HAP model.
- **Underwater UXO discrimination:** We have demonstrated mathematically that the HAP approach can in principle make valid predictions if the target is in an underwater environment. At this point, however, we have not investigated if this is true when actual EMI data are considered. Our success with land-based predictions is a good first step in that direction.



## References

### Technical publications produced under this project:

- F. Shubitidze, D. Karkashadze, B. E. Barrowes, I. Shamatava, and K. O'Neill (2007), "A new physics based approach for estimating a buried object's location orientation and magnetic polarization from EMI data wide-band electromagnetic induction problem." J. Environ. Eng. Geophys., **In-press**.
- F. Shubitidze, D. Karkashadze, B. Barrowes, K. O'Neill. "An analytical expression for estimating a buried object's location, orientation and magnetic polarization to support UXO discrimination". Proceedings of XIIth International Seminar/Workshop on Direct and Inverse Problems of Electromagnetic and Acoustic Wave Theory (DIPED-2007), September 17-20, 2007, L'viv Ukraine, Georgia. pp. 126-129.
- F. Shubitidze, B. E. Barrowes, K. O'Neill, I. Shamatava, and J. P. Fernández (2007), "A combined NSMC and pole series expansion approach for UXO discrimination." Proc. SPIE **6553**, 65530E.
- F. Shubitidze, B. E. Barrowes, I. Shamatava, J. P. Fernández, and K. O'Neill (2008), "Application of the NSMS model to multi-axis time domain EMI data." Proc. SPIE **6953**, 695303-1-11.
- F. Shubitidze, E. Demidenko, B. E. Barrowes, I. Shamatava, J. P. Fernández, and K. O'Neill (2008), "Combining dipole and mixed model approaches for UXO discrimination." Proc. SPIE **6953**, 695305-1-12.
- F. Shubitidze, J. P. Fernández, B. E. Barrowes, I. Shamatava, and K. O'Neill (2008), "Combining NSMS and high-quality MPV-TD data for UXO discrimination." International Geophysics and Remote Sensing Symposium, Boston, MA.
- F. Shubitidze, B. Barrowes, K. O'Neill, I. Shamatava, J. P. Fernández, "NSMC for UXO discrimination in cases with overlapping signatures", UXO/Counter-Mine forum Orlando Florida, August 27-30, 2007.
- F. Shubitidze, B. Barrowes; D. Karkashadze; I. Shamatava; K. O'Neill , "A non-traditional inverse-scattering approach for estimating a buried object's location, orientation and magnetic polarizability tensor", Partners in Environmental Technology Technical Symposium and Workshop, Washington DC, December 4-6, 2007.
- F. Shubitidze, Benjamin Barrowes, Kevin O'Neill, Irma Shamatava, Juano Fernández, "Combined NSMC and Pseudo-Spectral Finite-Difference Method for Inverting a Buried Object Location", 20-th Anniversary Symposium on the Application of Geophysics to Engineering and Environmental problems, SAGEEP-2007, pp-1475-1484.

### Other references:

- H. T. Anastassiou, D. I. Kaklamani, D. P. Economou, and O. Breinbjerg (2002), "Electromagnetic scattering analysis of coated conductors with edges using the method of auxiliary sources (MAS) in conjunction with the standard impedance boundary condition (SIBC)." IEEE Trans. Antennas Propagat. **50**(1), 59-66.
- V. I. Arnold (1986), *Catastrophe Theory*, second edition. Berlin, Springer.

- B. E. Barrowes, K. O'Neill, D. D. Snyder, D. C. George, and F. Shubitidze (2006), "New man-portable vector time-domain EMI sensor and discrimination processing." UXO/Countermining Forum, Las Vegas, NV.
- N. Bliznyuk, R. J. Pogorzelski, and V. P. Cable (2005), "Localization of scattered field singularities in the Method of Auxiliary Sources." Proceedings of the 2005 IEEE AP-S/URSI Symposium.
- C. N. G. Dampney (1969), "The equivalent source technique." *Geophysics* **34**, 39–53.
- E. Gasperikova (2006), "Berkeley UXO Discriminator (BUD) for UXO detection and discrimination." SERDP and ESCTP's Partners in Environmental Technology Technical Symposium & Workshop, Washington, DC.
- A. G. Kyurhkan, B. Y. Sternin, and V. E. Shatalov (1996), "Singularities of continuation of wave fields." *Sov. Phys. Usp.* **39**(12), 1221–1242.
- J. D. McNeill and M. Bosnar (1996), "Application of time-domain electromagnetic techniques to UXO detection." Proceedings of UXO Forum.
- H. H. Nelson and J. R. McDonald (2001), "Multi-sensor towed array detection system for UXO detection." *IEEE Trans. Geosci. Remote Sensing* **39**(6), 1139–1145.
- K. O'Neill, I. J. Won, A. Oren, F. Shubitidze, K. Sun, and I. Shamatava (2004), "A new handheld vector EMI sensor with precise 3D positioning." UXO/Countermining Forum, St. Louis, MO.
- L. R. Pasion and D. W. Oldenburg (2001), "A discrimination algorithm for UXO using time domain electromagnetics." *J. Environ. Eng. Geophys.* **6**, 91–102.
- J. B. Pendry, A. J. Holden, W. J. Stewart, and I. Youngs (1996), "Extremely low frequency plasmons in metallic meso structures." *Phys. Rev. Lett.* **76**, 4773–4776.
- J. B. Pendry, A. J. Holden, D. J. Robbins, and W. J. Stewart (1999), "Magnetism from conductors and enhanced nonlinear phenomena." *IEEE Trans. Microwave Theory Tech.* **47**(11), 2075–2084.
- F. Shubitidze, K. O'Neill, S. A. Haider, K. Sun, and K. D. Paulsen (2002), "Application of the method of auxiliary sources to the wide-band electromagnetic induction problem." *IEEE Trans. Geosci. Remote Sensing* **40**(4), 928–942.
- F. Shubitidze, H. T. Anastassiou, and D. I. Kaklamani (2004), "An improved accuracy version of the method of auxiliary sources for computational electromagnetics." *IEEE Trans. Antennas Propagat.* **52**(1), 302–309.
- F. Shubitidze, K. O'Neill, I. Shamatava, K. Sun, and K. D. Paulsen (2005), "Fast and accurate calculation of physically complete EMI response by a heterogeneous metallic object." *IEEE Trans. Geosci. Remote Sensing* **43**(8), 1736–1750.
- F. Shubitidze, K. O'Neill, B. E. Barrowes, I. Shamatava, J. P. Fernández, K. Sun, and K. D. Paulsen (2007), "Application of the normalized surface magnetic charge model to UXO discrimination with overlapping signals." *J. Appl. Geophys.* **61**, 292–303.
- F. Shubitidze, E. Demidenko, B. E. Barrowes, I. Shamatava, J. P. Fernández, and K. O'Neill (2008), "Combining dipole and mixed model approaches for UXO discrimination." *Proc. SPIE* **6953**, 695305-1–12.
- J. A. Stratton (1941), *Electromagnetic Theory*. New York, McGraw-Hill.
- K. Sun, K. O'Neill, F. Shubitidze, I. Shamatava, and K. D. Paulsen (2005), "Fast data-derived fundamental spheroidal excitation models with application to UXO discrimination." *IEEE Trans. Geosci. Remote Sensing* **43**(11), 2573–2583.
- V. G. Veselago (1968), "Electrodynamics of substances with simultaneously negative electrical and magnetic permeabilities." *Sov. Phys. Usp.* **10**, 509.
- I. J. Won, D. A. Keiswetter, D. R. Hanson, E. Novikova, and T. M. Hall (1997), "GEM-3: a monostatic broadband electromagnetic induction sensor." *J. Environ. Eng. Geophys.* **2**, 53–64.
- R. Zaridze, G. Bit-Babik, K. Tavzarashvili, D.P. Economou, and N.K. Uzunoglu (2002), "Wave field singularity aspects in large-size scatterers and inverse problems." *IEEE Trans. Antennas Propagat.* **50**(1), 50–58.

- R. W. Ziolkowski (2003), “Pulsed and CW Gaussian beam interactions with double negative metamaterial slabs.” Opt. Express **11**(7), 662–681.